

IntechOpen

Direct Torque Control Strategies of Electrical Machines

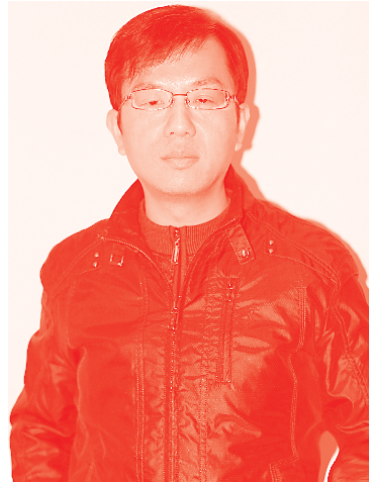
Edited by Fatma Ben Salem



Direct Torque Control Strategies of Electrical Machines

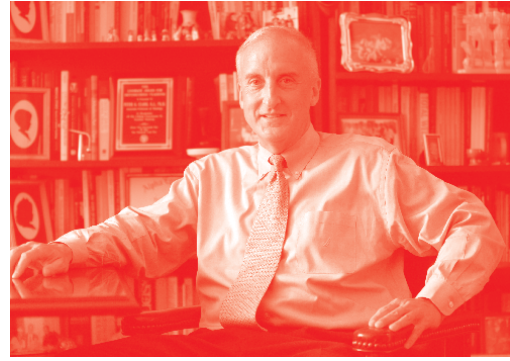
Edited by Fatma Ben Salem

Published in London, United Kingdom



IntechOpen





Supporting open minds since 2005



Direct Torque Control Strategies of Electrical Machines

<http://dx.doi.org/10.5772/intechopen.80103>

Edited by Fatma Ben Salem

Contributors

Mohamed Haithem Lazreg, Abderrahim Bentaallah, Fatma Ben Salem, Yuting Gao, Yang Liu, Cherifi Djamilia, Miloud Yahia, Dr. Venu Madhav Gopala, Obulesu Y. P., Adhavan Balashanmugham, Maheswaran Mockaisam, Sathiyathan Murugesan, Tojiddin Khayrullaevich Juraev, Sobir Norov, Musulmanov Furqat Shodiyevich

© The Editor(s) and the Author(s) 2021

The rights of the editor(s) and the author(s) have been asserted in accordance with the Copyright, Designs and Patents Act 1988. All rights to the book as a whole are reserved by INTECHOPEN LIMITED. The book as a whole (compilation) cannot be reproduced, distributed or used for commercial or non-commercial purposes without INTECHOPEN LIMITED's written permission. Enquiries concerning the use of the book should be directed to INTECHOPEN LIMITED rights and permissions department (permissions@intechopen.com).

Violations are liable to prosecution under the governing Copyright Law.



Individual chapters of this publication are distributed under the terms of the Creative Commons Attribution 3.0 Unported License which permits commercial use, distribution and reproduction of the individual chapters, provided the original author(s) and source publication are appropriately acknowledged. If so indicated, certain images may not be included under the Creative Commons license. In such cases users will need to obtain permission from the license holder to reproduce the material. More details and guidelines concerning content reuse and adaptation can be found at <http://www.intechopen.com/copyright-policy.html>.

Notice

Statements and opinions expressed in the chapters are these of the individual contributors and not necessarily those of the editors or publisher. No responsibility is accepted for the accuracy of information contained in the published chapters. The publisher assumes no responsibility for any damage or injury to persons or property arising out of the use of any materials, instructions, methods or ideas contained in the book.

First published in London, United Kingdom, 2021 by IntechOpen

IntechOpen is the global imprint of INTECHOPEN LIMITED, registered in England and Wales, registration number: 11086078, 5 Princes Gate Court, London, SW7 2QJ, United Kingdom

Printed in Croatia

British Library Cataloguing-in-Publication Data

A catalogue record for this book is available from the British Library

Additional hard and PDF copies can be obtained from orders@intechopen.com

Direct Torque Control Strategies of Electrical Machines

Edited by Fatma Ben Salem

p. cm.

Print ISBN 978-1-83880-295-0

Online ISBN 978-1-83880-296-7

eBook (PDF) ISBN 978-1-83880-359-9

We are IntechOpen, the world's leading publisher of Open Access books Built by scientists, for scientists

5,100+

Open access books available

127,000+

International authors and editors

145M+

Downloads

156

Countries delivered to

Our authors are among the
Top 1%

most cited scientists

12.2%

Contributors from top 500 universities



WEB OF SCIENCE™

Selection of our books indexed in the Book Citation Index
in Web of Science™ Core Collection (BKCI)

Interested in publishing with us?
Contact book.department@intechopen.com

Numbers displayed above are based on latest data collected.
For more information visit www.intechopen.com



Meet the editor



Fatma Ben Salem was born in Sfax, Tunisia, in 1978. She received her BS, MSc, Ph.D., and HCR degrees in 2002, 2003, 2010, and 2015, respectively, all in electrical engineering from the National Engineering School of Sfax, University of Sfax, Tunisia. She is an associate professor of electrical engineering at the High Institute of Industrial Management of Sfax, Tunisia. She is a member of the Control Energy Management Laboratory (CEMLab) of the University of Sfax. She is the author of several journals and international conference papers. She has participated in writing book chapters and in the organization of international conferences and workshops. She is an IEEE member. Her main research interests cover several aspects related to the control and the diagnostics of electrical machine drives and generators involved in automotive as well as in renewable energy systems.

Contents

Preface	III
Section 1	
Direct Torque Control of Induction Motors	1
Chapter 1	3
Improved Direct Torque Control Based on Neural Network of the Double-Star Induction Machine Using Deferent Multilevel Inverter <i>by Mohamed Haithem Lazreg and Abderrahim Bentaallah</i>	
Chapter 2	17
Direct Torque Control Strategies of Induction Machine: Comparative Studies <i>by Cherifi Djamila and Miloud Yahia</i>	
Chapter 3	39
DTC-SVM Approaches of an Induction Motor Dedicated to Position Control Applications <i>by Fatma Ben Salem</i>	
Section 2	
Direct Torque Control Improvements	65
Chapter 4	67
Flux Reversal Machine Design <i>by Yuting Gao and Yang Liu</i>	
Chapter 5	101
Predictive Direct Torque Control Strategy for Doubly Fed Induction Machine for Torque and Flux Ripple Minimization <i>by Gopala Venu Madhav and Y.P. Obulesu</i>	
Chapter 6	123
Study of the Parameters of the Planner with a Screw Working Body <i>by Juraev Tojiddin Khayrullaevich, Norov Sobirjon Negmurodovich and Musulmanov Furqat Shodiyevich</i>	

Torque Ripple Reduction in DTC Induction Motor Drive
*by Adhavan Balashanmugham, Maheswaran Mockaisamy
and Sathiyathan Murugesan*

Preface

Electrical machines are being widely used today in traction systems, robotics, and other position control systems. The modern applications demand advanced control techniques with high precision. The Direct Torque Control (DTC) method is one of the highest performance control strategies for AC machines to provide rapid torque and flux control. It is widely known to produce a quick and fast response in AC drives by selecting the proper voltage space vector according to the switching status of the inverter. The main advantage of DTC is its simple structure. Within this framework, this book entitled Direct Torque Control Strategies of Electrical Machines consists of a representation of theoretical results related to design and advanced control of AC machines and the diagnostics of electrical machine drives and generators involved in automotive systems. The priority has been focused on the DTC approach applications with and without commutation frequency control. It also covers DTC applications using artificial intelligence.

This book consists of seven chapters that have been written by leading researchers covering recent theoretical developments and applications of DTC strategies. It combines theoretical analysis, simulation, and experimental concepts. It is expected that readers require background knowledge to understand various concepts and results presented in this book.

Finally, the editor would like to express their sincere gratitude to authors from all over the world for submitting their high-quality work in a timely manner and revising it appropriately at short notice. A particular thanks and my deepest gratitude to the IntechOpen editorial staff for their continuous support, assistance, and significant improvement in the manuscript. Without their help, the book would not be published as scheduled.

Fatma Ben Salem
Associate Professor (ISGIS),
Sfax University, Tunisia

Section 1

Direct Torque Control of Induction Motors

Improved Direct Torque Control Based on Neural Network of the Double-Star Induction Machine Using Deferent Multilevel Inverter

Mohamed Haithem Lazreg and Abderrahim Bentaallah

Abstract

In this chapter, we will compare the performance of a multilevel direct torque control (DTC) control for the double-star induction machine (DSIM) based on artificial neural network (ANN). The application of DTC control brings a very interesting solution to the problems of robustness and dynamics. However, this control has some disadvantages such as variable switching frequency, size, and complexity of the switching tables and the strong ripple torque. A solution to this problem is to increase the output voltage level of the inverter and associate the DTC control with modern control techniques such as artificial neural networks. Theoretical elements and simulation results are presented and discussed. As results, the flux and torque ripple of the five-level DTC-ANN control significantly reduces compared to the flux and torque ripple of the three-level DTC-ANN control. By viewing the simulation results using MATLAB/Simulink for both controls, the results obtained showed a very satisfactory behavior of this machine.

Keywords: double-star induction machine (DSIM), direct torque control (DTC), three-level inverter, five-level inverter, artificial neural network (ANN)

1. Introduction

The use of a conventional two-level inverter in the field of high power applications is not appropriate because it requires electronic components capable of withstanding high reverse voltage and high current. Another disadvantage of this inverter is the problem of magnetic interference caused by the abrupt change of the output voltage of the inverter from zero to high value [1].

With the appearance of the structures of the multilevel inverters proposed for the first time by [2], the research was able to face the handicaps presented by the classical structure. The goal of this research focus is to improve the quality of the output voltage, as well as to overcome the problems associated with two-level inverters. There are several topologies of multilevel inverters such as floating-diode, floating-capacitor, and cascaded inverters [3]. These structures make it possible to generate an output voltage of several levels.

Diode-clamped inverter (DCI) is the one that attracts the most attention because of the simplicity of its structure compared to the floating capacity inverter; in fact

we do not need to use capacitors for each phase, which eliminates the risks of parasitic resonances [4]. In this structure, diodes called floating diodes are associated with each phase, which serves to apply the different voltage levels of the DC source.

In high power, AC machines powered by static inverters find more and more applications. But the constraints on the power components limit the switching frequency and therefore the performance. To enable the use of higher switching frequency components, the power must be divided. To do this, one of the solutions is to use multiphase machines thanks to their advantages, such as the power segmentation and the minimization of the ripples of the torque (elimination of the harmonic torque of rank six). One of the most common examples of multiphase machines is the double-star induction machine (DSIM) [5].

To improve the decoupling between the flux and the torque, a so-called direct torque control (DTC) control technique has been applied.

The conventional direct torque control (DTCc) is proposed by Takahashi and Depenbrock in 1985 [2], and several studies allowed to apply this control technique on multiphase machines. As for each control, the DTC has advantages and disadvantages, and among these advantages, the stator resistance is theoretically the only parameter of the machine that intervenes in the control. This is essential for estimating the stator flux vector [6]. From this purely theoretical point of view, one can thus consider a great robustness compared to the other parameters of the machine; the block PWM is usually deleted [7].

Despite these advantages, this control also has significant disadvantages, the problem of instability such as the lack of control of the generator of acoustic noise at the machine. In addition, the use of hysteresis tapes is the cause of electromagnetic torque ripples and noise in the machine. To solve these drawbacks, in the framework of this work, we try to apply the multilevel direct torque control for DSIM and to develop a new control method such as artificial neural networks that replaces the switching tables [8].

This chapter is organized as follows: the DSIM model will be presented in the next section. The three-level and the five-level inverter modeling is described in the third and fourth section. The control method by DTC based on artificial neural networks (DTC-ANN) will be discussed in the fifth section. Moreover, in the sixth section, the simulation results are presented. Finally, a general conclusion summarizes this work.

2. DSIM model

In the conventional configuration, two identical three-phase windings share the same stator and are shifted by an electric angle of 30° . The rotor structure remains identical to that of a three-phase machine [9].

The model of machine DSIM is nonlinear. The DSIM model fed by voltage inverter is given by the following equations [10]:

$$\frac{dX}{dt} = AX + BU \quad (1)$$

$$T_{em} = p \frac{L_m}{L_r + L_m} \left[\varphi_{dr}(i_{qs1} + i_{qs2}) - \varphi_{qr}(i_{ds1} + i_{ds2}) \right] \quad (2)$$

$$J \frac{d\Omega}{dt} = T_{em} - T_L - k_f \Omega \quad (3)$$

where:

$$X = [x_1, x_2, x_3, x_4, x_5, x_6]^T = [i_{ds1}, i_{ds2}, i_{qs1}, i_{qs2}, \phi_{dr}, \phi_{qr}]^T$$

$$U = [v_{ds1}, v_{ds2}, v_{qs1}, v_{qs2}]$$

Matrixes A and B are given by

$$A = \begin{bmatrix} a_1 & a_2 & a_3 & a_4 & a_5 & a_6 \\ -a_2 & a_1 & -a_4 & a_3 & -a_6 & a_5 \\ a_3 & a_4 & a_1 & a_2 & a_5 & a_6 \\ -a_4 & a_3 & -a_2 & a_1 & -a_6 & a_5 \\ a_9 & a_8 & a_7 & 0 & a_7 & 0 \\ -a_8 & a_9 & 0 & a_7 & 0 & a_7 \end{bmatrix} \quad B = \begin{bmatrix} b_1 & 0 & b_2 & 0 \\ 0 & b_1 & 0 & b_2 \\ b_2 & 0 & b_1 & 0 \\ 0 & b_2 & 0 & b_1 \end{bmatrix}$$

where

$$a_1 = b_0 \frac{L_m}{T_r} - b_1 R_s, \quad a_2 = \omega_s (b_1 L_1 + b_2 L_2), \quad a_3 = b_0 \frac{L_m}{T_r} - b_2 R_s, \quad a_4 = \omega_s (b_1 L_2 + b_2 L_1),$$

$$a_5 = \frac{-b_0}{T_r}, \quad a_6 = a_0 b_3 + \omega_g b_0, \quad a_7 = \frac{L_m}{T_r}, \quad a_8 = \omega_g, \quad a_9 = -\frac{1}{T_r}, \quad a_{10} = \frac{3}{2} p \frac{L_m}{L_r},$$

$$\sigma = 1 - \frac{L_m^2}{L_s L_r}, \quad L_1 = \sigma L_s, \quad L_2 = \sigma L_s - l_s, \quad L_3 = L_s (1 - \sigma), \quad a_0 = \frac{L_m}{L_r}, \quad b_0 = \frac{L_m}{L_r (L_1 + L_2)},$$

$$b_1 = \frac{L_1}{L_1^2 - L_2^2}, \quad b_2 = \frac{L_2}{L_1^2 - L_2^2}, \quad b_3 = \omega_s (b_1 + b_2)$$

3. Modeling of three-level inverter

Figure 1 shows the structure of the three-level floating-diode inverter introduced by A. Nabae and H. Akagi in 1981 [11] (**Table 1**).

The three symmetrical arms consist of four fully controllable switches. These switches must not be opened or closed simultaneously, in order to avoid short circuiting of the DC source at the input of the inverter. Each switch is composed of an antiparallel transistor with a diode. The floating diodes ensure the application of the different voltage levels at the output of each arm. The DC input voltage is divided into two equal parts by using two capacitors. Each capacitor must be sized for a voltage equal to $v_{dc}/2$ [12].

The switching function of each switch T_{xki} ($k = 1, 2, i = 1 \dots 4, x = a, b, \text{ and } c$) is defined as follows:

$$F_{xki} = \begin{cases} 1 & \text{if } T_{xki} \text{ is ON} \\ 0 & \text{if } T_{xki} \text{ is OFF} \end{cases} \quad (4)$$

The controls of the switches of the lower half-arms are complementary to those of the upper half-arms:

$$F_{xki} = 1 - F_{xk(i-2)} \quad (5)$$

For each arm, we define three connection functions:

$$\begin{cases} F_{c1xk} = F_{c1xk}F_{c2xk} \\ F_{c2xk} = F_{c2xk}F_{c3xk} \\ F_{c3xk} = F_{c3xk}F_{c4xk} \end{cases} \quad (6)$$

The output voltages with respect to the neutral point of the DC source are expressed by

$$\begin{pmatrix} v_{a0k} \\ v_{b0k} \\ v_{c0k} \end{pmatrix} = \begin{pmatrix} F_{c1ak} & F_{c2ak} & F_{c3ak} \\ F_{c1bk} & F_{c2bk} & F_{c3bk} \\ F_{c1ck} & F_{c2ck} & F_{c3ck} \end{pmatrix} \begin{pmatrix} v_{c2} \\ 0 \\ -v_{c1} \end{pmatrix} \quad (7)$$

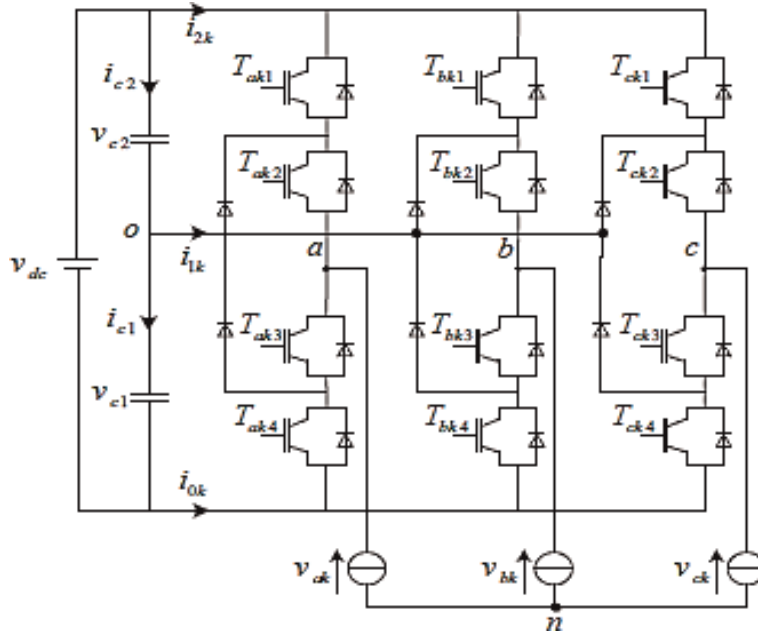


Figure 1. Three-phase inverter with floating diodes ($k = 1$ is the first inverter, and $k = 2$ is the second inverter).

Switching states	State of the switches of an arm				Output voltage
	T_{xk1}	T_{xk2}	T_{xk3}	T_{xk4}	
2	1	1	0	0	v_{c2}
1	0	1	1	0	0
0	0	0	1	1	$-v_{c1}$

Table 1. States of an arm of the inverter with three levels.

4. Modeling of five-level inverter

Currently the diode-clamped inverter is the one that attracts the most attention, given the simplicity of its structure compared to floating capacity inverters and cascading. In fact, compared to the inverter with floating capacities, it is not necessary to use capacities for each phase, which eliminates the risks of parasitic resonances.

The main advantage lies in a considerable reduction in switching losses and its ability to control harmonic content [13].

Figure 2 shows the structure of the inverter with five levels, each of the three arms of the inverter consists of eight controlled switches and six floating diodes. The controlled switches are unidirectional in voltage and bidirectional current; it is conventional associations of a transistor and an antiparallel diode.

These switches must not be opened or closed simultaneously, in order to avoid a short circuit of the DC source in the input. The floating diodes (six per arm) ensure the application of the different voltage levels at the output of each arm. The DC input voltage is divided into four equal parts using four capacitors [14].

The DC input bus is composed of four capacitors (C1, C2, C3, and C4), making it possible to create a set of three capacitive middle points. The total voltage of the DC bus is v_{dc} ; under normal operating conditions, this is uniformly distributed over the four capacitors, which then have a voltage $v_{dc}/4$ at their terminals [15] (**Table 2**).

For each switch T_{xki} ($k = 1, 2, i = 1 \dots 8, x = a, b, \text{ and } c$), a switching function is defined as follows:

$$F_{xki} = \begin{cases} 1 & \text{if } T_{xki} \text{ is ON} \\ 0 & \text{if } T_{xki} \text{ is OFF} \end{cases} \quad (8)$$

The switch control of the lower half-arms is complementary to those of the upper half-arms:

$$F_{xki} = 1 - F_{xk(i-4)} \quad (9)$$

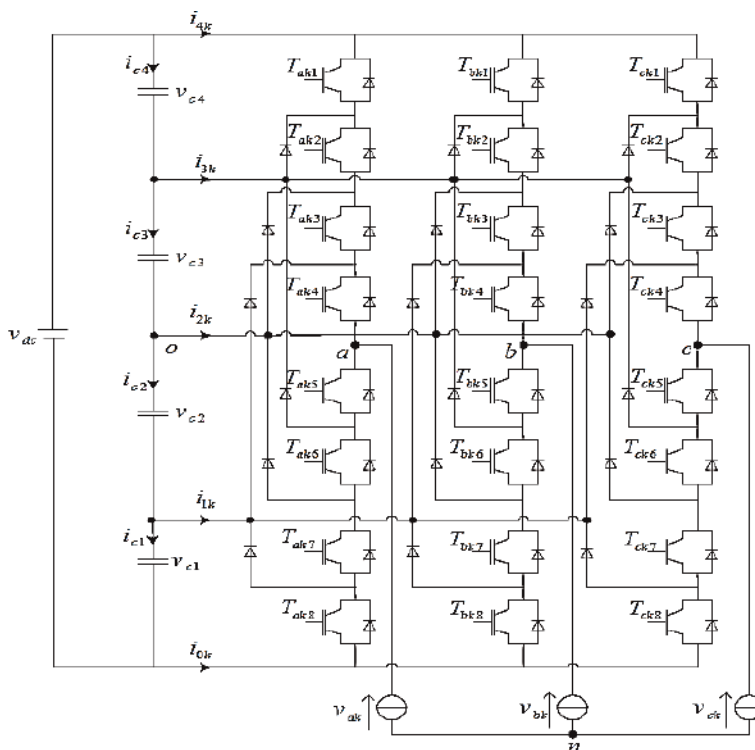


Figure 2.
 Diagram of the five-level inverter with NPC structure.

Switching states	State of the switches of an arm								Output voltage
	T _{xk1}	T _{xk2}	T _{xk3}	T _{xk4}	T _{xk5}	T _{xk6}	T _{xk7}	T _{xk8}	
4	1	1	1	1	0	0	0	0	v _{c3} + v _{c4}
3	0	1	1	1	1	0	0	0	v _{c3}
2	0	0	1	1	1	1	0	0	0
1	0	0	0	1	1	1	1	0	-v _{c2}
0	0	0	0	0	1	1	1	1	-(v _{c1} + v _{c2})

Table 2.
States of an arm of the inverter with five levels.

We define five connection functions, each associated with one of the five states of the arm:

$$\begin{cases} F_{c1xk} = F_{c1xk}F_{c2xk}F_{c3xk}F_{c4xk} \\ F_{c2xk} = F_{c2xk}F_{c3xk}F_{c4xk}F_{c5xk} \\ F_{c3xk} = F_{c3xk}F_{c4xk}F_{c5xk}F_{c6xk} \\ F_{c4xk} = F_{c4xk}F_{c5xk}F_{c6xk}F_{c7xk} \\ F_{c5xk} = F_{c5xk}F_{c6xk}F_{c7xk}F_{c8xk} \end{cases} \quad (10)$$

The potentials of nodes a, b, and c of the three-phase inverter at five levels with respect to the point o are given by the following system:

$$\begin{pmatrix} v_{a0k} \\ v_{b0k} \\ v_{c0k} \end{pmatrix} = \begin{pmatrix} F_{c1ak} & F_{c2ak} & F_{c3ak} & F_{c4ak} & F_{c5ak} \\ F_{c1bk} & F_{c2bk} & F_{c3bk} & F_{c4bk} & F_{c5bk} \\ F_{c1ck} & F_{c2ck} & F_{c3ck} & F_{c4ck} & F_{c5ck} \end{pmatrix} \begin{pmatrix} v_{c3} + v_{c4} \\ v_{c3} \\ 0 \\ -v_{c2} \\ -(v_{c1} + v_{c2}) \end{pmatrix} \quad (11)$$

5. Direct torque control based on neural networks

The direct torque control of a DSIM is based on the direct determination of the control sequence applied to the switches of a voltage inverter. This choice is based generally on the use of hysteresis comparators whose function is to control the state of the system, namely, the amplitude of the stator flux and the electromagnetic torque [16].

In the structure of the DTC, the voltage model is commonly used. Thus, the amplitude of the stator flux is estimated from its components following the axes (α , β):

$$\begin{cases} \hat{\phi}_{\alpha s} = \int_0^t (V_{\alpha s} - R_s I_{\alpha s}) dt \\ \hat{\phi}_{\beta s} = \int_0^t (V_{\beta s} - R_s I_{\beta s}) dt \end{cases} \quad (12)$$

The stator flux module is given by

$$\hat{\phi}_s = \sqrt{\hat{\phi}_\alpha^2 + \hat{\phi}_\beta^2} \quad (13)$$

The angle θ_s is given by

$$\hat{\theta}_s = \tan^{-1} \left(\frac{\hat{\phi}_\beta(t)}{\hat{\phi}_\alpha(t)} \right) \quad (14)$$

This method of estimating the stator flux has the advantage of simplicity and accuracy, particularly at medium and high speeds where the ohmic voltage drop becomes negligible [17].

The electromagnetic torque can be estimated from the estimated magnitudes of the stator flux and the measured magnitudes of the line currents, by the following equation:

$$\hat{T}_{em} = \frac{3}{2} p \cdot (\hat{\phi}_{\alpha s} i_{\beta s} - \hat{\phi}_{\beta s} i_{\alpha s}) \quad (15)$$

5.1 Neural network strategy

The human brain is able to adapt, learn, and decide, and it is on this fact that researchers have been interested in understanding its operating principle and being able to apply it to the field of computer science.

Among the disadvantages of DTC control, a slow response for small changes in stator flux and electromagnetic torque, size, and complexity of switching tables when the number of levels of inverters is high. In order to improve the performance of the DTC control, many contributions have been made in the DTC control based on artificial neural networks [18].

In this application, our goal is to replace switching tables with artificial neural networks.

The multilayer architecture was chosen to be applied to multilevel DTC control. This network, which can be multiplexed for each controller output, has acceptable performance in many industrial applications [19]. The neural network contains three layers: input layer, hidden layers, and output layer. Each layer consists of several neurons. The number of neurons in the output and the layers depends on the number of input and output variables chosen. The number of hidden layers and the number of neurons in each one depend on the dynamics of the system and the desired degree of accuracy.

Figure 3 shows the structure of the neural network applied to the multilevel DTC control of the DSIM. It is a network with three neurons in the input layer, whose inputs are flow error (Ef), torque error (Ec), and flow position angle (Z) [20]. For the three-level inverter, there are 12 neurons in the hidden layer and 06 neurons in the output, and for the five-level inverter, there are 24 neurons in the hidden layer and 12 neurons in the output. **Figure 4** shows the chosen architecture.

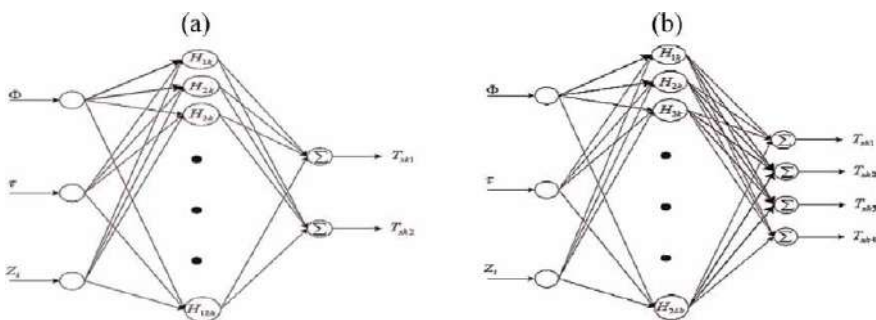


Figure 3. Neural network structure applied to the multilevel DTC control. (a) for three-level DTC, (b) for five-level DTC.

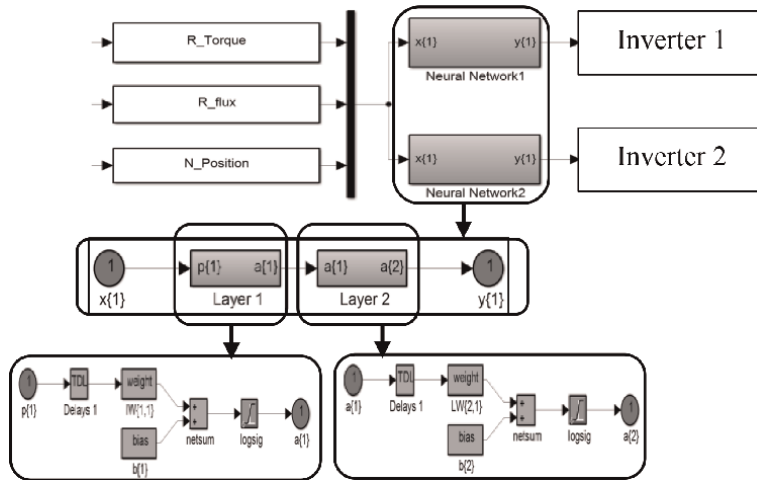


Figure 4. Selection table based on neuron network.

6. Simulation results

In order to test the static and dynamic performance of the control, the DSIM is accelerated from standstill to reference speed 100 rad/s. The machine is applied

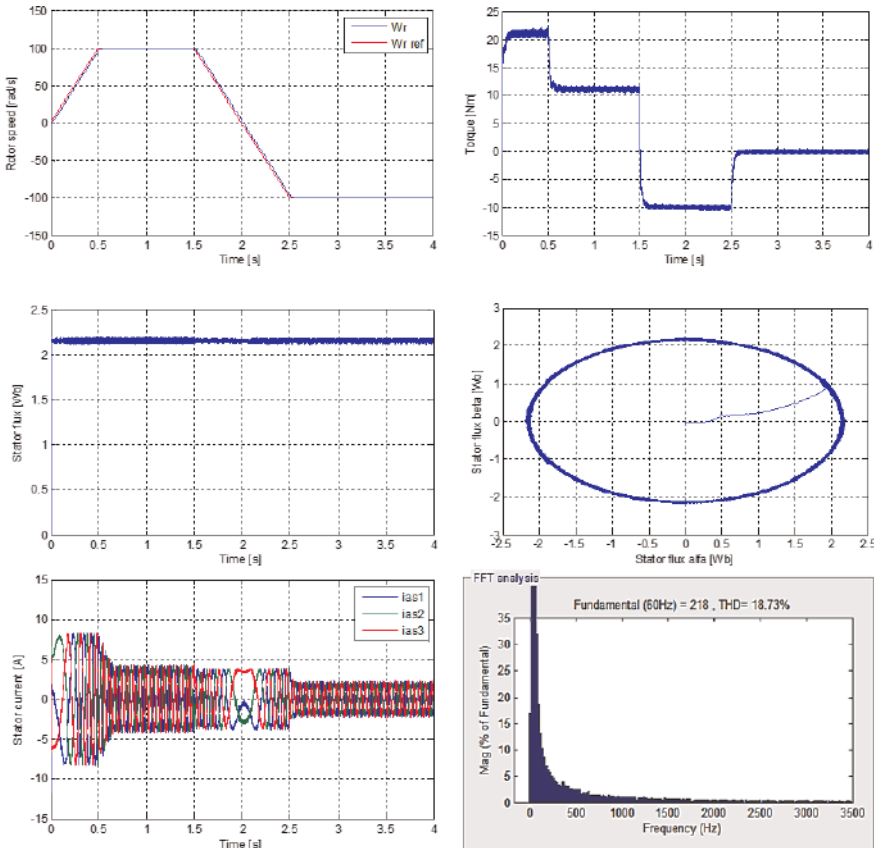


Figure 5. Simulation results of real and estimated speed, torque, flux, and current of three-level DTC-ANN.

with a load torque of 11 Nm. Finally, the direction of rotation of the machine is reversed from 100 rad/s to -100 rad/s at time $t = 2$ s. **Figures 5 and 6** show the simulation results of the three- and five-level DTC control for DSIM.

Simulation results of speed, stator flux, torque, stator current, and stator voltage show the good performance of the three- and five-level DTC-ANN control of DSIM (speed, stability, and precision).

We note that the speed follows its reference value. The electromagnetic torque stabilizes at the value of the nominal torque after a transient regime with rapid response and without exceeding before stabilizing at the value of the applied load torque.

Figure 6 shows that the five-level DTC-ANN control reduces the ripple of the electromagnetic torque, the stator flux, and the THD value compared to that of the three-level DTC-ANN. On the other hand, we note that the speed reaches its reference without exceeding for the two control types. Moreover, the couple follows the load torque. The dynamics of the stator flux are not affected by the application of these load instructions.

The use of multilevel inverter at five levels causes a decrease in the current ripple at the steady state that is to say low peaks than that of the three-level control. However, the results of the simulations shows a good dynamic characteristic of the stator flux in the transient regime for five-level DTC-ANN compared to the three-level DTC-ANN with static errors that are virtually null in both cases of control DTC proposed.

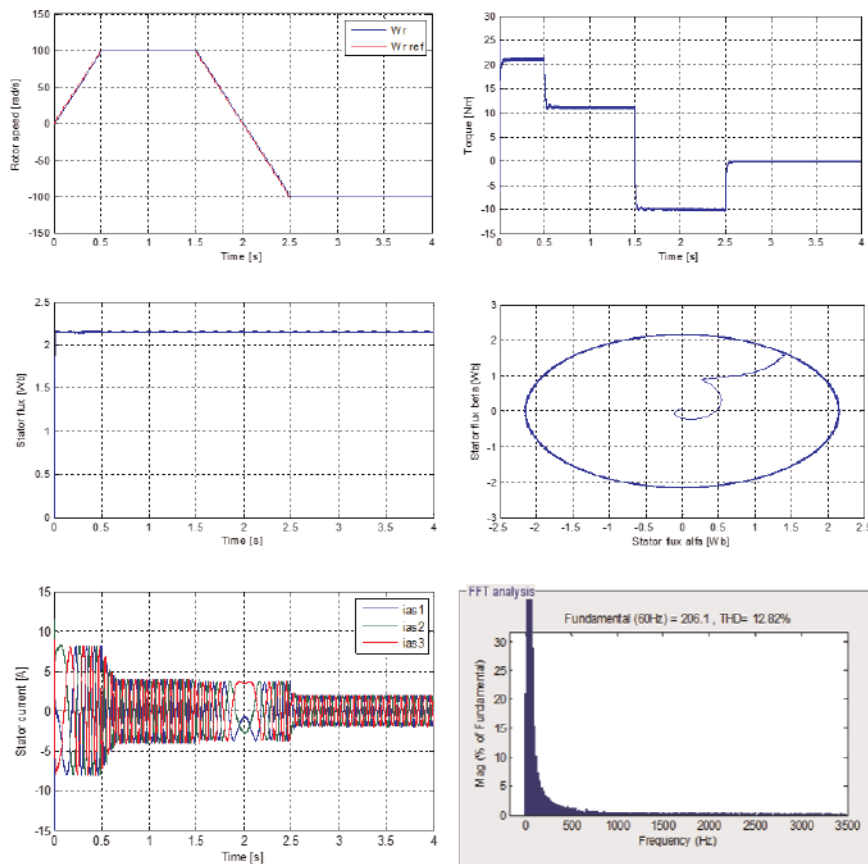


Figure 6. Simulation results of real and estimated speed, torque, flux, and current of five-level DTC-ANN.

Figures 7 and 8 show the simulation results of the three-level and five-level DTC-ANN control for low-speed operation. DSIM is accelerated from standstill to a low reference speed of 10 rad/s, at time $t = 0.5$ s; the DSIM is accelerated again to a reference speed of 100 rad/s. The machine is loaded with a nominal load of 11 Nm. Finally, a reversal of the direction of rotation of the machine from 100 rad/s to -10 rad/s is performed at time $t = 2$ s.

The simulation results show that low-speed operation does not affect the performance of the proposed drive. Indeed, the good reference speed tracking is ensured, with advantages brought by the use of five-level DTC-ANN control, the minimization of torque ripple, and stator flux, which is confirmed by the simulation results.

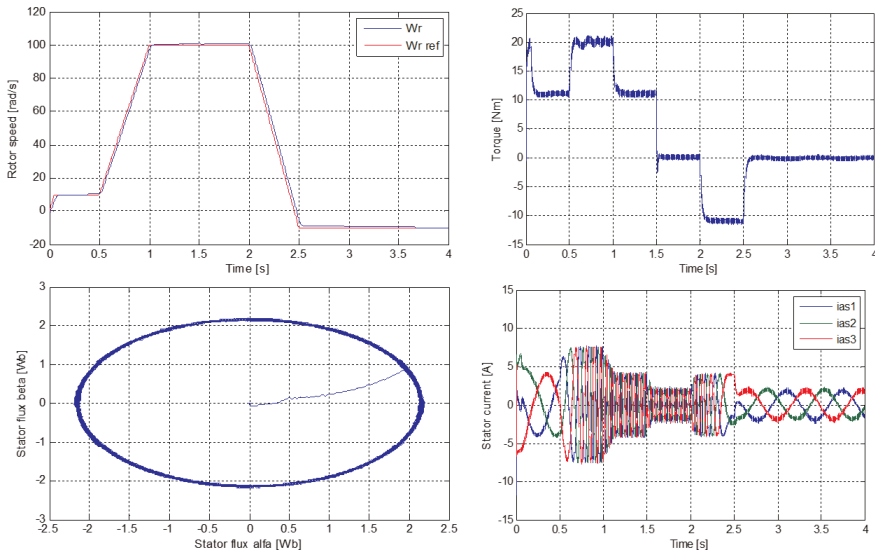


Figure 7. Simulation results of three-level DTC-ANN for low-speed operation.

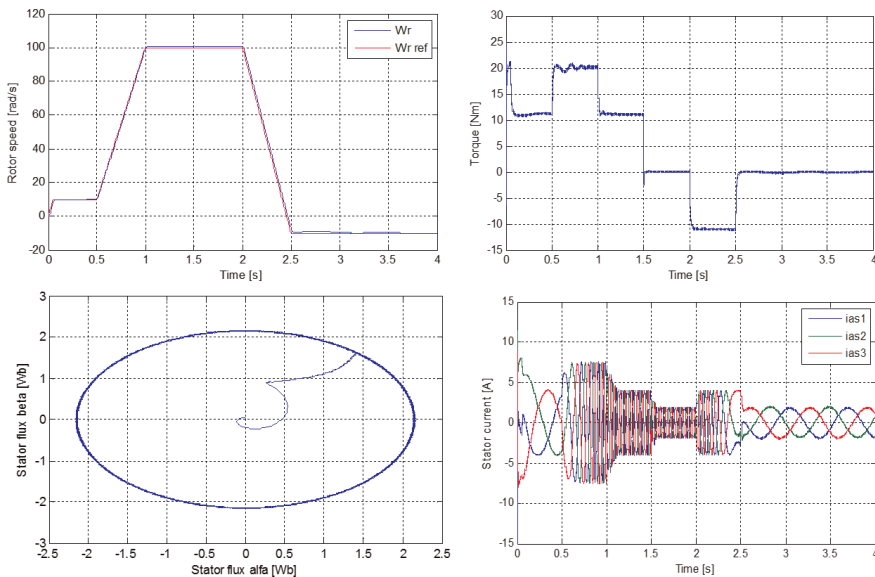


Figure 8. Simulation results of five-level DTC-ANN for low-speed operation.

	THD (%)	Ripples of torque	Ripples of flux
Three-level DTC	18.73	Good	Good
Five-level DTC	12.82	Very good	Very good

Table 3.
The comparison between three-level and five-level DTC-ANN.

In order to know the best type control of DSIM, a comparative study is essential between the two types (three-level DTC-ANN and five-level DTC-ANN). The following table shows the comparison between the two types (**Table 3**).

7. Conclusion

In this chapter, we presented two types of DTC control (three-level DTC-ANN and five-level DTC-ANN) of a DSIM fed by two NPC voltage inverters, and the technique of neural networks was applied to the DTC control. The main advantage of this control is to allow control of the flux and torque of the machine without the need to use a mechanical sensor. The direct torque control strategy is an effective and simple way to control an induction machine. In order to improve the performance of the DSIM (torque ripple reductions, flux, response time, and the THD value of the stator current), simulation tests of the control by variation and inversely of the speed have been presented; the results obtained show that the five-level DTC-ANN control with speed control is very efficient. This shows the effectiveness of the proposed strategy.

Appendix

DSIM parameters

$$\begin{aligned}P_n &= 4.5 \text{ Kw} \\I_n &= 6 \text{ A} \\R_r &= 2.12 \ \Omega \\L_r &= 0.006 \text{ H} \\R_{s1} &= R_{s2} = 1.86 \ \Omega \\L_{s1} &= L_{s2} = 0.011 \text{ H} \\L_m &= 0.3672 \text{ H} \\J &= 0.065 \text{ kg.m}^2 \\k_f &= 0.001 \text{ Nm/rad.}\end{aligned}$$

Author details

Mohamed Haithem Lazreg* and Abderrahim Bentaallah
Faculty of Electrical Engineering, Laboratory of Intelligent Control and Electrical
power Systems (ICEPS), Djillali Liabes University of Sidi Bel Abbes, Algeria

*Address all correspondence to: haitem.31@hotmail.fr

IntechOpen

© 2020 The Author(s). Licensee IntechOpen. This chapter is distributed under the terms of the Creative Commons Attribution License (<http://creativecommons.org/licenses/by/3.0>), which permits unrestricted use, distribution, and reproduction in any medium, provided the original work is properly cited. 

References

- [1] Kirankumar B, Reddy YV, Vijayakumar M. Multilevel inverter with space vector modulation: Intelligence direct torque control of induction motor. *IET Power Electronics*. 2017;**10**:1129-1137
- [2] Nabae A, Takahashi I, Akagi H. A new neutral-point-clamped PWM inverter. *IEEE Transactions on Industrial Applications*. 1981;**IA-17**: 518-523
- [3] Babaei E, Dehqan A, Sabahi M. A new topology for multilevel inverter considering its optimal structures. *Electric Power Systems Research*. 2013; **103**:145-156
- [4] Gupta K, Bhatnagar P. Chapter 2 – Basics of multilevel inverters. In: *Multilevel Inverters Conventional and Emerging Topologies and their Control*; 2018. pp. 21-42
- [5] Meroufel A, Massoum S, Bentaallah A, et al. Double star induction motor direct torque control with fuzzy sliding mode speed controller. *Revue Roumaine des Sciences Techniques - Serie Électrotechnique et Énergétique*. 2017; **62**:31-35
- [6] Taheri A. Harmonic reduction of direct torque control of six-phase induction motor. *ISA Transactions*. 2016;**63**:299-314
- [7] Khedher A, Mimouni MF. Sensorless-adaptive DTC of double star induction motor. *Energy Conversion and Management*. 2010;**51**:2878-2892
- [8] Gadoue SM, Giaouris D, Finch JW. Artificial intelligence-based speed control of DTC induction motor drives — A comparative study. *Electric Power Systems Research*. 2009;**79**:210-219
- [9] Lazreg MH, Bentaallah A. Speed sensorless vector control of double star induction machine using reduced order observer and MRAS estimator. In: *IEEE International Conference on Electrical Engineering (ICEE-B)*; Boumerdes, Algeria; 2017
- [10] Lazreg MH, Bentaallah A. Sensorless fuzzy sliding-mode control of the double-star induction motor using a sliding-mode observer. *Elektrotehniški Vestnik*. 2018;**85**:169-176
- [11] Payami S, Behera RK, Iqbal A. DTC of three-level NPC inverter fed five-phase induction motor drive with novel neutral point voltage balancing scheme. *IEEE Transactions on Power Electronics*. 2018;**33**:1487-1500
- [12] Harina MM, Vanithaa V, Jayakumar M. Comparison of PWM techniques for a three level modular multilevel inverter. *Energy Procedia*. 2017;**117**:666-673
- [13] Figarado S, Sivakumar K, Ramchand R, Das A, Patel C, Gopakumar K. Five-level inverter scheme for an open-end winding induction machine with less number of switches. *IET Power Electronics*. 2010;**3**: 637-647
- [14] Rosmadi A, Nasrudin A, Siti R, Sheikh R, Zaharin A. A five-level diode-clamped inverter with three-level boost converter. *IEEE Transactions on Industrial Electronics*. 2014;**61**: 5155-5163
- [15] Naganathan P, Srinivas S, Ittamveetil H. Five-level torque controller-based DTC method for a cascaded three-level inverter fed induction motor drive. *IET Power Electronics*. 2017;**10**:1223-1230
- [16] Talaeizadeh V, Kianinezhad R, Seyfossadat SG, Shayanfar HA. Direct torque control of six-phase induction motors using three-phase matrix

converter. *Energy Conversion and Management*. 2010;**51**:2482-2491

[17] Usta MA, Okumus HI, Kahveci HA. Simplified three-level SVM-DTC induction motor drive with speed and stator resistance estimation based on extended Kalman filter. *Electrical Engineering*. 2017;**99**:707-720

[18] Barika S, Jaladi KK. Five-phase induction motor DTC-SVM scheme with PI controller and ANN controller. *Procedia Technology*. 2016;**25**:816-823

[19] Zolfaghari M, Taher SA, Munuz DV. Neural network-based sensorless direct power control of permanent magnet synchronous motor. *Ain Shams Engineering Journal*. 2016;**7**:729-740

[20] Douiri MR, Cherkaoui M. Comparative study of various artificial intelligence approaches applied to direct torque control of induction motor drives. *Frontiers in Energy*. 2013;**7**: 456-467

Direct Torque Control Strategies of Induction Machine: Comparative Studies

Cherifi Djamila and Miloud Yahia

Abstract

The direct torque control (DTC) was proposed as an alternative to the vector control in the middle of 1980s for AC machine control. This strategy bases on the direct determination of inverter switching states and offers a simpler scheme and less sensitivity to machine parameters. However, the variable switching frequency of DTC causes high flux and torque ripples which lead to an acoustical noise and degrade the performance of the control technique, especially at low-speed regions. In the objective of improving the performance of DTC for the induction motor, this work addresses the most important points concerning this issue. The reduction of high ripples, which are the major drawbacks, by applying a constant switching frequency using the space vector modulation (SVM) has been done firstly. Then, fuzzy DTC-SVM strategy with adaptive fuzzy-PI speed controller has been proposed. The results of all the discussed aspects of this chapter have been obtained by numerical simulation using MATLAB/Simulink software.

Keywords: induction motor, conventional direct torque control (DTC), space vector modulation, DTC-SVM, fuzzy-PI speed controller

1. Introduction

Advanced control of electrical machines requires an independent control of magnetic flux and torque. For that reason it was not surprising that the DC machine played an important role in the early days of high-performance electrical drive systems, since the magnetic flux and torque are easily controlled by the stator and rotor current, respectively. The introduction of field oriented control meant a huge turn in the field of electrical drives, since with this type of control the robust induction machine can be controlled with a high performance. Later in the 1980s, a new control method for induction machines was introduced: The direct torque control (DTC) method. It was proposed by Takahashi and Depenbrock [1, 2]. It bases on the direct selecting of the switching states to control the voltage source inverter (VSI) through a switching look-up table. Due to the limits of the conventional DTC strategy, especially the high torque and flux ripples problem, various control structures are presented to improve the performances of control, [3, 4]. The constant switching frequency DTC using the space vector modulation (DTC-SVM) is a well discussed solution; in order to improve the DTC-SVM performances, hysteresis comparators of electromagnetic torque and stator flux have been

replaced by PI controllers, [5, 6]. The main drawbacks of DTC-SVM using PI controllers are the sensitivity of the performances to the system-parameter variations and the inadequate rejection of external disturbances and load changes [7–11]. To cope with this disadvantage, it is suggested to replace the conventional regulators used for the speed control, flux, and electromagnetic torque by intelligent controllers by fuzzy logic to make the controls more robust against the disturbances of the parameters of the machine. The aim of this chapter is to design and compare three strategies for the direct torque control (DTC) of induction motor (IM). The first method is a conventional direct torque control (C-DTC) where the torque and the flux are regulated by the hysteresis controllers. The second one is direct torque control by space vector modulation strategy (SVM-DTC) where the torque and flux are regulated by PI controllers. The third one is fuzzy SVM-DTC with adaptive fuzzy-PI speed controller where the torque and flux are regulated by fuzzy logic controllers. The main feature of the proposed (SVM-DTC) strategy is the reduction of torque and flux ripples.

2. Model of induction motor dedicated for direct torque control

The mathematical model of induction motor can be described in the stator fixed reference frame (α, β) (stationary frame) by assuming the rotor and the stator flux as state variables:

$$\frac{dX}{dt} = AX + BU \quad (1)$$

with

$$X = \begin{bmatrix} \phi_{s\alpha} \\ \phi_{s\beta} \\ \phi_{r\alpha} \\ \phi_{r\beta} \end{bmatrix}, A = \begin{bmatrix} -\frac{R_s}{\sigma L_s} & 0 & \frac{MR_s}{\sigma L_r L_s} & 0 \\ 0 & -\frac{R_s}{\sigma L_s} & 0 & \frac{MR_s}{\sigma L_r L_s} \\ \frac{MR_r}{\sigma L_r L_s} & 0 & -\frac{R_r}{\sigma L_r} & -\omega \\ 0 & \frac{MR_r}{\sigma L_r L_s} & \omega & -\frac{R_r}{\sigma L_r} \end{bmatrix}, B = \begin{bmatrix} 1 & 0 \\ 0 & 1 \\ 0 & 0 \\ 0 & 0 \end{bmatrix} \text{ and}$$

$$U = \begin{bmatrix} v_{s\alpha} \\ v_{s\beta} \end{bmatrix} \text{ where}$$

$\phi_{s\alpha}, \phi_{s\beta}, \phi_{r\alpha}, \phi_{r\beta}$ are stator and rotor flux components.

R_s, R_r are stator and rotor resistance.

L_s, L_r are stator and rotor inductance.

M is the mutual stator-rotor inductance.

$\sigma = 1 - \frac{M^2}{L_r L_s}$ is the Blondel's coefficient.

ω is the machine speed ($\omega = p\Omega = \omega_s - \omega_r$ and p is the pole pair number).

The rotor motion can be described by:

$$J \frac{d\Omega}{dt} = T_{em} - T_L - f\Omega \quad (2)$$

where J is the motor inertia, T_{em} is the electromagnetic torque, T_L is the load torque, and f is the friction coefficient.

3. Two-level voltage source inverter (VSI) model

Two-level three-phase voltage source inverter (VSI) is considered as a mature technology and becoming an industrial standard for the demand for energy saving. The output phase voltages are produced by the rectifier (V_{dc}) is delivered to the inverter input, which, thanks to controlled transistor switches, converts this voltage to three-phase AC voltage signal with wide range variable voltage amplitude and frequency.

The type of the used switches depends on the power of the inverter and switching frequency. In the most applications, IGBT transistors with antiparallel diodes are so helpful.

The model of two-level voltage inverter is shown in **Figure 1**.

Figure 1 shows the two-level three-phase voltage source inverter (VSI) with six transistor switches, S1–S6, and a dc constant voltage source V_{dc} connecting a three-phase load.

The voltage vector is generated by the following equation:

$$\vec{V}_s = \sqrt{\frac{2}{3}} V_{dc} \left[S_a + S_b e^{j\frac{2\pi}{3}} + S_c e^{j\frac{4\pi}{3}} \right] \quad (3)$$

where S_a , S_b , and S_c are three-phase inverter switching functions, which can take a logical value of either 0 or 1.

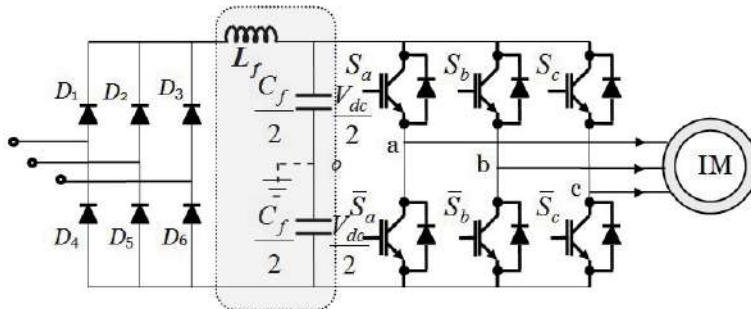


Figure 1.
 Three-phase VSI fed star-connected induction machine.

4. Principles of direct torque control

Direct torque control principle was introduced in the late 1980s by [1, 2]. It achieves a decoupled control of the stator flux and the electromagnetic torque in the stationary frame (α, β), and it allows induction machines to have an accurate and fast electromagnetic torque response. It uses a switching table for the selection of an appropriate voltage vector. The selection of the switching states is related directly to the variation of the stator flux and the torque of the machine. Hence, the selection is made by restricting the flux and torque magnitudes within two hysteresis bands. Those controllers ensure a separated regulation of both of these quantities [12–14]. The inputs of hysteresis controllers are the flux and the torque errors as well as their outputs determine the appropriate voltage vector for each commutation period.

5. Estimation of stator flux and electromagnetic torque

5.1 Control of stator flux

Basing on the induction motor model in stationary frame, the stator flux equation can be expressed as follows [15–19]:

$$\begin{cases} \phi_{s\alpha} = \int (v_{s\alpha} - R_s i_{s\alpha}) dt \\ \phi_{s\beta} = \int (v_{s\beta} - R_s i_{s\beta}) dt \end{cases} \quad (4)$$

Considering that the control of the switches of the inverter is done by control period (or sampling) T_e and that at each of these periods the states S_a , S_b , and S_c are kept constant, the method of numerical integration of the rectangles makes it possible to obtain an expression of the sample $k + 1$ of the stator flux in the following form:

$$\begin{cases} \phi_{s\alpha}(k+1) = \phi_{s\alpha}(k) + (v_{s\alpha}(k) - R_s i_{s\alpha}(k)) T_e \\ \phi_{s\beta}(k+1) = \phi_{s\beta}(k) + (v_{s\beta}(k) - R_s i_{s\beta}(k)) T_e \end{cases} \quad (5)$$

A vector inscription of this expression can be given by:

$$\vec{\phi}_s(k+1) = \vec{\phi}_s(k) + \left(\vec{V}_s(k) - R_s \vec{I}_s(k) \right) T_e \quad (6)$$

We can neglect the stator resistance voltage drop compared to V_s for high speed regions. Then Eq. (6) can be written as:

$$\vec{\phi}_s(k+1) = \vec{\phi}_s(k) + \vec{V}_s(k) T_e \quad (7)$$

Eq. (7) means that the stator flux can be changed by the application of stator voltage during a time k . The stator flux vector's extremity moves in direction given by the voltage vector and making a circular trajectory.

A two-level hysteresis comparator is used for flux regulation. It allows to drop easily the flux vector extremity within the limits of the two concentric circles with close radius. The choice of the hysteresis bandwidth depends on the switching frequency of the inverter **Figures 2** and **3**.

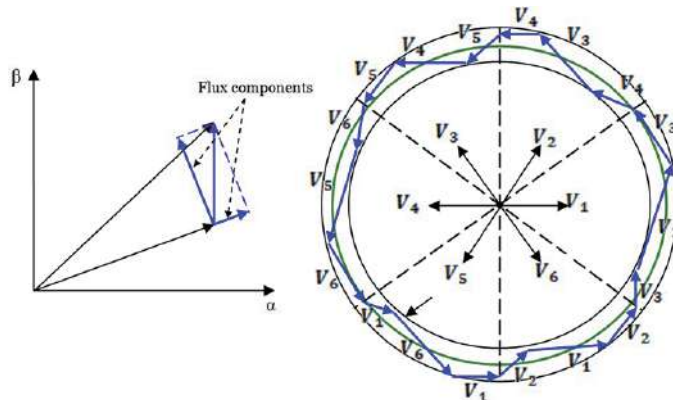


Figure 2.
Evolution of stator flux vector in the complex plan.

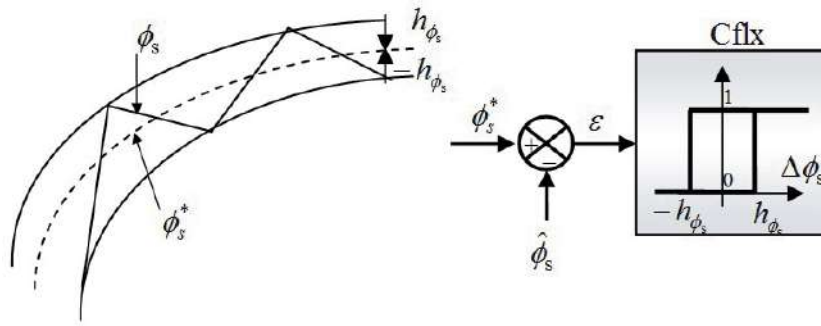


Figure 3.
 Two-level hysteresis comparator for stator flux control.

The logical outputs of the flux controller are defined as:

$$\begin{aligned} \text{Cflx} &= 1 && \text{if } \Delta\phi_s > h_{\phi_s} \\ \text{Cflx} &= 0 && \text{if } \Delta\phi_s \leq -h_{\phi_s} \end{aligned} \quad (8)$$

where h_{ϕ_s} is hysteresis band of stator flux.

The stator flux error is defined by the difference between the reference value of flux and the actual estimated value:

$$\Delta\phi_s = |\phi_s^*| - |\phi_s| \quad (9)$$

5.2 Control of electromagnetic torque

During one sampling period, the rotor flux vector is supposed invariant. The rotor and stator flux vectors are linked by the following relation:

$$\phi_r = \frac{M}{L_s} \cdot \frac{1}{1 + j\sigma\omega T_r} \phi_s \quad (10)$$

The angle between these two vectors is given by:

$$\delta = \text{Arctan } g(\sigma\omega T_r) \quad (11)$$

Finally, between the modules of the two flux vectors, we have the following relation:

$$|\phi_r| = \frac{M}{L_s} \cdot \frac{1}{\sqrt{1 + (\sigma\omega T_r)^2}} |\phi_s| \quad (12)$$

The general expression of electromagnetic torque is given by:

$$T_{em} = p \frac{M}{\sigma L_s L_r} [\phi_s \cdot \phi_r^*] \quad (13)$$

$$T_{em} = p \frac{M}{\sigma L_s L_r} \phi_s \cdot \phi_r \text{Sin}(\delta) \quad (14)$$

where:

p is the number of poles pairs.

ϕ_s, ϕ_r are stator and rotor flux vectors.

δ angle between the stator and rotor flux vectors.

From expression (14), it is clear that the electromagnetic torque is controlled by the stator and rotor flux amplitudes. If those quantities are maintaining constant, the torque can be controlled by adjusting the load angle δ .

The torque regulation can be realized using three-level hysteresis comparator. (Figure 4).

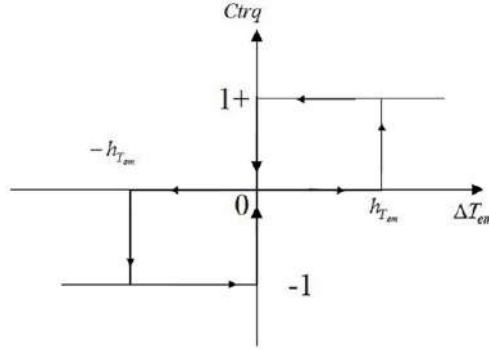


Figure 4.
Three-level hysteresis comparator for electromagnetic torque control.

The logical outputs of the torque controller are defined as:

$$\begin{aligned} \text{Ctrq} &= 1 && \text{if } \Delta T_{em} > h_{T_{em}} \\ \text{Ctrq} &= 0 && \text{if } -h_{T_{em}} \leq \Delta T_{em} \leq h_{T_{em}} \\ \text{Ctrq} &= -1 && \text{if } \Delta T_{em} < -h_{T_{em}} \end{aligned} \quad (15)$$

where $h_{T_{em}}$ is hysteresis band of torque.

The torque error is defined by the difference between the references values of the torque and the actual estimated values:

$$\Delta T_{em} = T_{em}^* - T_{em} \quad (16)$$

6. Estimation of stator flux and electromagnetic torque

6.1 Stator flux estimation

The amplitude of the stator flux is estimated from its two-phase components $\phi_{s\alpha}$ and $\phi_{s\beta}$:

$$\phi_s = \sqrt{\phi_{s\alpha}^2 + \phi_{s\beta}^2} \quad (17)$$

Or $\phi_{s\alpha}$ and $\phi_{s\beta}$ are estimated using Eq. (4) which requires knowledge of the components of the stator current vector $i_{s\alpha}$ and $i_{s\beta}$ and that of the vector stator voltage $v_{s\alpha}$ and $v_{s\beta}$.

The stator voltage components $v_{s\alpha}$ and $v_{s\beta}$ are obtained by applying Concordia transformation on the output voltage of the three-phase VSI which are given by:

$$\begin{cases} v_{s\alpha} = \sqrt{\frac{2}{3}} V_{dc} \left[S_a - \frac{1}{2}(S_b + S_c) \right] \\ v_{s\beta} = \sqrt{\frac{1}{2}} V_{dc} (S_b - S_c) \end{cases} \quad (18)$$

The stator currents components $i_{s\alpha}$ and $i_{s\beta}$ can be obtained also by applying Concordia transformation on the measured currents:

$$\begin{cases} i_{s\alpha} = \sqrt{\frac{3}{2}} i_{sa} \\ i_{s\beta} = \frac{1}{\sqrt{2}} (i_{sb} - i_{sc}) \end{cases} \quad (19)$$

6.2 Electromagnetic torque estimation

The produced electromagnetic torque of the induction motor can be determined using the cross product of the stator quantities (i.e., stator flux and stator currents). The torque formula is expressed as the following:

$$T_{em} = p(\phi_{s\alpha} i_{s\beta} - \phi_{s\beta} i_{s\alpha}) \quad (20)$$

7. Switching table construction and control algorithm design

To maintain a decoupled control, a pair of hysteresis comparators receives the stator flux and torque errors as inputs. Then, the comparators outputs determine the appropriate voltage vector selection. However, the choice of voltage vector is not only depending on the output of hysteresis controllers but on the position of stator flux vector also. Thus, the circular stator flux vector trajectory will be divided into six symmetrical sectors (**Table 1**).

For each sector, the vectors (V_i and V_{3+i}) are not considered because both of them can increase or decrease the torque in the same sector according to the position of flux vector on the first or the second sector. If the zero vectors V_0 and V_7 are selected, the stator flux will stop moving, its magnitude will not change, and the electromagnetic torque will decrease, but not as much as when the active voltage vectors are selected. The resulting look-up table for DTC which was proposed by Takahashi is presented in **Table 2**.

	Increases	Decreases
ϕ_s	V_{i-1} and V_{i+1}	V_{i+2} and V_{i-2}
T_{em}	V_{i+1} and V_{i+2}	V_{i-1} and V_{i-2}

Table 1.
Generalized switching table.

Flux	Torque	1	2	3	4	5	6	Comparator
Cflx = 1	Ctrq = 1	V_2	V_3	V_4	V_5	V_6	V_1	Two-level
	Ctrq = 0	V_7	V_0	V_7	V_0	V_7	V_0	
	Ctrq = -1	V_6	V_1	V_2	V_3	V_4	V_5	Three-level
Cflx = 0	Ctrq = 1	V_3	V_4	V_5	V_6	V_1	V_2	Two-level
	Ctrq = 0	V_0	V_7	V_0	V_7	V_0	V_7	
	Ctrq = -1	V_5	V_6	V_1	V_2	V_3	V_4	Three-level

Table 2.
Look-up table for basic direct torque control.

is passed through a gain block (tracking time constant T_i) before arriving as feedback to the integrator. As well flux and torque hysteresis controllers, look-up switching table, an association of VSI-Induction motor, voltage and current calculation blocks with 3/2 (Concordia) transformation and flux/torque estimators with position/sector determination.

9. Constant switching frequency direct torque control using SVM

The conventional direct torque control has several disadvantages, among which the variable switching frequency and the high level of ripples. Consequently, they lead to high-current harmonics and an acoustical noise and they degrade the control performance especially at low speed values. The ripples are affected proportionally by the width of the hysteresis band. However, even with choosing a reduced bandwidth values, the ripples are still important due to the discrete nature of the hysteresis controllers. Moreover, the very small values of bandwidths increase inverter switching frequency. In order to overcome these drawbacks, most of the studies presented in the literature have been oriented towards modification in the conventional DTC method by the introduction of a vector modulator [21, 22]. The vector PWM technique (SVM) is used to apply a voltage vector with a fixed switching frequency. The control system consists of replacing the switching table and the hysteresis comparators with proportional and integrating controllers (PI) for controlling the stator flux and the electromagnetic torque, [6, 23–27]. The main drawbacks of DTC-SVM using PI controllers are the sensitivity of the performances to the system-parameter variations and the inadequate rejection of external disturbances and load changes [28, 29]. To cope with this disadvantage, it is suggested to replace the conventional regulators used for the speed control, flux, and electromagnetic torque by intelligent controllers by adaptive fuzzy-PI and fuzzy logic to make the control more robust against the disturbances of the parameters of the machine.

9.1 Space vector modulation algorithm

This technique is much requested in the field of control in that the reference voltages are given by a global control vector approximated over a modulation period T_s . The principle of SVM is the prediction of inverter voltage vector by the projection of the reference vector V_s^* between adjacent vectors corresponding to two non-zero switching states. For two-level inverters, the switching vector diagram forms a hexagon divided into six sectors, each one is expanded by 60° as shown in **Figure 7**.

The application time for each vector can be obtained by vector calculations, and the rest of the time period will be spent by applying the null vector.

When the reference voltage is in sector 1 (**Figure 8**), it can be synthesized by using the vectors V_1 , V_2 , and V_0 (zero vector).

The determination of times T_1 and T_2 corresponding to voltage vectors are obtained by simple projections (**Figure 9**).

$$T_1 = \frac{\sqrt{6} \cdot V_{s\alpha} - \sqrt{2} \cdot V_{s\beta}}{2V_{dc}} T \quad (21)$$

$$T_2 = \frac{\sqrt{2} \cdot V_{s\beta}}{V_{dc}} \cdot T \quad (22)$$

where V_{dc} is the DC bus voltage.

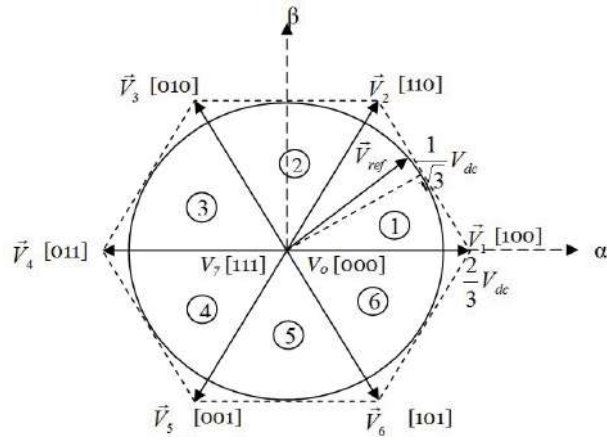


Figure 7.
Diagram of voltage space vector.

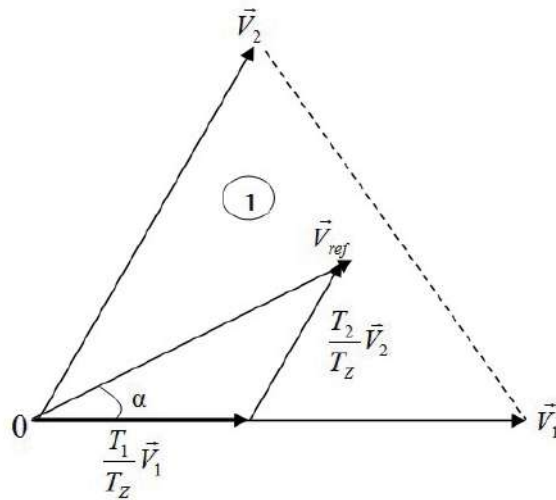


Figure 8.
Reference vector as a combination of adjacent vectors at sector 1.

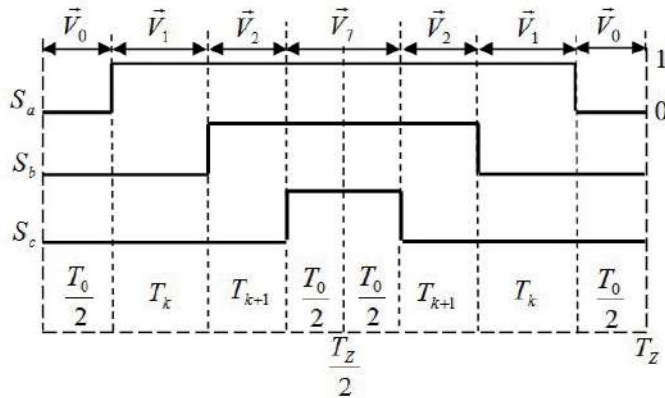


Figure 9.
Switching times of sector 1.

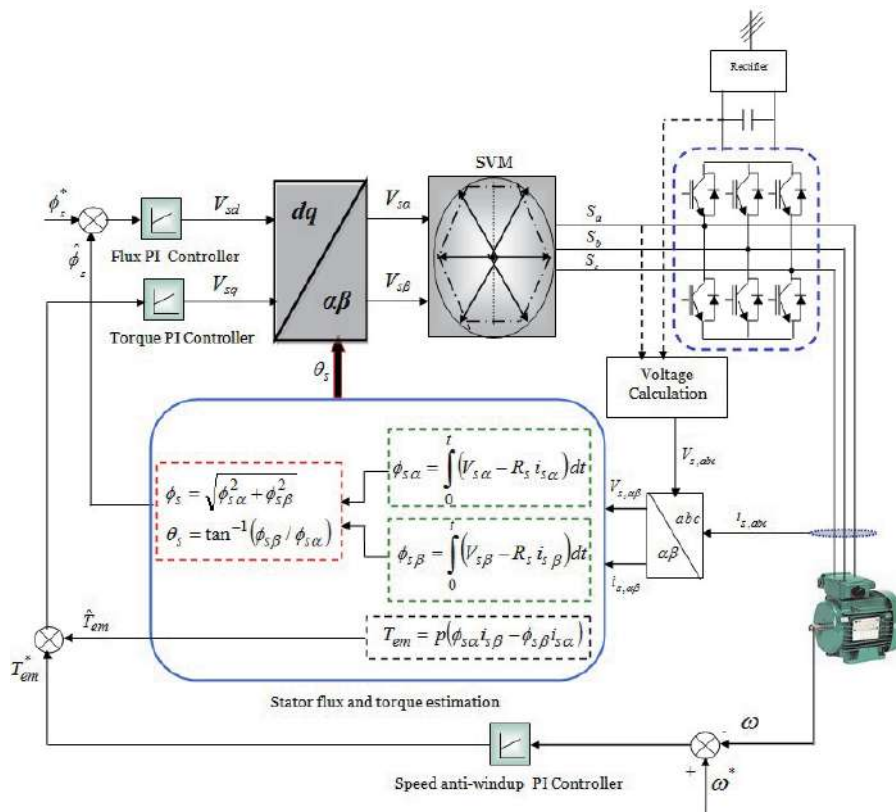


Figure 10. Global control scheme of SVM-direct torque control with PI controller.

T_1 , T_2 , and T_0 are the corresponding application times of the voltage vectors, respectively. T_z is the sampling time.

Figure 10 shows the global block diagram of DTC with SVM.

9.2 Principle of fuzzy direct torque control

The complete block diagram DTC-SVM improvement of induction motor drive with fuzzy logic controller is shown in **Figure 11**. The practical difficulty with PI controllers has been addressed in the previous section. The PI controllers are being replaced by fuzzy logic controllers that generates the module and the voltage vector angle in order to bring the stator flux and the electromagnetic torque to references optimally; this vector is used by a PWM control vector to generate the pulses for the control of the switches of the inverter, and PI speed controller is replaced by the adaptive fuzzy-PI speed controller to offer a good insensitivity to parameter variations, to get better response in external disturbance rejection and fast dynamics.

9.2.1 Selecting the position of the voltage vector

The position of the reference voltage vector with respect to the stator flux vector must be chosen so as to maintain the stator flux and the electromagnetic torque in an optimal error band around their reference value. The errors of torque and flux are multiplied by “scales factors” to obtain standardized sizes and functions. These

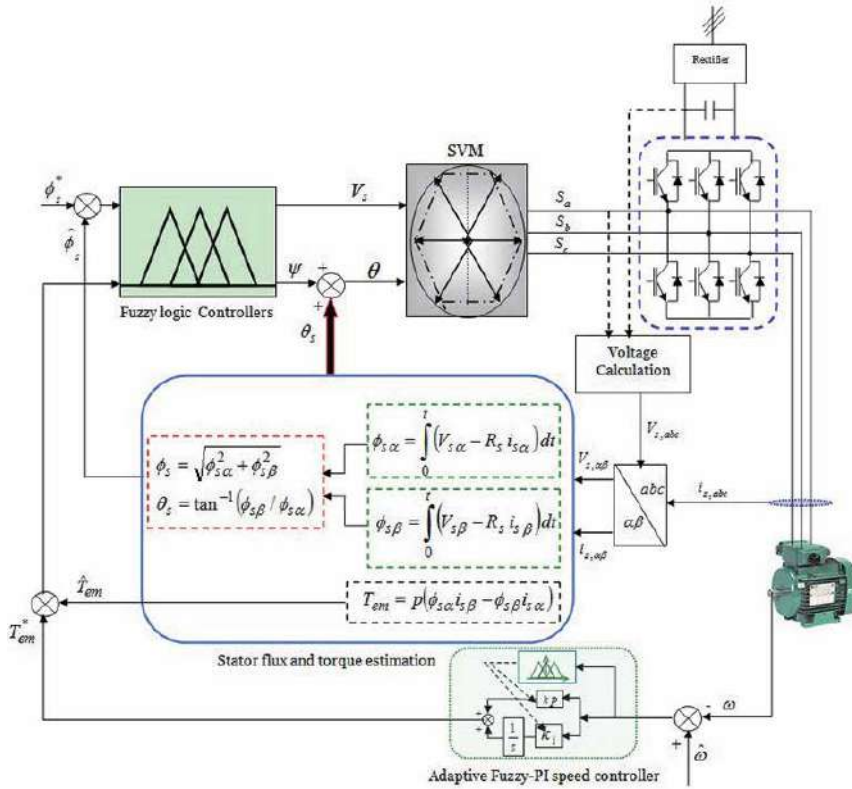


Figure 11. Global control scheme of SVM-direct torque control with fuzzy logic controllers and adaptive fuzzy-PI speed controller.

values are used by the fuzzification block to be transformed into fuzzy values. These are used by the block fuzzy control rules after defuzzification; the value of (ψ) which must be added to the angle of the stator flux [30–32] (**Figure 12**).

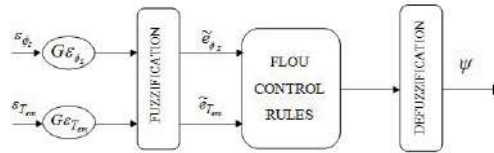


Figure 12. Controller structure for estimating the angle (ψ).

9.2.2 Selection of the voltage vector magnitude

The voltage vector module must be selected to minimize the error of torque and flux. A fuzzy logic controller is designed to generate the appropriate voltage vector magnitude (**Figure 13**).

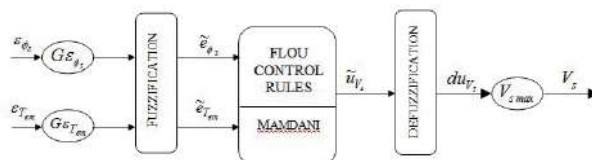


Figure 13. Controller structure for voltage vector module estimation.

9.2.3 Selection of the voltage vector magnitude

The voltage vector obtained from the characteristic comes to the vector modulation $|\vec{V}_s| = f(\varepsilon_{T_{em}})$ which in turn generates the states, and switches using V_α , V_β the following algorithm:

Calculate the biphasic components of the desired voltage vector using the following equations [30–32]:

$$\begin{cases} V_{s\alpha} = V_s \cos(\theta) \\ V_{s\beta} = V_s \sin(\theta) \end{cases} \quad (23)$$

- Calculation of the area where the desired voltage vector is.
- Get the switching vectors and their operating cycle. Then calculate the operating cycle of the null switching vector ($t_0 = 1 - t_1 - t_2$).
- Calculation of the relative position of the clock (PRH) in the sampling time by using the following equations:

$$\text{PRH} = \text{Rem}(t/T_s)/T_s. \quad (24)$$

9.2.4 The speed control of the IM by an adaptive fuzzy-PI controller

In what follows, we show the synthesis and description of the adaptation of the PI controller by a fuzzy system method:

The fuzzy inference mechanism adjusts the PI parameters and generates new parameters during the process control. It enlarges the operating area of the linear controller (PI) so that it also works with a nonlinear system [33, 34].

The inputs of the fuzzy adapter are the error (e) and the derivative of error (Δe); the outputs are the normalized value of the proportional action (k'_p) and the normalized value of the integral action (k'_i).

The normalization PI parameters are given by:

$$k'_p = (k_p - k_{p \min}) / (k_{p \max} - k_{p \min}) \quad (25)$$

$$k'_i = (k_i - k_{i \min}) / (k_{i \max} - k_{i \min}) \quad (26)$$

The parameters k'_p and k'_i are determined by a set of fuzzy rules of the form:

$$\text{If } e \text{ is } A_i \text{ and } \Delta e \text{ is } B_i, \text{ then } k'_p \text{ is } C_i, \text{ and } k'_i \text{ is } D_i \quad (27)$$

where A_i , B_i , C_i , and D_i are fuzzy sets on corresponding supporting sets.

The associated fuzzy sets involved in the fuzzy control rules are defined as follows:

PB	Positive big	NB	Negative big	B	Big
PM	Positive medium	NM	Negative medium	ZE	Zero
PS	Positive small	NS	Negative small	S	Small

The membership functions for the fuzzy sets corresponding to the error e and Δe and the adjusted proportional and integral terms (k'_p and k'_i) are defined in **Figures 14** and **15**.

By using the membership functions shown in **Figure 15**, we satisfy the following condition.

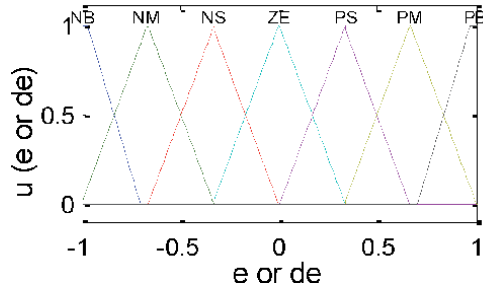


Figure 14.
Membership functions e and Δe .

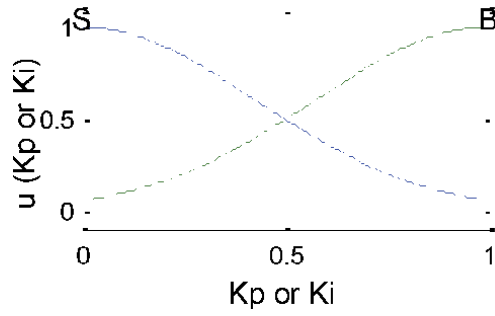


Figure 15.
Membership functions k'_p and k'_i .

$$\sum_1^m v_i = 1 \quad (28)$$

The fuzzy outputs k'_p and k'_i can be calculated by the center of area defuzzification as:

$$[k'_p, k'_i] = \frac{\sum_{i=1}^3 w_i c_i}{\sum_{i=1}^3 w_i} = \frac{[c_1 \dots c_2] \begin{bmatrix} w_1 \\ \vdots \\ w_2 \end{bmatrix}}{\sum_{i=1}^2 w_i} = v^T W \quad (29)$$

		e					
Δe	NB	NM	NS	ZE	PS	PM	PB
NB	B	B	B	B	B	B	B
NM	S	B	B	B	B	B	S
NS	S	S	B	B	B	S	S
ZE	S	S	S	B	S	S	S
PS	S	S	B	B	B	S	S
PM	S	B	B	B	B	B	S
PB	B	B	B	B	B	B	B

Table 3.
Fuzzy rule base for computing k'_p .

Δe	e						
	NB	NM	NS	ZE	PS	PM	PB
NB	B	B	B	B	B	B	B
NM	B	S	S	S	S	S	B
NS	B	B	S	S	S	B	B
ZE	B	B	B	S	B	B	B
PS	B	B	S	S	S	B	B
PM	B	S	S	S	S	S	B
PB	B	B	B	B	B	B	B

Table 4.
 Fuzzy rules base for computing k'_i .

where $C = [c_1 \dots c_2]$ is the vector containing the output fuzzy centers of the membership functions, $W = [w_1 \dots w_2] / \sum_{i=1}^2 w_i$ is the firing strength vector, and v_i represents the membership value of the output k'_p or k'_i to output fuzzy set i .

Once the values of k'_p and k'_i are obtained (**Tables 3 and 4**), the new parameters of PI controller is calculated by the following equations:

$$k_p = (k_{p \max} - k_{p \min})k'_p + k_{p \min} \quad (30)$$

$$k_i = (k_{i \max} - k_{i \min})k'_i + k_{i \min} \quad (31)$$

10. Simulation results

The DTC control algorithms have been simulated by MATLAB/Simulink software. A comparative study between the three strategies for the direct torque control (DTC) of induction motor (IM) is presented. The first method is a conventional direct torque control (C-DTC) where the torque and the flux are regulated by the hysteresis controllers. The second one is direct torque control by space vector modulation strategy (SVM-DTC) where the torque and flux are regulated by PI controllers. The third one is fuzzy SVM-DTC with adaptive fuzzy-PI speed controller where the torque and flux are regulated by fuzzy logic controllers is presented. The simulation has been conducted for a three-phase 1.5 kW squirrel-cage induction motor with characteristics given in the appendix. The starting up and the steady states of the controlled motor with load introduction are presented. For the classical DTC, the chosen bandwidths of the hysteresis controllers are ± 0.01 Wb for flux and ± 0.1 Nm for torque.

This section presents the starting up state of the induction motor according to speed step reference of 1000 rpm. Then, a load of 10 Nm is suddenly applied between ($t = 1$ s) and ($t = 2$ s).

Figures 16 and 17 show, respectively, rotor speed, torque, stator phase current i_{sa} , flux magnitude, and the circular trajectory.

Figures 16 and 17(a) illustrate the comparison between speed responses of conventional DTC and SVM-DTC-PI, according to the speed reference step of 1000 rpm. The load disturbance has been introduced between ($t = 1$ s) and ($t = 2$ s). The results of **Figure 16** show that the conventional DTC technique gives a good dynamic at starting up. We can notice that the speed regulation loop rejects the applied load disturbance quickly. The SVM-DTC-PI in **Figure 17(a)** kept the same

fast speed response of DTC strategy. Since the same PI speed controller is used for both schemes, there is no difference in the transient response.

Then, the results illustrate the torque responses with load application. The figures show that at the beginning the speed controller (PI anti-windup) operates the system at the physical limit. It can be seen clearly that the constant switching frequency-based DTC strategy in **Figure 17(a)** has a reducer ripples level owing to the use of SVM compared to the conventional DTC in **Figure 16**, where it is observed that the high torque ripples exceed the hysteresis boundary. Next, the

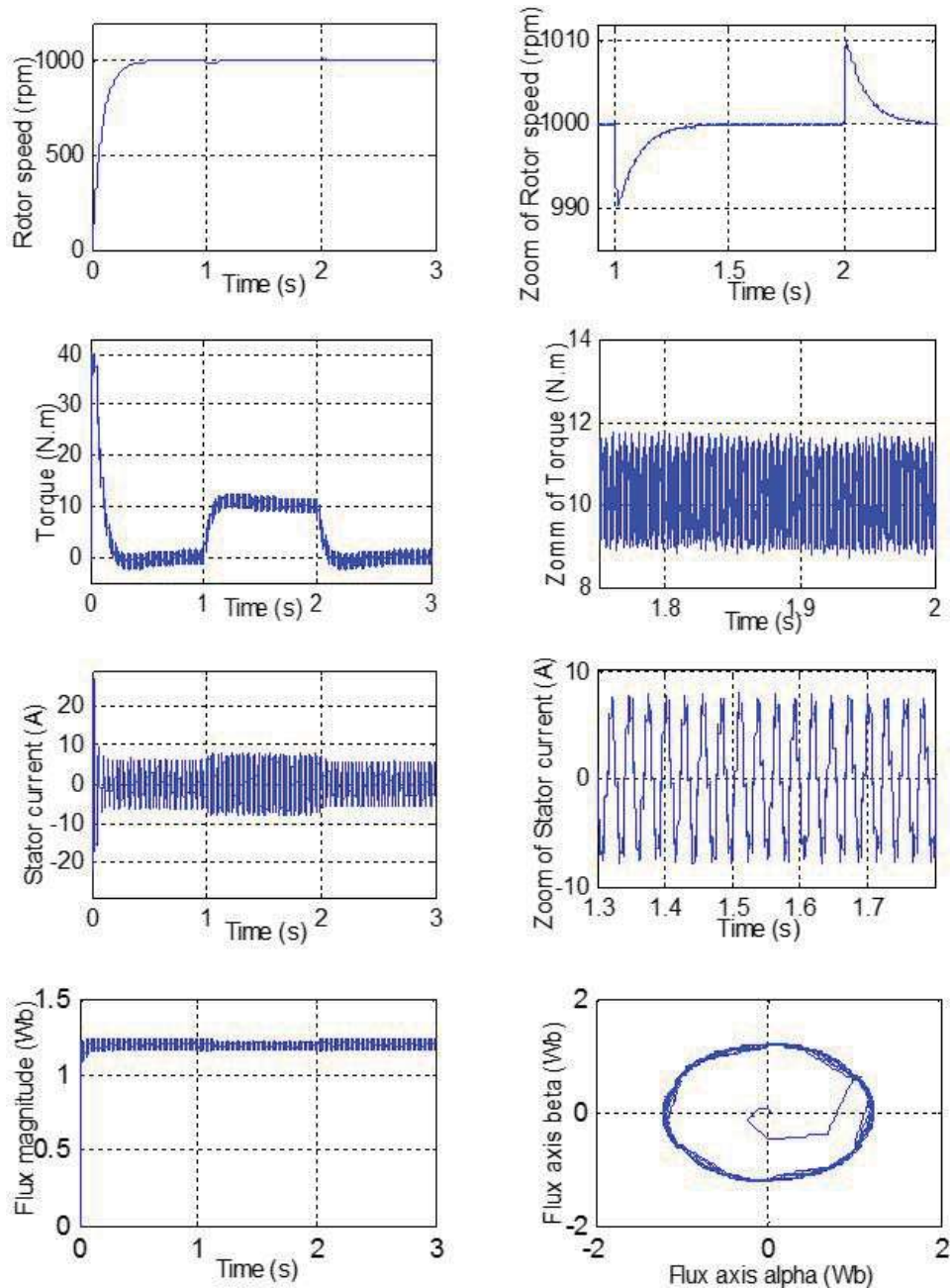


Figure 16. Simulation results of the classical DTC control applied to IM.

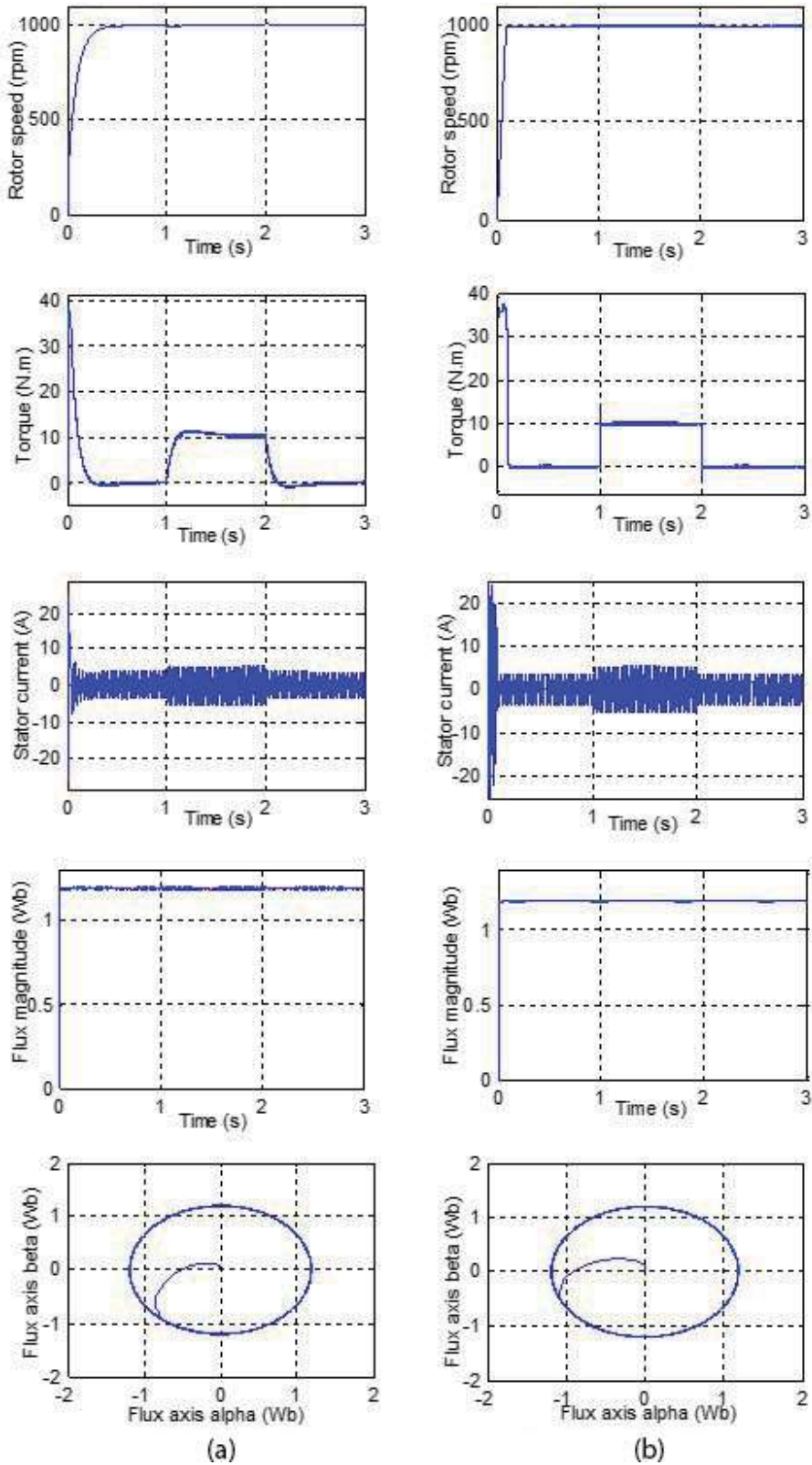


Figure 17. Simulation results of the SVM-DTC control applied to IM. (a) SVM-DTC-PI. (b) SVM-DTC-Fuzzy.

stator phase current with zoom is presented. The conventional DTC in **Figure 16** shows a chopped sinusoid waveform of current which indicates a high harmonic level, while SVM-DTC in **Figure 17(a)** shows a smoother sinusoid waveform. After that, the results exhibit the magnitude of stator flux evolution and circular trajectory. It is clear that the flux ripples of the conventional DTC have exceeded the hysteresis boundary. The magnitude and the trajectory illustrate that the flux takes a few steps before reaching the reference value (1.2 Wb) at the starting stage due to the zone's changing.

The simulation in **Figure 17(b)** shows that the SVM-DTC-fuzzy has better performance than those obtained by both other DTC strategies (conventional and SVM-PI). There is an appreciable decrease in the start-up response time; we can notice that the speed regulation loop rejects the applied load disturbance very quickly which proves the performance of adaptive fuzzy-PI controller as well as a significant attenuation of the ripples of the torque and of the sinusoidal current without any ripple in the steady state.

11. Conclusion

The main objective of this chapter is the improvement of the performance of an induction motor drive controlled by DTC. The objective of this improvement is to minimize the ripples of the couple and the flux of the IM on the one hand and the decrease of the switching frequency of the inverter on the other hand. In this context, a comparative analysis between different DTC strategies has been presented. This chapter began by explaining the principle of the conventional DTC, SVM-DTC-PI, and SVM-DTC-fuzzy with adaptive Fuzzy-PI speed controller. The chapter presents later a discussion based on the simulation results presented in the same work. The synthesis of this simulation study reveals advantages of SVM-DTC-fuzzy scheme compared to the two strategies: conventional DTC and SVM-DTC-PI. It has been observed by comparing the torque, speed, and stator flux characteristics that the method SVM-DTC-fuzzy is better. It is clear that the current is sinusoidal without any ripple in the steady state and torque ripples are reduced. In order to improve the SVM-DTC-fuzzy to have better performances, this method has been associated to the adaptive fuzzy-PI speed controller. This association makes the induction motor-based DTC perform more and more stable; there is an appreciable decrease in the start-up response time; we can notice that the speed regulation loop rejects the applied load disturbance very quickly.

A. IM motor parameters

Item	Symbol	Data
IM mechanical power	P_w	1.5 kw
Nominal speed	ω	1420 rpm
Nominal frequency	f	50 Hz
Pole pair number	P	2
Stator resistance	R_s	4.85 Ω
Rotor resistance	R_r	3.805 Ω
Stator self-inductance	L_s	274 mH

Item	Symbol	Data
Rotor self-inductance	L_r	274 mH
Mutual inductance	L_m	258 mH
Moment of inertia	J	0.031 kg m ²
Friction coefficient	F	0.00114 kg m ² /s

Author details

Cherifi Djamila* and Miloud Yahia
GACA Laboratory, University of Dr Moulay Tahar, Saida, Algeria

*Address all correspondence to: d_cherifi@yahoo.fr

IntechOpen

© 2020 The Author(s). Licensee IntechOpen. This chapter is distributed under the terms of the Creative Commons Attribution License (<http://creativecommons.org/licenses/by/3.0>), which permits unrestricted use, distribution, and reproduction in any medium, provided the original work is properly cited. 

References

- [1] Takahashi, Noguchi T. A new quick-response and high-efficiency control strategy of an induction motor. *IEEE Transactions on Industry Applications.*, Vol.22, No.5, pp.820–827, 1986. DOI: 10.1109/TIA.1986.4504799
- [2] Depenbrock M. Direct self control (DSC) of inverter fed induction machine. *IEEE Transactions on Power Electronics.* 1988;3(4):420-429. DOI: 10.1109/63.17963
- [3] Ammar A, Benakcha A, Bourek A. Closed loop torque SVM-DTC based on robust super twisting speed controller for induction motor drive with efficiency optimization. *International Journal of Hydrogen Energy.* 2017:1-13. DOI: 10.1016/j.ijhydene.2017.04.034
- [4] Lazim MT, Al-Khishali MJM, Al-Shawi AI. Space vector modulation direct torque speed control of induction motor. *Procedia Computer Science.* 2011;5:505-512. DOI: 10.1016/j.procs.2011.07.065
- [5] Habetler Thomas G, Profumo F, Pastorelli M, Tolbert Leon M. Direct torque control of induction machines using space vector modulation. *IEEE Transactions on Industry Applications.* 1992;28(5):1045-1053. DOI: 10.1109/28.158828
- [6] Hassan Farhan R, Nadia Tan ML, Koh SP, Abdalla AN, Chong KH, Tiong SK. DTC-SVM based on PI torque and PI flux controllers to achieve high performance of induction motor. *Research Journal of Applied Sciences, Engineering and Technology.* 2014;7(4):875-891. DOI: 10.19026/rjaset.7.330
- [7] Krim S, Gdaim S, Mtibaa A, Mimoun MF. FPGA-based DTC-SVM: A comparative study between two approaches. *IEEE.* 2016. DOI: 10.1109/CEIT.2016.7929060
- [8] Yu H, Chen Z. Three-phase induction motor DTC-SVPWM scheme with self-tuning PI-type fuzzy controller. *International Journal of Computer and Communication Engineering.* 2015;4(3). DOI: 10.17706/IJCCE.2015.4.3.204-210
- [9] Ben Salem F, Derbel N. Direct torque control of induction motors based on discrete space vector modulation using adaptive sliding mode control. *International Journal of Electric Power Components and Systems.* 2014;42(14): 1598-1610. DOI: 10.1080/15325008.2014.927029
- [10] Ben Salem F, Derbel N. Performance analysis of DTC-SVM sliding mode controllers-based parameters estimator of electric motor speed drive. *Mathematical Problems in Engineering.* 2014:1-11. DOI: 10.1155/2014/127128. Article ID 127128
- [11] Ben Salem F, Derbel N. Chapter 14: DTC-SVM based sliding mode controllers with load torque estimators for induction motor drives. In: *Applications of Sliding Mode Control, Studies in Systems, Decision and Control 79.* Singapore: Springer Science+Business Media; 2017. pp. 269-297. DOI: 10.1007/978-981-10-2374-3_14
- [12] Brandstetter P, Chlebis P, Palacky P. Direct torque control of induction motor with direct calculation of voltage vector. *Advances in Electrical and Computer Engineering Journal.* 2010; 10(4):17-22. DOI: 10.4316/aece.2010.04003
- [13] Carmelia S, Maurib M. Direct torque control as variable structure control: Existence conditions verification and analysis. *Electric Power Systems Research.* 2011;81:1188-1196. DOI: 10.1016/j.epsr.2011.01.007

- [14] Kuo-Kai S, Juu-Kuh L, Van-Truong P, Ming-Ji Y, Te-Wei W. Global minimum torque ripple design for direct torque control of induction motor drives. *IEEE Transactions on Industrial Electronics*. 2010;**57**(9):3148-3156. DOI: 10.1109/TIE.2009.2038401
- [15] Nash JN. Direct torque control, induction motor vector control without an encoder. *IEEE Transactions on Industry Applications*. 1997;**33**(2): 333-341. DOI: 10.1109/28.567792
- [16] Tiitinen P, Pohkalainen P, Lalu J. The next generation motor control method: Direct torque control (DTC). *European Power Electronics and Drives*. 1995;**5**(1):14-18. DOI: 10.1080/09398368.1995.11463357
- [17] Kazmierkowski MP, Kasprowicz A. Improved direct torque and flux vector control of PWM inverter-fed induction motor drives. *IEEE Transactions on Industrial Electronics*. 1995;**45**(4): 344-350. DOI: 10.1109/41.402472
- [18] Buja GS, Kazmierkowski MP. Direct torque control of PWM inverter-fed AC motors—A survey. *IEEE Transactions on Industrial Electronics*. 2004;**51**(4): 744-757. DOI: 10.1109/TIE.2004.831717
- [19] Yuttana K, Suttichai P, Hamid AT. Modified direct torque control method for induction motor drives based on amplitude and angle control of stator flux. *Journal of Electric Power Systems Research*. 2008;**78**(10):1712-1718. DOI: 10.1016/j.epsr.2008.02.015
- [20] Yang M, Tang S, Xu D. Comments on Antiwindup strategy for PI-type speed controller. *IEEE Transactions on Industrial Electronics*. 2015;**62**(2): 1329-1332. DOI: 10.1109/TIE.2014.2363626
- [21] Jose L, Azcue P, Ernesto R. Three-phase induction motor DTC-SVM scheme with self-tuning PI-type fuzzy controller. In: *International Conference on FSKD*. 2010. DOI: 10.1109/FSKD.2010.5569358
- [22] Lascu C, Trzynadlowski AM. Combining the principles of sliding mode, direct torque control, and space-vector modulation in a high-performance sensorless AC drive. *IEEE Transactions on Industry Applications*. 2004;**40**(1):170-177. DOI: 10.1109/TIA.2003.821667
- [23] Kyo-Beum L, Blaabjerg F. An improved DTC-SVM method for sensorless matrix converter drives using an over modulation strategy and a simple nonlinearity compensation. *IEEE Transactions on Industrial Electronics*. 2007;**54**(6):3155-3166. DOI: 10.1109/TIE.2007.905914
- [24] Bounadja M, Belarbi A, Belmadani B. A high-performance space vector modulation—Direct torque controlled induction machine drive based on stator flux orientation technique. *Advances in Electrical and Computer Engineering*. 2009;**9**(2): 28-33. DOI: 10.4316/aece.2009.02005
- [25] Bo L, Gui-Fang G, Xiao-Hong H, Xiao-Ning L. Novel torque ripple minimization algorithm for direct torque control of induction motor drive. *Journal of Shanghai University*. 2009; **13**(2):155-163. DOI: 10.1007/s11741-009-0213-3
- [26] Rashag HF, Koh SP, Chong KH, Tiong SK, Tan NML, Abdalla AN. High performance of space vector modulation direct torque control SVM-DTC based on amplitude voltage and stator flux angle. *Research Journal of Applied Sciences, Engineering and Technology*. 2013;**5**(15):3934-3940. DOI: 10.19026/rjaset.5.4455
- [27] Subodh KB, Kiran KJ. Five-phase induction motor DTC-SVM scheme with PI controller and ANN controller. *Procedia Technology*. 2016:816-823. DOI: 10.1016/j.protcy.2016.08.184

[28] Gadoue SM, Giaouris D, Finch JW. Artificial intelligence-based speed control of DTC induction motor drives—A comparative study. *Electric Power Systems Research*. 2009;210-219. DOI: 10.1016/j.epsr.2008.05.024

[29] El Ouanjli N, Derouich A, El Ghzizal A, Motahhir S, Chebabhi A, El Mourabit Y, et al. Modern improvement techniques of direct torque control for induction motor drives—A review. *Protection and Control of Modern Power Systems*. 2019;1-12. DOI: 10.1186/s41601-019-0125-5

[30] Uddin M, Hafeez M. FLC-based DTC scheme to improve the dynamic performance of an IM drive. *IEEE Transactions on Industry Applications*. 2012;48(2):823-831. DOI: 10.1109/TIA.2011.2181287

[31] Ouledali O, Meroufel A, Wira P, Bentouba S. Direct torque fuzzy control of PMSM based on SVM. *Energy Procedia*. 2015;1314-1322. DOI: 10.1016/j.egypro.2015.07.778

[32] Nour MO, Tedjini HA. Improved fuzzy logic control strategy of induction machine based on direct torque control. *International Journal of Mechatronics, Electrical and Computer Technology (IJMEC)*. DOI: 649123/10.225134

[33] Bousserhane IK, Hazzab A, Rahli M, Kamli M, Mazari B. Adaptive PI controller using fuzzy system optimized by genetic algorithm for induction motor control. *IEEE*. 2006;1-8. DOI: 10.1109/CIEP.2006.312162

[34] Laroussi K, Zelmat M. Implementation of a fuzzy logic system to tune a PI controller applied to induction motor. *Advances in Electrical and Computer Engineering*. 2009;9(3): 107-113. DOI: 10.4316/aece.2009.03019

DTC-SVM Approaches of an Induction Motor Dedicated to Position Control Applications

Fatma Ben Salem

Abstract

The chapter is devoted to the DTC and DTC-SVM position control approaches of induction motor (IM) allowing the movement of a photovoltaic panel according to the maximum sunshine position to extract a high efficiency of the system. The DTC is selected to full the application requirements, especially a maximum torque at standstill. This feature is necessary in order to guarantee a high degree of robustness of the maximum sunshine position tracking system against the high and sudden load torque variations characterized by the gusts of wind. The first step is devoted to a comparison study between three DTC strategies, dedicated to position control, such that: the basic DTC strategy, the DTC strategy with a look-up table including only active voltage vectors, and the DTC-SVM strategy with hysteresis controllers. Furthermore, the synthesis and the implementation of DTC-SVM approaches based on position control are treated. Within this context, the final part of the chapter proposes a comparison between three DTC-SVM approaches: (i) a DTC-SVM approach using PI controllers, (ii) a DTC-SVM approach using PI controllers with a nonlinear compensator, and (iii) a DTC-SVM approach using sliding mode controllers. In that case, an adaptation approach of parameter estimators are implemented in order to eliminate the effects of parameter variations and load disturbances. Simulations results show that the SM DTC-SVM approach gives the best results.

Keywords: induction machine, position control, SM, DTC, SVM, parameters variations, load disturbances

1. Introduction

Induction motors (IM) are very common because they are inexpensive and robust, finding use in everything from industrial applications such as pumps, fans, and blowers to home appliances. In recent years, the control of high-performance IM drives for general industrial applications and production areas has received a lot of research interests.

The most modern technique, for the induction machine, is the direct torque and the stator flux vector control method (DTC). It has been realized in an industrial way by ABB, using the theoretical background proposed by *Takahashi* [1] and *Depenbrock* [2] in the middle of 1980's. Over the years, DTC method becomes one of the high-performance control strategies for AC machines to provide a very fast torque and flux control [3, 4].

The DTC has been selected in order to fulfill the application requirements, especially a maximum torque at standstill. This feature is necessary in order to guarantee a high degree of robustness of the maximum sunshine position tracking system against the high and sudden load torque variations characterized by the gusts of wind. This positioning system can be introduced in the multi-sources hybrid system, in order to allow high efficiencies of photovoltaic systems. To do so, an electric motor drive could be associated with photovoltaic panels in order to be able to track the maximum sunshine positions during the day. In what follows, the chapter will be focused on the problem of position regulation of an induction motor under DTC and DTC-SVM strategies.

2. A case study: solar panel positioning

2.1 Problem heading

Photovoltaic panels are commonly exposed to the sun in a fixed position corresponding to the maximum sunshine recorded during a day that is the position of the sun at midday. Nevertheless, this strategy does not allow the extraction of the maximum power during a day and therefore a high efficiency of photovoltaic systems, which can be integrated with the multi-source hybrid system, described above. An approach to solve this problem consists in moving photovoltaic panels according to the maximum sunshine position. To do so, an electric motor drive could be associated with photovoltaic panels in order to be able to track the maximum sunshine positions during the day. Accounting for the high perturbation amplitude applied to the panel, the control strategy to be implemented in the drive is of great importance [5].

The proposed tracking system has two freedom degrees in such a way that it allows the displacement of the photovoltaic system within latitudes and meridians: the first degree of freedom is controlled automatically by an IM drive under the control of a DTC strategy.

The DTC approach has been selected in order to full the application requirements, especially a maximum torque at standstill. This feature is necessary in order to guarantee a high degree of robustness of the maximum sunshine position tracking system against the high and sudden load torque variations characterized by the gusts of wind.

The following work will be focused on the study of the first freedom degree. Special attention is paid to the implementation of a suitable DTC strategy in the IM drive.

2.2 Mathematical model of induction machines

The dynamic behavior of an induction machine is defined in terms of space variables in the sequel:

$$\begin{cases} \frac{d}{dt}\phi_{as} = v_{as} - R_s i_{as} \\ \frac{d}{dt}\phi_{\beta s} = v_{\beta s} - R_s i_{\beta s} \\ \frac{d}{dt}\phi_{ar} = -R_r i_{ar} - \omega_m \phi_{\beta r} \\ \frac{d}{dt}\phi_{\beta r} = -R_r i_{\beta r} + \omega_m \phi_{ar} \end{cases} \quad (1)$$

considering that subscripts s and r refer to stator and rotor, subscripts α and β refer to components in (α, β) frame, v, i and ρ refer to voltage, current and flux, R_s and R_r refer to stator and rotor resistances, and ω_m refers to the machine speed ($\omega_m = N_p \Omega_m = \omega_s - \omega_r$ and N_p is the pole pair number).

Relationships between currents and flux are:

$$\begin{cases} \phi_{\alpha s} = L_s i_{\alpha s} + M i_{\alpha r} \\ \phi_{\alpha r} = M i_{\alpha s} + L_r i_{\alpha r} \\ \phi_{\beta r} = M i_{\beta s} + L_r i_{\beta r} \\ \phi_{\beta s} = L_s i_{\beta s} + M i_{\beta r} \end{cases} \quad (2)$$

where L and M refer to the inductance and the mutual one.
 The mechanical part of the machine is described by:

$$J \frac{d}{dt} \Omega_m = T_{em} - T_l \quad (3)$$

where J is the motor inertia and T_l represent the load torque.

2.3 Voltage source inverter

The made constant DC voltage by the rectifier is delivered to the inverter input, which thanks to controlled transistor switches, converts this voltage to three-phase AC voltage signal with wide range variable voltage amplitude and frequency.

The voltage vector of the three-phase voltage inverter can be represented as follows:

$$\vec{V}_s = \sqrt{\frac{2}{3}} [S_a + S_b e^{j\frac{2\pi}{3}} + S_c e^{j\frac{4\pi}{3}}] \quad (4)$$

where S_a, S_b and S_c are three-phase inverter switching functions, which can take a logical value of either 0 or 1.

2.4 Basic concept of DTC based position control

The implementation scheme of the *Takahashi* basic DTC strategy applied to the position regulation of an induction motor drive is shown in **Figure 1**.

Referring to [5, 6], it has been found that the *Takahashi* basic DTC strategy is penalized at low speeds by the so-called “demagnetization phenomenon” which is caused by the systematic application of zero voltage vectors when the torque regulator output is zero, independently of the flux regulator output state. Indeed, the application of these voltage vectors during a sampling period T_s yields a slight decrease of the stator flux at high speeds. However, at low speeds, the application of zero voltage vectors leads to a high reduction of the stator flux, yielding the demagnetization problem which affects the electromagnetic torque.

In order to overcome this shortcoming, the zero-voltage vectors can be substituted by active ones. For a given stator flux vector and when the torque regulator output is “0”, the active vector around which is located the sector including the stator flux vector, is applied. The resulting look-up table is given in **Table 1**. Nevertheless, this substitution is associated to an other crucial problem: that is an increase of the inverter switching frequency which compromises the drive efficiency.

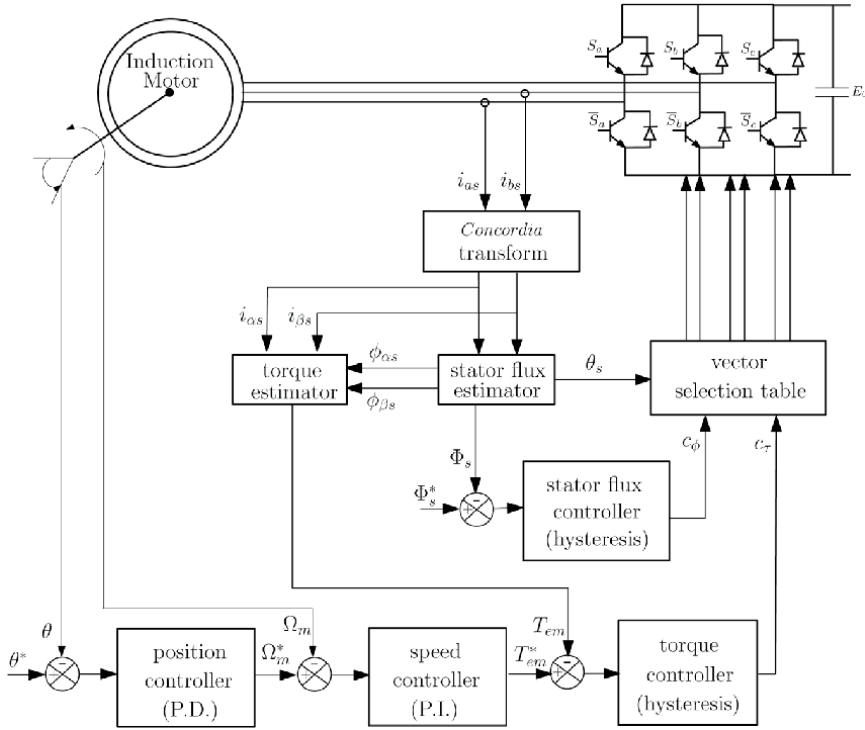


Figure 1. IM position regulation based on basic DTC strategy.

c_ϕ	+1			-1		
c_τ	+1	0	-1	+1	0	-1
S1	V_2 (100)	V_1 (101)	V_6 (001)	V_3 (110)	V_4 (010)	V_5 (011)
S2	V_3 (110)	V_2 (100)	V_1 (101)	V_4 (010)	V_5 (011)	V_6 (001)
S4	V_4 (010)	V_3 (110)	V_2 (100)	V_5 (011)	V_6 (001)	V_1 (101)
S4	V_5 (011)	V_4 (010)	V_3 (110)	V_6 (001)	V_1 (101)	V_2 (100)
S5	V_6 (001)	V_5 (011)	V_4 (010)	V_1 (101)	V_2 (100)	V_3 (110)
S6	V_1 (101)	V_6 (001)	V_5 (011)	V_2 (100)	V_3 (110)	V_4 (010)

Table 1. Look-up table with zero-voltage vectors substituted by active ones.

2.5 Concept of DTC-SVM with hysteresis controllers based position control

The implementation scheme of the DTC-SVM strategy with hysteresis controllers applied to the position regulation of an induction motor drive is shown in **Figure 2**. It has the same layout as the one of the basic DTC strategy proposed in section II, except that the SVM bloc is added to the control system that ensures an imposed switching frequency [7–12].

2.6 Simulations and discussions: A comparative study

The ratings and parameters of the induction machine, used in the simulation study, are listed in **Tables 2** and **3** respectively.

- The sampling period T_s has been chosen equal to $50\mu s$ in the cases of the first and the second strategies, whereas in the case of the third strategy, it has been chosen equal to $100\mu s$.
- Bandwidths of flux and torque hysteresis regulators have been chosen as: $\varepsilon_\phi = 0.02\text{ Wb}$ and $\varepsilon_\tau = 5\text{ N}$ for the two first strategies, whereas for the third one, they have been selected as $\varepsilon_\phi = 0.02\text{ Wb}$ and $\varepsilon_\tau = 3.5\text{ N}$.
- The load torque is given by the following expression: $T_l = K \sin \theta$. K has been calculated and has been found equal to 57.762 N.m .
- The modulation period has been fixed to $T_{mod} = 150\mu s$ in DTC-SVM approach under study.

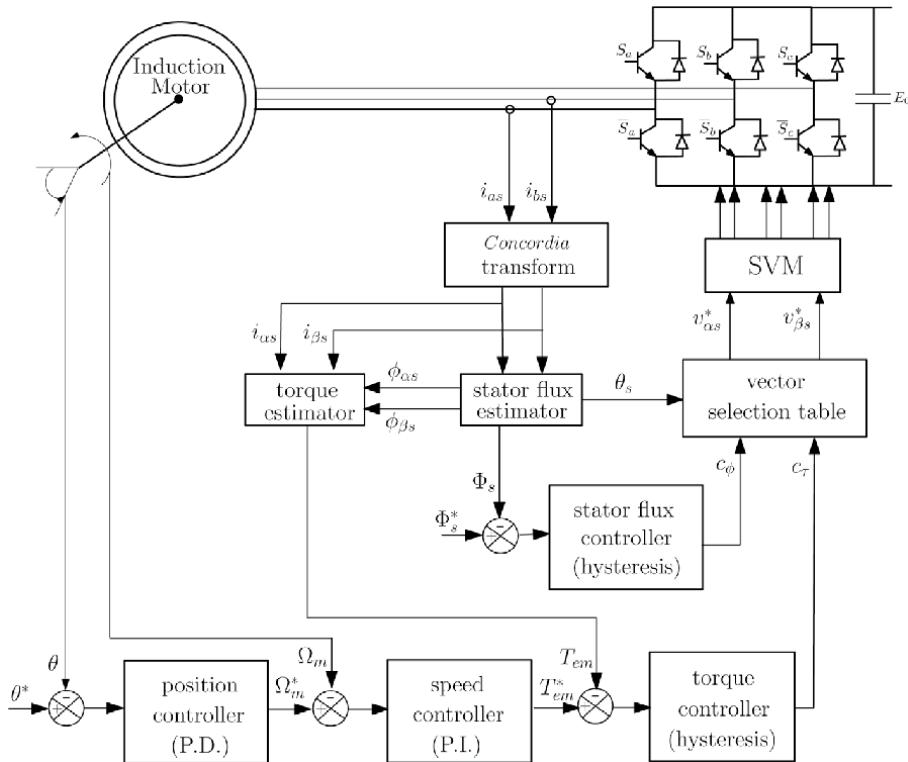


Figure 2.
 Induction motor position regulation based on the DTC-SVM strategy.

Power	10 kW	Voltage	380 V/220 V
Efficiency	80%	Current	24A/41A
Speed	1500 rpm	Frequency	50 Hz

Table 2.
 Induction machine ratings.

$r_s = 0.29\Omega$	$r_r = 0.38\Omega$	$M = 47.3\text{mH}$
$L_s = L_r = 50\text{mH}$	$N_p = 2$	$J = 0.5\text{Kg.m}^2$

Table 3.
Induction machine parameters.

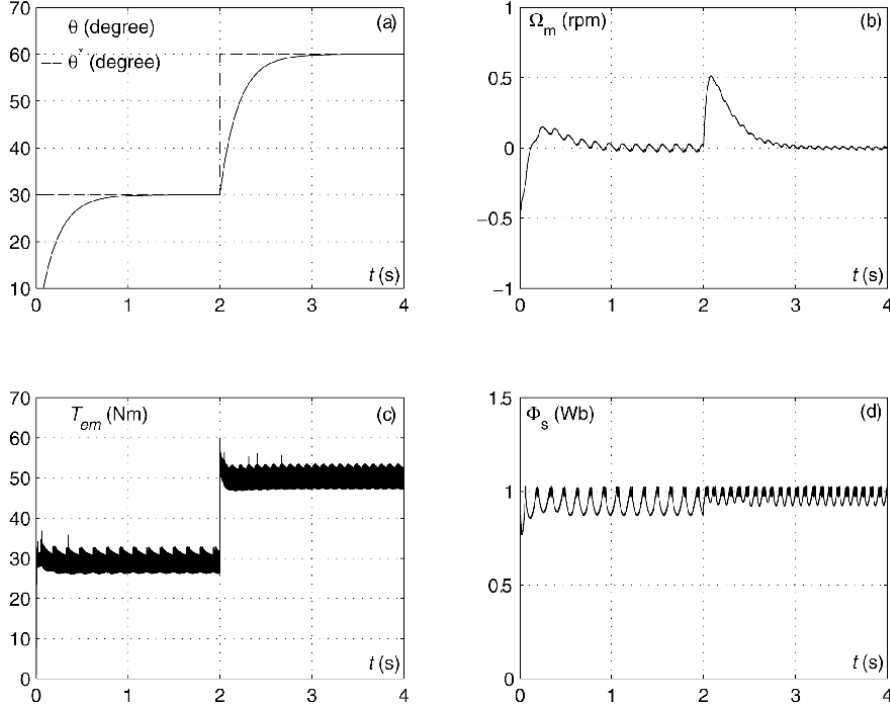


Figure 3. Induction motor position regulation under the basic Takahashi DTC strategy, (a): Rotor position θ and its reference, (b): Speed Ω_m , (c): Electromagnetic torque T_{em} , (d): Stator flux Φ_s .

Figures 3–5 show the induction motor dynamic following the application of a dual-step reference position under the basic *Takahashi* DTC strategy, the modified *Takahashi* one, and the DTC-SVM strategy with a controlled commutation frequency, respectively. In order to highlight performances gained by the DTC-SVM scheme, resulting features are compared to the obtained ones following the implementation of the basic DTC strategy. The analysis of these results leads to the following remarks:

- **Figures 3a–5a** show that the three DTC strategies exhibit almost the same position and speed dynamics,
- Performances of the flux loop of the basic *Takahashi* DTC strategy is affected by the demagnetized phenomenon (**Figure 3d**). In fact, the analysis of the *Takahashi* strategy highlights low performances at low speed operations. Under such conditions, and for steady state operations, the motor turns to be demagnetized.
- In order to overcome the demagnetization problem caused by zero-voltage vectors included in the look-up table of the basic DTC strategy, these have

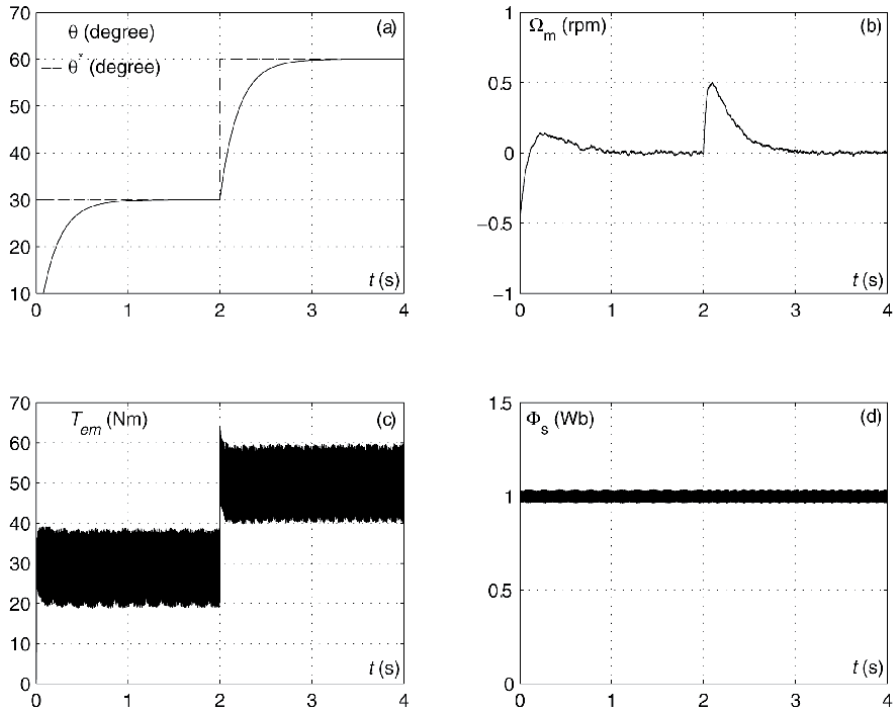


Figure 4. Induction motor position regulation under the modified Takahashi DTC strategy, (a): Rotor position θ and its reference, (b): Speed Ω_m , (c): Electromagnetic torque T_{em} , (d): Stator flux Φ_s .

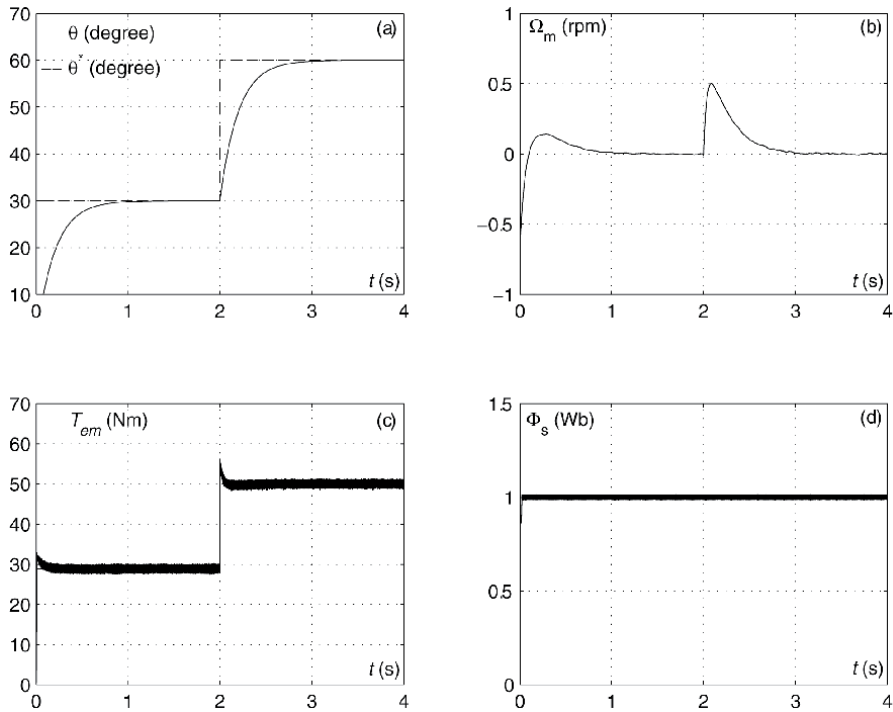


Figure 5. Induction motor position regulation under the DTC-SVM strategy with a constant commutation frequency of 6.5 kHz, (a) rotor position θ , (b): Speed Ω_m , (c): Electromagnetic torque T_{em} , (d): Stator flux Φ_s .

been substituted by active vectors. Obtained results are illustrated in **Figure 4**. Referring to **Figure 4d**, one can notice that the demagnetization problem has been removed, while performances of the motor, for high speeds, are not affected. However, the torque ripple amplitudes rise considerably (**Figure 4c**) with respect to the one yielded by the *Takahashi* DTC strategy, which represents a severe drawback.

- **Figure 5** shows that the DTC-SVM strategy exhibits high dynamical performances. In fact, this approach presents a low torque ripple amplitude (**Figure 5c**). Moreover, it completely eliminates the demagnetization phenomenon (**Figure 5d**).

Further investigation of the stator flux has been achieved through the representation of the stator flux vector extremity locus in the (α, β) plane. This has been

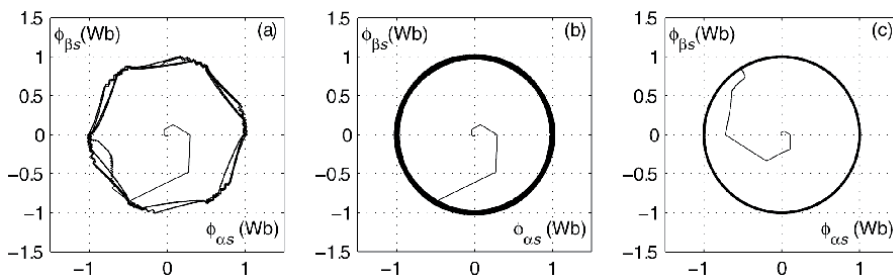


Figure 6. Locus of the extremities of $\vec{\Phi}_s$, with (a) basic *Takahashi* DTC strategy, (b) modified *Takahashi* DTC strategy and (c) DTC-SVM strategy with a constant commutation frequency.

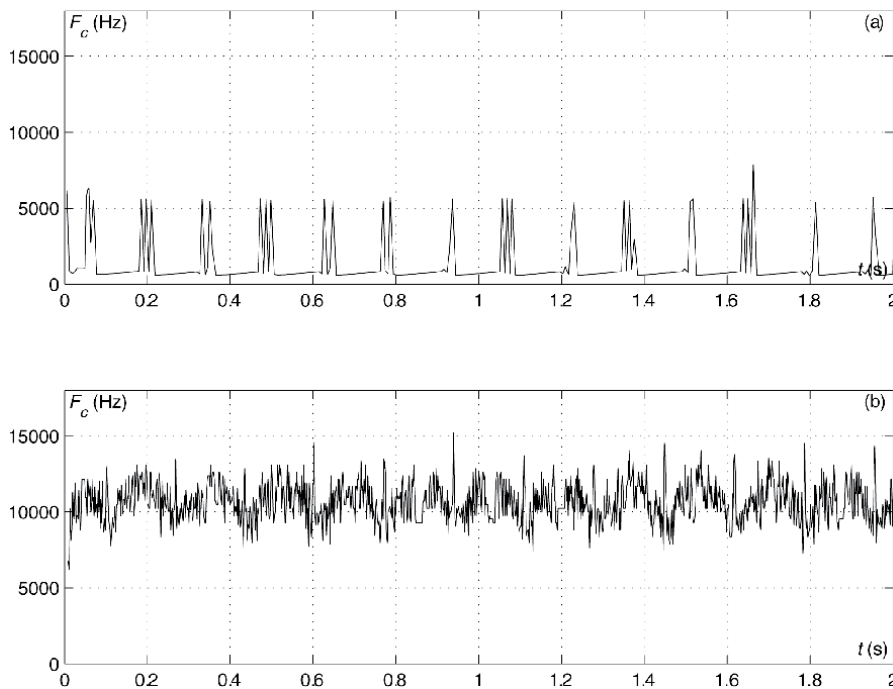


Figure 7. Average commutation frequency of the inverter power switches, (a) basic *Takahashi* DTC strategy, (b) modified *Takahashi* DTC strategy.

done considering the three DTC strategies. Obtained results are shown in **Figure 6**. One can notice, easily, that the DTC-SVM strategy with hysteresis regulators and with an imposed commutation frequency yields to the smoothest circular locus.

Finally, we have involved in the assessment of the average commutation frequencies of both basic and modified *Takahashi* DTC strategies. Obtained results have been showing in **Figure 7**. It is to be noted that the basic DTC strategy and the DTC-SVM with an imposed commutation frequency ($F_c = 6.25kHz$) strategy offer lower commutation frequencies than the modified *Takahashi* DTC strategy.

3. Concept of PI DTC-SVM based position control

3.1 Computing of flux reference coordinates

The slip angular reference speed ω_r^* , which is the output of the PI controller, will be used to calculate the argument of the stator flux reference. In the reference frame (α , β), coordinates of the reference stator flux $\phi_{\alpha s}^*$ and $\phi_{\beta s}^*$ are calculated from the polar coordinates according to the following expressions:

$$\begin{cases} \phi_{\alpha s}^* = |\Phi_s^*| \cos \theta_s^* \\ \phi_{\beta s}^* = |\Phi_s^*| \sin \theta_s^* \end{cases} \quad (5)$$

3.2 Computing of voltage reference coordinates

The coordinates of references of voltage vectors $v_{\alpha s}^*$ and $v_{\beta s}^*$ in (α , β) frame are determined by the following equations:

$$\begin{cases} V_{\alpha s}^* = \frac{\phi_{\alpha s}^* - \phi_{\alpha s}}{T_e} + R_s i_{\alpha s} \\ V_{\beta s}^* = \frac{\phi_{\beta s}^* - \phi_{\beta s}}{T_e} + R_s i_{\beta s} \end{cases} \quad (6)$$

Finally, they are introduced to the SVM block, which uses them to control the inverter switches (S_a , S_b , S_c).

3.3 Position control loop

The objective is the design of a suitable controller as described by **Figure 8**.

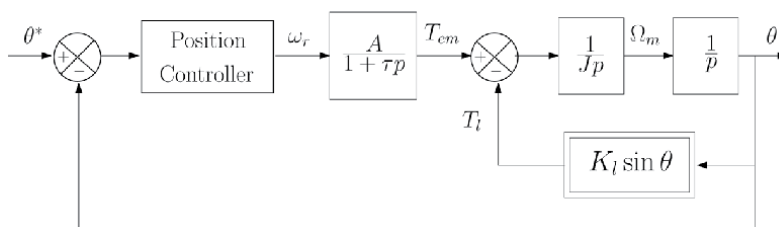


Figure 8.
 Position control loop.

Then, we have:

$$\begin{cases} \frac{d\theta}{dt} = \Omega_m \\ \frac{d^2\theta}{dt^2} = \frac{1}{J}T_{em} - \frac{K_l}{J} \sin \theta \\ \frac{d^3\theta}{dt^3} = \frac{1}{J} \frac{dT_{em}}{dt} - \frac{K_l}{J} \frac{d\theta}{dt} \cos \theta \end{cases} \quad (7)$$

This yields:

$$\begin{aligned} \frac{d^3\theta}{dt^3} &= \frac{1}{J} \left(-\frac{1}{\tau}T_{em} + \frac{A}{\tau} \omega_r \right) - \frac{K_l}{J} \frac{d\theta}{dt} \cos \theta \\ &= -\frac{1}{\tau} \left(\frac{d^2\theta}{dt^2} + \frac{K_l}{J} \sin \theta \right) + \frac{A}{J\tau} \omega_r - \frac{K_l}{J} \frac{d\theta}{dt} \cos \theta \end{aligned} \quad (8)$$

Thus, we can write:

$$\frac{d^3\theta}{dt^3} + \frac{1}{\tau} \frac{d^2\theta}{dt^2} + \frac{K_l}{J} \frac{d\theta}{dt} + \frac{K_l}{J\tau} \theta + \varphi \left(\theta, \frac{d\theta}{dt} \right) = \frac{A}{J\tau} \omega_r \quad (9)$$

where:

$$\varphi \left(\theta, \frac{d\theta}{dt} \right) = \frac{K_l}{J} \frac{d\theta}{dt} (\cos \theta - 1) + \frac{K_l}{J\tau} (\sin \theta - \theta) = 0 \left(\theta, \frac{d\theta}{dt} \right)^3 \quad (10)$$

For small values of θ , $\varphi \left(\theta, \frac{d\theta}{dt} \right)$ can be neglected, and then the mechanical part of the machine can be represented by a third order linear system described by the following transfer function:

$$\frac{\theta}{\omega_r} = \frac{\frac{A}{J\tau}}{\left(p^2 + \frac{K_l}{J} \right) \left(p + \frac{1}{\tau} \right)} \quad (11)$$

It is to be noted that the application of the following nonlinear feedback represents a nonlinear compensator:

$$\omega_r' = \omega_r - \frac{J\tau}{K_l} \varphi \left(\theta, \frac{d\theta}{dt} \right) \quad (12)$$

This loop realizes a feedback linearization. The transfer function between θ and ω_r' is expressed as:

$$\frac{\theta}{\omega_r'} = \frac{\frac{A}{J\tau}}{\left(p^2 + \frac{K_l}{J} \right) \left(p + \frac{1}{\tau} \right)} \quad (13)$$

which is an exact transfer function without any approximation.

Observing this transfer function, it is clear that it contains two imaginary poles. This leads to a certain difficulty to control the system with a PID controller $C(p)$:

$$C(p) = K_c \left(1 + \frac{1}{T_i p} + T_d p \right) \quad (14)$$

In fact, the system does not present any stability margin. Moreover, to have an adequate dynamical behavior, the derivative time constant (T_d) should be larger than the integral time constant (T_i), which is strongly not recommended.

3.4 DTC-SVM based position control scheme

The implementation scheme of a DTC-SVM based position regulation of an induction motor is shown in **Figure 9**. The idea is based on the decoupling between the amplitude and the argument of the stator flux reference vector.

The amplitude of this vector will be imposed equal to the nominal value of the stator flux, but the argument will be calculated according to the desired performances. In fact, the error between the reference position θ^* and the measured one θ is applied to the position regulator whose output provides the slip angular reference speed ω_r^* , which will be used to calculate the argument of the stator flux reference. Coordinates of the reference stator flux in the reference frame (α, β) are computed from its polar coordinates according to Eqs. (5). The coordinates of the reference voltage vector $v_{\alpha s}^*$ and $v_{\beta s}^*$ are determined using Eqs. (6).

Finally, the SVM block, which uses these later to generate the convenient stator voltages inverter in each modulation period, ensuring working with a constant commutation frequency.

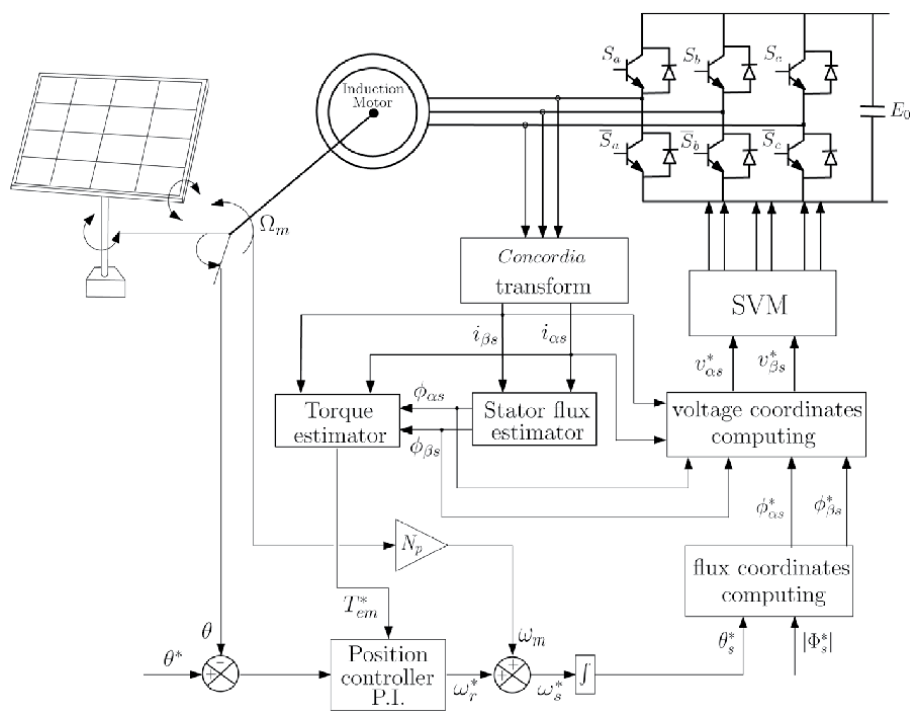


Figure 9. Induction motor position regulation based on the DTC-SVM strategy.

3.5 Concept of sliding mode DTC-SVM based position control

Sliding mode (SM) controllers perform well in non nonlinear systems than PI controllers [13, 14]. Indeed, the sliding mode control is a type of variable structure systems characterized by the high simplicity and the robustness against insensitivity to parameter variations and external disturbances [14–16]. Considering a nonlinear system described by the following state equation:

$$\dot{X} = f(X) + g(X)U \quad (15)$$

A choice of the sliding surface $S(X)$ can be given by:

$$S(X) = h(X) - h(X^*) \quad (16)$$

with X^* is a reference trajectory.

In order to decide a system trajectory, the equivalent control U_{eq} represents the required control to reach and to remain on the sliding surface. The corrected term ΔU is required to guarantee the remaining on the surface $S(X) = 0$.

Thus, one can choose for the controller the following expression:

$$U = U_{eq} + \Delta U \quad (17)$$

The equivalent control can be designed as follows: when the system remains on the sliding surface, we have $S(X) = 0$, then $\dot{S}(X) = 0$. Since:

$$\dot{S}(X) = h_1(X)[f(X) + g(X)U] - h_1(X^*)\dot{X}^* = \mathcal{F}(X, X^*) + \mathcal{G}(X)U \quad (18)$$

where $h_1(X) = \frac{dh}{dX}$.

This yields the following expression of the equivalent control:

$$U_{eq} = [h_1(X)g(X)]^{-1} [h_1(X^*)\dot{X}^* - h_1(X)f(X)] = -[\mathcal{G}(X)]^{-1}\mathcal{F}(X, X^*) \quad (19)$$

under the regularity of matrix $\mathcal{G}(X) = [h_1(X)g(X)]$.

The term ΔU can be expressed as:

$$\Delta U = -U_0 \text{sign} \left[\mathcal{G}^T(X)S(X) \right] \quad (20)$$

In fact, if we consider the Lyapunov function:

$$V(X) = S^T S > 0 \quad (21)$$

Its differential with respect to time is expressed as:

$$\dot{V} = S^T \dot{S} = S^T \mathcal{G}(X)\Delta U = -U_0 S^T \mathcal{G}(X) \text{sign} \left[\mathcal{G}^T(X)S(X) \right] = -U_0 \|\mathcal{G}^T(X)S(X)\|_1 \leq 0 \quad (22)$$

This yields that the closed loop system is stable.

3.5.1 Position sliding mode controller

The sliding surface is expressed as:

$$S_\theta = \left(\frac{d}{dt} + \lambda_1 \right)^2 \varepsilon_\theta = 0 \quad (23)$$

that is to say:

$$S_\theta = \frac{d^2 \varepsilon_\theta}{dt^2} + 2\lambda_1 \frac{d\varepsilon_\theta}{dt} + \lambda_1^2 \varepsilon_\theta = 0 \quad (24)$$

with: $\varepsilon_\theta = \theta - \theta^*$. This choice takes into account that the error decreases exponentially after reaching the sliding surface. In fact, if $S_\theta = 0$, for $t \geq t_0$, we have:
 $\varepsilon_\theta(t) = \{\varepsilon_\theta(t_0) + [\dot{\varepsilon}_\theta(t_0) + \lambda_1 \varepsilon_\theta(t_0)](t - t_0)\} e^{-\lambda_1(t-t_0)}$.

In this case, function $h(X)$ is expressed as:

$$h(X) = \frac{1}{J} T_{em} + 2\lambda_1 \Omega_m + \lambda_1^2 \theta - \frac{K_l}{J} \sin \theta \quad (25)$$

To remain the state of the system on the sliding surface $S_\theta = 0$, we have: $\dot{S}_\theta = 0$. This leads to:

$$\dot{S}_\theta = \frac{d^3 \varepsilon_\theta}{dt^3} + 2\lambda_1 \frac{d^2 \varepsilon_\theta}{dt^2} + \lambda_1^2 \frac{d\varepsilon_\theta}{dt} = 0 \quad (26)$$

That is to say:

$$\begin{aligned} \dot{S}_\theta &= \frac{1}{J} \left(-\frac{1}{\tau} T_{em} + \frac{A}{\tau} U \right) + 2\lambda_1 \left(\frac{1}{J} T_{em} - \frac{K_l}{J} \sin \theta \right) + \left(\lambda_1^2 - \frac{K_l}{J} \cos \theta \right) \Omega_m - h_1(X^*) \dot{X}^* \\ &= 0 \end{aligned} \quad (27)$$

where:

$$h_1(X^*) \dot{X}^* = \left(\ddot{\Omega}_m^* + 2\lambda_1 \dot{\Omega}_m^* + \lambda_1^2 \dot{\theta}^* \right) \quad (28)$$

Then, it is easy to express the so-called equivalent control which corresponds to the required control remaining the system on the sliding surface:

$$U_{eq,\theta} = \frac{1}{A} T_{em} - 2 \frac{\lambda_1 \tau}{A} (T_{em} - K_l \sin \theta) - \frac{J \tau}{A} \lambda_1^2 \Omega_m + \frac{\tau K_l}{A} \Omega_m \cos \theta + \frac{J \tau}{A} h_1(X^*) \dot{X}^* \quad (29)$$

Then, the slip angular reference speed ω_r can be expressed by:

$$\omega_r = U_{eq,\theta} - U_{0,\theta} \text{sign}(S_\theta) \quad (30)$$

The new structure of this control approach is given by the block diagram of **Figure 10**.

3.6 SM controllers with adaptive parameters estimation

If system (14) depends on an unknown parameter vector $\gamma = [\gamma_1 \gamma_2 \dots]^T$, the expression of the control depends on γ , that is to say: $U_{eq} = U_{eq}(\gamma)$ and the applied control law becomes:

$$\bar{U} = \bar{U}_{eq} + \Delta U \quad (31)$$

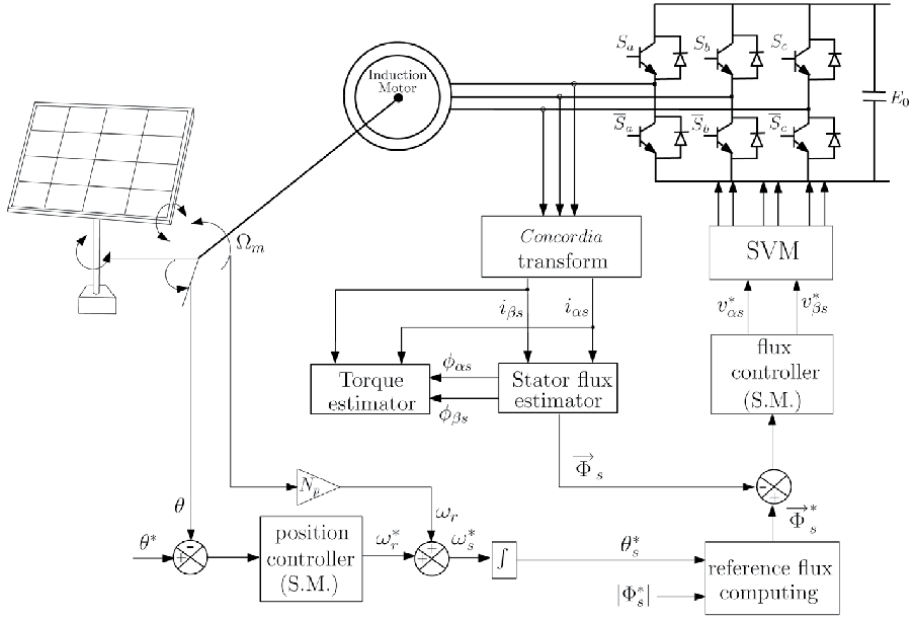


Figure 10. Induction motor position regulation based on the DTC-SVM with sliding mode controllers.

where $\bar{U}_{eq} = U_{eq}(\bar{\gamma})$. $\bar{\gamma}$ is the estimated vector of γ .

Referring to Eq. (17), the differential of S is expressed as:

$$\begin{aligned}
 \dot{S} &= \mathcal{F}(X, X^*) + \mathcal{G}(X)\bar{U} = \mathcal{F}(X, X^*) + \mathcal{G}(X)(\bar{U}_{eq} + \Delta U) \\
 &= \underbrace{\mathcal{F}(X, X^*) + \mathcal{G}(X)U_{eq}}_{=0} + \mathcal{G}(X)\Delta U + \mathcal{G}(X)(\bar{U}_{eq} - U_{eq}) \\
 &= \mathcal{G}(X)\Delta U + \mathcal{G}(X)(\bar{U}_{eq} - U_{eq}) \\
 &= \mathcal{G}(X)\Delta U + \mathcal{G}(X)(\bar{U}_{eq} - U_{eq}) + \underbrace{\left[\underbrace{\mathcal{G}(X) - \bar{\mathcal{G}}(X)}_{=o(\Delta\gamma)} \right] \underbrace{(\bar{U}_{eq} - U_{eq})}_{=o(\Delta\gamma)}}_{=o(\Delta\gamma)^2} \\
 &= \mathcal{G}(X)\Delta U + \bar{\mathcal{G}}(X) \left(\sum_i \frac{\partial U_{eq}}{\partial \gamma_i}(\bar{\gamma}) \Delta \gamma_i \right) + o(\Delta\gamma)^2 \\
 &= \bar{\mathcal{G}}(X)\Delta U + \bar{\mathcal{G}}(X) \left(\sum_i \frac{\partial U_{eq}}{\partial \gamma_i}(\bar{\gamma}) \Delta \gamma_i \right) + [\mathcal{G}(X) - \bar{\mathcal{G}}(X)]\Delta U + o(\Delta\gamma)^2 \\
 &= \bar{\mathcal{G}}(X)\Delta U + \bar{\mathcal{G}}(X) \left(\sum_i \frac{\partial U_{eq}}{\partial \gamma_i}(\bar{\gamma}) \Delta \gamma_i \right) + [\mathcal{G}(X) - \bar{\mathcal{G}}(X)]\Delta U + o(\Delta\gamma)^2 \\
 &= \bar{\mathcal{G}}(X)\Delta U + \left(\sum_i \left[\bar{\mathcal{G}}(X) \frac{\partial U_{eq}}{\partial \gamma_i}(\bar{\gamma}) + \frac{\partial \mathcal{G}(X)}{\partial \gamma_i} \Delta U \right] \Delta \gamma_i \right) + o(\Delta\gamma)^2
 \end{aligned} \tag{32}$$

with $\Delta\gamma = \bar{\gamma} - \gamma$ and $\bar{\mathcal{G}}(X)$ is the expression of $\mathcal{G}(X)$ for $\gamma = \bar{\gamma}$.

- Theorem

Control laws (17), (19) and (20) stabilize system (15) with the following adaptive laws:

$$\dot{\bar{\gamma}}_i = -\eta_i S^T \left(\bar{G}(X) \frac{\partial U_{eq}}{\partial \gamma_i}(\bar{\gamma}) + \frac{\partial G(X)}{\partial \gamma_i} \Delta U \right) \quad (33)$$

- Proof

Let us consider the following Lyapunov function:

$$V = \frac{1}{2} S^T S + \frac{1}{2} \sum_i \frac{1}{\eta_i} \Delta \gamma_i^2 \quad (34)$$

In the following, it assumed that vector γ is constant or it has slow variations with respect to time, in such way that we can neglect its differential with

respect to time: $\dot{\gamma} \simeq 0$. Then, we can write: $\Delta \dot{\gamma} \simeq \dot{\bar{\gamma}}$.

The differential with respect to time of function V is expressed as:

$$\begin{aligned} \dot{V} &= S^T \dot{S} + \sum_i \frac{1}{\eta_i} \Delta \gamma_i \Delta \dot{\gamma}_i \\ &= S^T \left[\bar{G}(X) \Delta U + \left(\sum_i \left[\bar{G}(X) \frac{\partial U_{eq}}{\partial \gamma_i}(\bar{\gamma}) + \frac{\partial G(X)}{\partial \gamma_i} \Delta U \right] \Delta \gamma_i \right) + o(\Delta \gamma)^2 \right] \\ &\quad + \sum_i \frac{1}{\eta_i} \Delta \gamma_i \Delta \dot{\gamma}_i + o(\Delta \gamma)^2 \\ &= S^T \bar{G}(X) \Delta U + \underbrace{\sum_i \left[S^T \left(\bar{G}(X) \frac{\partial U_{eq}}{\partial \gamma_i}(\bar{\gamma}) + \frac{\partial G(X)}{\partial \gamma_i} \Delta U \right) + \frac{1}{\eta_i} \Delta \dot{\gamma}_i \right] \Delta \gamma_i}_{=0} + o(\Delta \gamma)^2 \\ &= S^T \bar{G}(X) \Delta U + o(\Delta \gamma)^2 = -S^T \bar{G}(X) \text{sign} \left[\bar{G}^T(X) S(X) \right] + o(\Delta \gamma)^2 \\ &= -\left\| \bar{G}^T(X) S(X) \right\|_1 + o(\Delta \gamma)^2 \leq 0 \end{aligned} \quad (35)$$

where $\|\cdot\|_1$ is the norm “1” of a vector which corresponds to the sum of absolute values of its components.

3.6.1 Position adaptive SM controller with variations on the mutual inductance and the rotor resistance

The sensitivity of the DTC-SVM to (i) variations on the magnetic permeability of the stator and rotor cores, and (ii) variations on the rotor resistance, which can vary with time and operating conditions, can be removed by an online estimation of the mutual inductance and the rotor resistance. The adaptive SM of the speed can be derived based on the mutual inductance and rotor resistance estimations using the *Lyapunov* theorem [17].

It is easy to show that:

$$U_\theta = \bar{U}_{eq,\theta} - U_{0,\theta} \text{sign} (S_\Omega) \quad (36)$$

where:

$$\bar{U}_{eq,\theta} = -\left[\bar{G}(X)\right]^{-1}\bar{F}(X, X^*) \quad (37)$$

Then:

$$\begin{aligned} \dot{S}_\theta &= \mathcal{F}(X, X^*) + \mathcal{G}(X)\bar{U}_\theta = \mathcal{F}(X, X^*) + \mathcal{G}(X)(\bar{U}_{eq,\theta} + \Delta U_\theta) \\ &= \mathcal{F}(X, X^*) + \mathcal{G}(X)U_{eq,\theta} + \mathcal{G}(X)\Delta U_\theta + \mathcal{G}(X)(\bar{U}_{eq,\theta} - U_{eq,\theta}) \\ &= \mathcal{G}(X)\Delta U_\theta + \mathcal{G}(X)(\bar{U}_{eq,\theta} - U_{eq,\theta}) \end{aligned} \quad (38)$$

- Corollary

The following slip angular reference speed control law stabilizes the speed loop:

$$\omega_r = \bar{U}_{eq,\theta} - U_{0,\theta} \text{ sign } (S_\Omega) \quad (39)$$

where $\bar{U}_{eq,\theta} = U_{eq,\theta}(\bar{M}, \bar{R}_r)$, \bar{M} and \bar{R}_r are estimator values of the mutual inductance and the rotor resistance given by the following updating laws:

$$\begin{aligned} \dot{\bar{M}} &= -\eta_{\theta_1} \bar{G} S_\theta \left(\frac{\partial U_{eq,\theta}}{\partial M} \right) \\ \dot{\bar{R}}_r &= -\eta_{\theta_2} \bar{G} S_\theta \left(\frac{\partial U_{eq,\theta}}{\partial R} \right) \end{aligned} \quad (40)$$

with: η_{θ_1} and η_{θ_2} positive scalars, $\mathcal{G} = \mathcal{G}(M, R_r)$ and $\bar{G} = \bar{G}(\bar{M}, \bar{R}_r)$ defined in Eq. (17).

- Proof

Considering the following function:

$$V_\theta = \frac{1}{2} S_\theta^2 + \frac{1}{2\eta_{\theta_1}} \Delta M^2 + \frac{1}{2\eta_{\theta_2}} \Delta R_r^2 \quad (41)$$

with $\Delta M = \bar{M} - M$ and $\Delta R_r = \bar{R}_r - R_r$.

The time derivative of the *Lyapunov* function can be expressed as:

$$\dot{V}_\theta = S_\theta \dot{S}_\theta + \frac{1}{\eta_{\theta_1}} \Delta M \Delta \dot{M} + \frac{1}{\eta_{\theta_2}} \Delta R_r \Delta \dot{R}_r \quad (42)$$

However:

$$\bar{U}_{eq,\theta} - U_{eq,\theta} = (\bar{M} - M) \left(\frac{\partial U_{eq,\theta}}{\partial M} \right) + (\bar{R}_r - R_r) \left(\frac{\partial U_{eq,\theta}}{\partial R_r} \right) + o(\Delta M, \Delta R_r)^2 \quad (43)$$

Moreover:

$$\mathcal{G} (\bar{U}_{eq,\theta} - U_{eq,\theta}) = \bar{G} (\bar{U}_{eq,\theta} - U_{eq,\theta}) + o(\Delta M, \Delta R_r)^2 \quad (44)$$

Thereby, Eq. (42) gives:

$$\begin{aligned} \dot{V}_\theta &= -U_{0,\theta} \bar{G}(X) |S_\Omega| + \underbrace{\Delta M \left[\bar{G} \left(\frac{\partial U_{eq,\theta}}{\partial M} \right) + \frac{1}{\eta_{\theta_1}} \Delta \dot{M} \right]}_{=0} \\ &+ \Delta R_r \left[\underbrace{\bar{G} \left(\frac{\partial U_{eq,\theta}}{\partial R_r} \right) + \frac{1}{\eta_{\theta_2}} \Delta \dot{R}_r}_{=0} \right] + o(\Delta M, \Delta R_r)^2 \\ &= -U_{0,\theta} \bar{G}(X) |S_\Omega| + o(\Delta M, \Delta R_r)^2 \leq 0 \end{aligned} \quad (45)$$

Since $\bar{G}(X) > 0$, \dot{V}_θ is negative. Then, the system is stable.

3.7 Simulation results investigated SM DTC-SVM approach based position control

Simulation works have been carried out in order to investigate performances of the position control of the induction motor drive under the above-presented DTC-SVM strategies, using PID, PID with a nonlinear compensator and SM controllers. For the sake of comparison, both strategies have been considered in the same induction motor drive using the same implementation conditions, such that:

- a reference stator flux Φ_s^* equal to 1 *Wb*,
- The modulation period has been fixed to $T_{mod} = 150\mu s$ in all DTC-SVM approaches under study,
- Constants involved in the position SM controller are: $U_{0,\theta} = 50$ and $\lambda_\theta = 100$.
The constants involved in the flux SM controller are: $U_{0,\phi} = 150$ and $\lambda_\phi = 2$.

The desired trajectory is defined by smooth variations of the position θ , the speed Ω_m and the torque C_{em} , leading to:

- variations of θ form -60° (morning panel position) to 30° from 0 s to 1 s,
- constant value of θ equal to 30° from 1 s to 1.5 s.
- variations of θ form 30° to 60° (afternoon panel position) from 1.5 s to 2.5 s,
- constant value of θ equal to 60° from 2.5 s to 4 s.

The analysis of simulation results leads to the following items:

- **Figures 11 and 12** present evolutions of the position θ , the speed Ω_m , the torque C_{em} , the flux $|\Phi_s|$ and the current i_{as} , using PID controllers (figures indexed by 1), PID controllers with a nonlinear compensator (figures indexed by 2), and SM controllers (figures indexed by 3). It is well obvious that a good tracking has been realized by these control approaches. It is also obvious, that there is no significant difference between results yielded by PID controllers and PID controllers with a nonlinear compensator. This justifies that the nonlinear term $\varphi(\theta, \frac{d\theta}{dt})$ can be neglected. Moreover, ripples of the torque, the flux and stator currents are smallest for results given by SM controllers.

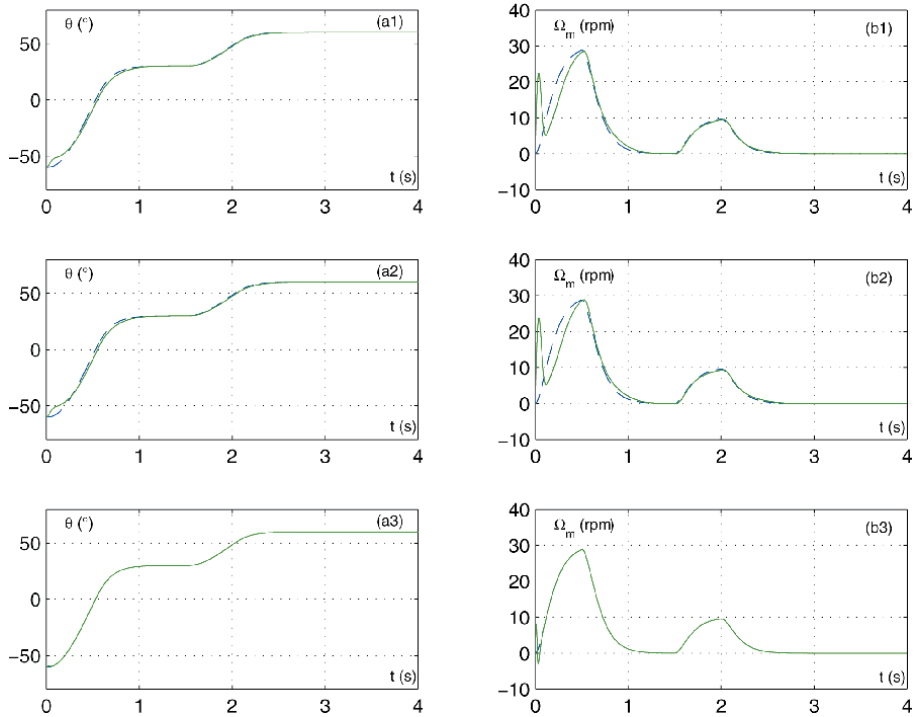


Figure 11. Induction motor position regulation considering (subscript “1”) DTC-SVM approach using PI controller, (subscript “2”) DTC-SVM approach using PI controller with a nonlinear compensator and (subscript “3”) DTC-SVM approach using sliding mode controllers. Legend: (a) evolution of the position and its reference and (b) the speed of the motor and its reference.

- **Figures 13 and 14** present the same variable evolutions for variations of machine parameters as: +100% variations on the stator resistance R_s , +100% variations on the rotor resistance R_r and -50% variations on the mutual inductance M . It is clear that results, yielded from PID controllers without and with a nonlinear compensator, present important oscillations. However, SM controllers with parameter’s updating give same results as in the case where parameters are known and do not vary.
- Thus, the implementation of the DTC-SVM using sliding mode controllers strategies highlights high dynamical performances obtained with the lowest torque ripple, the lowest flux ripple and the lowest current ripple.

3.8 Performance criteria

Considering the same simulation, we propose to use performance criteria defined in the appendix.

In the following, the steady state operating point is defined by a desired position θ equal to 60° for the time larger than 2.5 s.

- Total Harmonic Distortion (THD)

The first criterion is the average total harmonic distortion (THD) of the stator current which is defined in the Appendix.

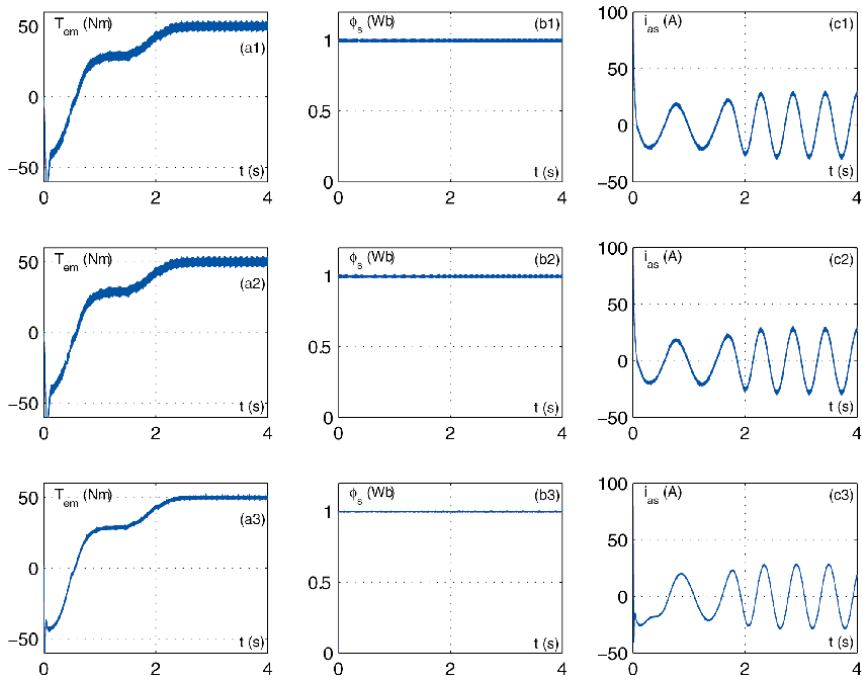


Figure 12. Induction motor position regulation considering (1) DTC-SVM approach using PI controller, (2) DTC-SVM approach using PI controller with a nonlinear compensator and (3) DTC-SVM approach using sliding mode controllers. Legend: (a) evolution of the electromagnetic torque, (b) the stator flux and (c) the stator current of phase a.

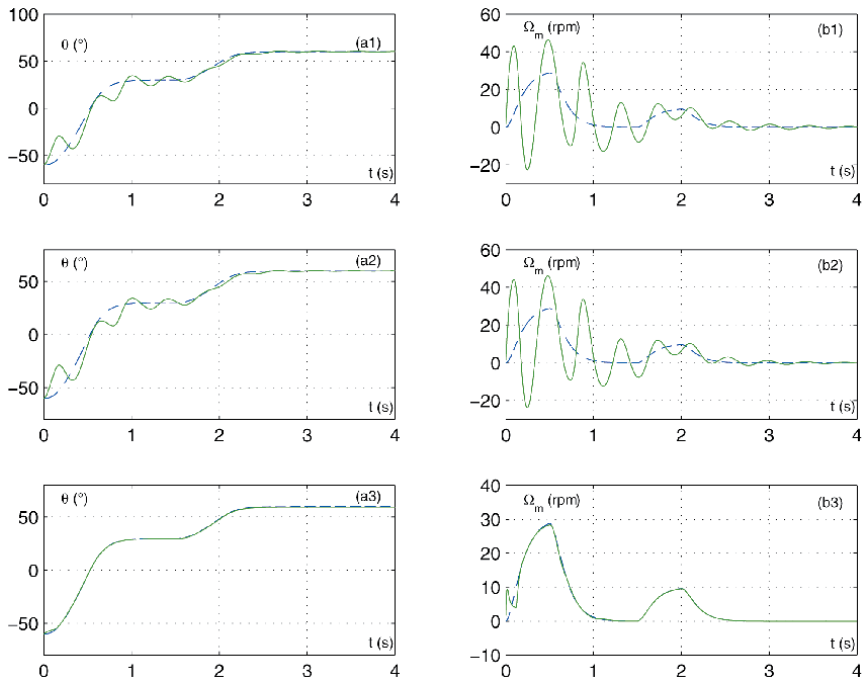


Figure 13. Induction motor position regulation, considering +100% variations on the stator resistance, (1) DTC-SVM approach using PI controller, (2) DTC-SVM approach using PI controller with a nonlinear compensator and (3) DTC-SVM approach using sliding mode controllers. Legend: (a) evolution of the position and its reference and (b) the speed of the motor and its reference.

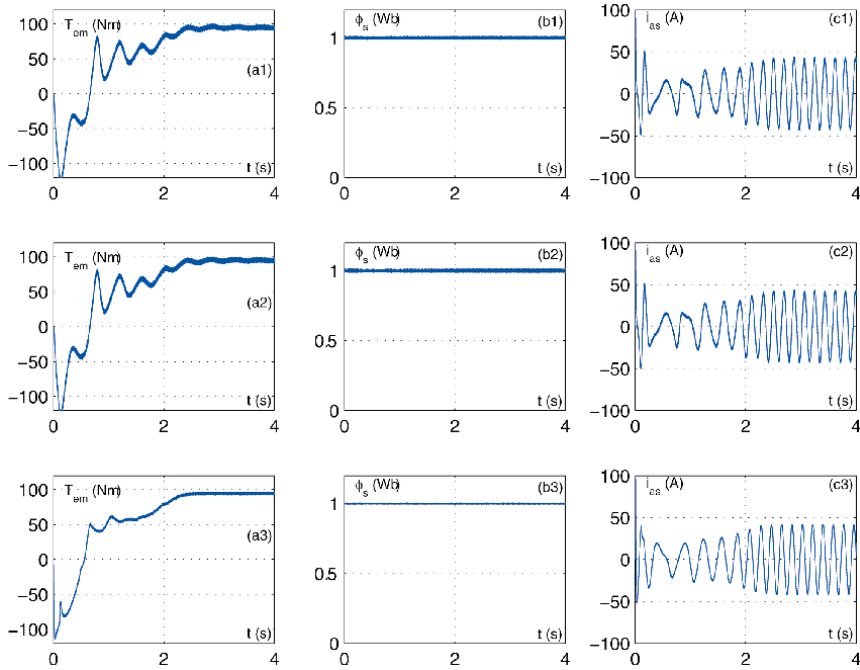


Figure 14. Induction motor position regulation, considering +100% variations on the stator resistance, considering (1) DTC-SVM approach using PI controller, (2) DTC-SVM approach using PI controller with a nonlinear compensator and (3) DTC-SVM approach using sliding mode controllers. Legend: (a) evolution of the electromagnetic torque, (b) the stator flux and (c) the stator current of phase a.

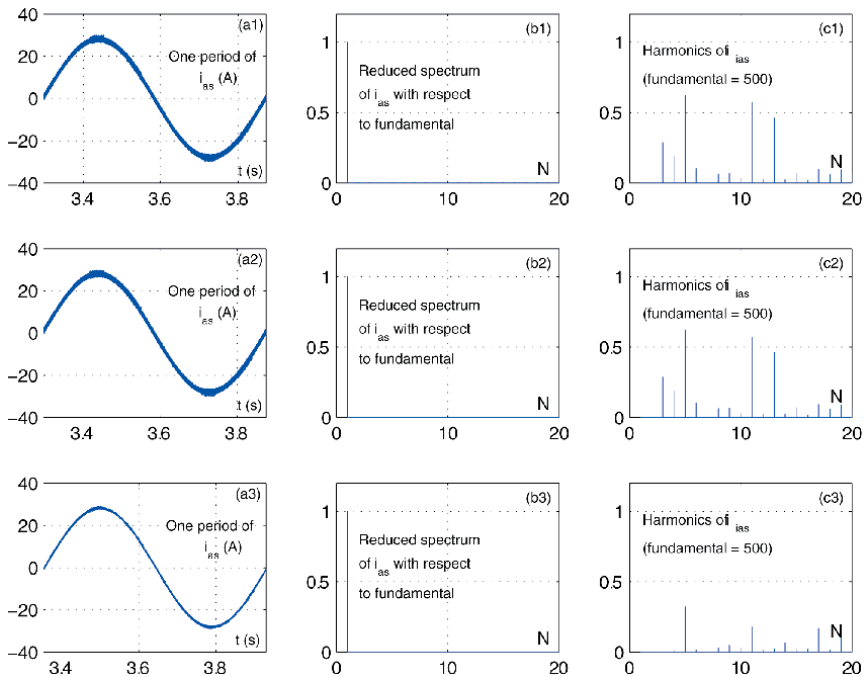


Figure 15. Spectrum of the current i_{as} . (a) Normalized spectrum, (b) higher harmonics of the spectrum current (c) one period of the current i_{as} . (subscript “1”) DTC-SVM approach using PI controller, (subscript “2”) DTC-SVM approach using PI controller with a nonlinear compensator and (subscript “3”) DTC-SVM approach using sliding mode controllers.

	PI without a NL compensator	PI with a NL Compensator	Sliding Mode Controllers
THD (%)	3.07	3.07	1.23

Table 4.
 Total harmonic distortion of the stator current i_{as} .

In this context, the frequency spectrum of the stator current i_{as} has been analyzed by the observation of amplitudes of all its harmonics frequencies. **Figure 15** shows the evolution of one period of i_{as} between 3 s and 4 s, its spectrum (only 20 harmonics has been presented). It is obvious that SM controllers give less ripples of the stator current.

The total harmonic distortion criterion of the stator current i_{as} is given by **Table 4** which shows that SM controllers give the lowest criterion.

- Ratio of torque and flux ripples.

The second comparison criterion translates the torque and the flux ripples around their steady state values $|\Phi_s| = 1$ and $T_{em,mean} = K_l \sin \frac{\pi}{6}$.

Figure 16 presents the evolution of the torque T_{em} and the flux $|\Phi_s|$ from 3 s to 4 s. Computations of flux ripple criteria are given by **Table 5**, and computations of torque ripple criteria are given by **Table 6**. These tables confirm that the PID controllers without a nonlinear compensator and PID controllers with a nonlinear compensator give same results. However, SM controllers give less ripples of the flux and the torque.

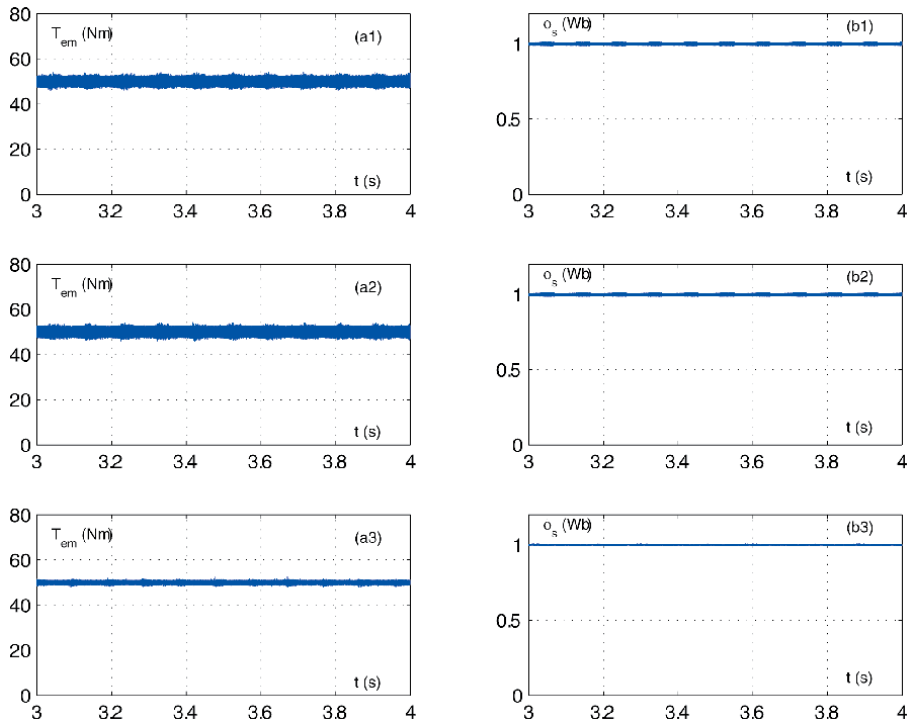


Figure 16.
 Zoomed shapes of (a) electromagnetic torque and (b) stator flux. In the case of (subscript “1”) DTC-SVM approach using PI controller, (subscript “2”) DTC-SVM approach using PI controller with a nonlinear compensator and (subscript “3”) DTC-SVM approach using sliding mode controllers.

	PI without a NL compensator	PI with a NL Compensator	Sliding Mode Controllers
$\Phi_{RIP,1}$ (%)	0.38	0.38	0.12
$\Phi_{RIP,2}$ (%)	0.44	0.44	0.15
$\Phi_{RIP,\infty}$ (%)	1.26	1.33	0.65

Table 5.
Flux ripple criteria.

	PI without a NL compensator	PI with a NL Compensator	Sliding Mode Controllers
$T_{RIP,1}$ (%)	1.88	1.86	0.92
$T_{RIP,2}$ (%)	2.71	2.66	0.62
$T_{RIP,\infty}$ (%)	8.17	8.34	4.65

Table 6.
Torque ripple criteria.

4. Conclusion

In this chapter, the DTC position control of induction motor controlling photovoltaic panel has been considered. This panel is commonly exposed to the sun in fixed positions corresponding to the maximum sunshine recorded during a day. Firstly, the DTC-SVM approach using hysteresis controllers has been compared to the basic DTC strategy and DTC strategy with a look-up table including only active voltage vectors. Then, the problem of position regulation of an IM under DTC-SVM approaches has been treated. In fact, a comparison between three DTC-SVM approaches: a DTC-SVM approach using PI controllers, a DTC-SVM approach using PI controllers with a nonlinear compensator, and a DTC-SVM approach using sliding mode controllers, has been proposed. Finally, an adaptation approach of parameter estimators has been implemented in order to eliminate the effects of parameter variations and load disturbances. It has been shown through simulations the sliding mode DTC-SVM approach (i) eliminates the demagnetization effects, and gives lowest ripples on the torque and on the flux, (ii) presents less harmonic distortion on the stator currents, and (iii) it presents good performances with a good robustness with respect to parameter's variations and load disturbances, particularly in the case of adapted estimators of machine parameters.

Author details

Fatma Ben Salem
Control and Energy Management Laboratory (CEMLab), University of Sfax, Sfax
Engineering School, BP 1173, 3038 Sfax, Tunisia

*Address all correspondence to: fatma.bensalem@isgis.usf.tn; fatma_bs@yahoo.fr

IntechOpen

© 2020 The Author(s). Licensee IntechOpen. This chapter is distributed under the terms of the Creative Commons Attribution License (<http://creativecommons.org/licenses/by/3.0>), which permits unrestricted use, distribution, and reproduction in any medium, provided the original work is properly cited. 

References

- [1] Takahashi, I., and Ohmori, Y., High Performance Direct Torque Control of Induction Machine. IEEE Power Electronics Specialists Conf. (PESC'88), 2:870–876, Kyoto-Japan, April 1988.
- [2] Depenbrock, M., 'Direct Self-Control (DSC) of Inverter-Fed Induction Machine'. *IEEE Trans. Industry Applications*, 28(3):581–588, May-juin 1992.
- [3] Ben Salem, F., and Feki, M., (2019) 'An improved DTC of Induction Motor for Electric Vehicle Propulsion: An Intent to Provide Comfortable Ride', *from book: Optimization of Green Transportation Problems: Fundamentals and Applications*, Wiley, December 16, 2019.
- [4] El Ouanjli, N., Derouich, A., El Ghzizal, A., Motahhir, S., Chebabhi, A., El Mourabit, Y., and Taoussi, M., (2019) 'Modern improvement techniques of direct torque control for induction motor drives - a review', *Protection and Control of Modern Power Systems*, 4(11): 12 pages.
- [5] Bouzidi, B., Ben Salem, F., Yangu, A., and Masmoudi, A., (2007) 'Direct Torque Control strategy Based Maximum Sunshine Position Tracking', *Second International Conference and Exhibition on Ecological Vehicles and Renewable Energies (EVER'07)*, Monte Carlo-Monaco, March–April 2007.
- [6] Bouzidi, B., Ben Salem, F., and Yangu, A., (2008) 'The Classical and Analytic DTC for Photovoltaic Panel Position and Control', *International Journal of Sciences and Techniques of Automatic Control and Computing Engineering (IJ-STA)*, special issue CEM, 636–651.
- [7] Davari, S. A., Hasankhan, E. and haburi, D. A. (2011) 'A comparative study of DTC-SVM with three-level inverter and an improved predictive torque control using two-level inverter', *2nd Power Electronics, Drive Systems and Technologies Conference*, Tehran, Iran.
- [8] Zhifeng, Z., Renyuyan, T., Boadong, B. and Dexin, X. (2010) 'Direct torque control based on space vector modulation with adaptative stator flux observer for induction motors', *IEEE Trans. Magnetics*, Vol. 48, No. 8, pp.3133–3136.
- [9] Meroufel, A., Wira, P., Nefsi, M. and Massoum, A. (2012) 'Contle directe du couple de la machine asynchrone bas sur MLI vectorielle discrtise (DSVM-DTC)', *Acta Electrotehnica*, Vol. 1, pp.35–40.
- [10] Abu-Rub, H., Stando, D. and Kazmierkowski, M.P. (2013) 'Simple speed sensorless DTC-SVM scheme for induction motor drives', *Bulletin of the Polish Academy of Sciences Technical Sciences*, Vol. 61, No. 2, pp.301–307.
- [11] Manuel, A. and Francis, J. (2013) 'Simulation of direct torque controlled induction motor drive by using space vector pulse width modulation for torque ripple reduction', *International Journal of Advanced Research in Electrical, Electronics and Instrumentation Engineering*, Vol. 2, No. 9, pp.4471–4478.
- [12] Bendaikha, A., Saad, S., Abdou, A., Defdaf, M., Laamari Y., (2019) 'A Study of SVM-DTC and Conventional DTC for Induction Motors Drive Fed by Five-level Inverter', *European Journal of Electrical Engineering*, Vol. 21, No. 1, pp.85–91.
- [13] Ben Salem, F., Bahri, I., Maamri, H. and Derbel, N. A Second-Order Sliding Mode Control of Switched Reluctance Motor, *J. of Power and Energy Systems*, 2020, doi.org/10.1080/15325008.2020.1797937, pp. 640–651.

[14] Ben Salem,F. and Derbel N., Direct torque control of induction motors based on discrete space vector modulation using adaptive sliding mode control, *Int. J. of Electric Power Components and Systems*, 2014, 42, (14), pp. 1598–1610.

[15] Ben Salem,F. and Derbel,N., A Sliding Mode field Oriented Control of an Induction Machine Operating with Variable Parameters, *J. of Power and Energy Systems*, 2007, 27,(2), pp. 205212.

[16] Ben Salem,F. and Derbel,N., DTC-SVM-Based Sliding Mode Controllers with Load Torque Estimators for Induction Motor Drives, Chapter 14 of the Book: *Applications of Sliding Mode Control, Studies in Systems, Decision and Control 79*, Springer Science +Business Media Singapore 2017, pp. 269297.

[17] F. Ben Salem and N. Derbel, “Position Control Performance Improvement of DTC-SVM for an Induction Motor: Application to Photovoltaic Panel Position”, *International Journal of Renewable Energy Research (IJRER)*, 4(4):879–892, 2014.

Section 2

Direct Torque Control
Improvements

Flux Reversal Machine Design

Yuting Gao and Yang Liu

Abstract

Flux reversal permanent magnet machines (FRPMMs) have a simple reluctance rotor and a stator with armature windings and permanent magnets (PMs). Due to the high torque density and high efficiency of FRPMMs, they have been widely used in many applications such as electric vehicle, wind power generation, etc. However, the general design method of FRPMMs has not been established in books. Therefore, this chapter will focus on introducing an analytical design method, which allows for fast design of FRPMMs. First of all, the analytical sizing equations are deduced based on a magneto motive force (MMF)-permeance model. After that, the effects of some key performances including average torque, pulsating torque, power factor, and PM demagnetization are analyzed. Moreover, the feasible slot-pole combinations are summarized and the corresponding winding type of each combination is recommended in order to maximize the output torque. Besides, the detailed geometric design of stator and rotor are presented. Finally, a case study is presented to help readers better understand the introduced design methodology.

Keywords: design method, flux reversal permanent magnet machine (FRPMM), sizing equation, finite element analysis (FEA)

1. Introduction

The topology of FRPMM is depicted in **Figure 1**. As can be seen, it has a slotted rotor without any windings or PMs, and a stator with armature windings and PMs mounted on each stator teeth. First of all, the structural characteristics of FRPMMs and the corresponding performance advantages need to be explained:

1. FRPMMs are excited by PMs instead of the excitation windings, which are different with asynchronous motors and brushed DC motors. So, for FRPMMs, the rotor will not have copper losses, and the efficiency is relatively higher [1, 2].
2. The rotor of FRPMMs has no windings or permanent magnets, thus is suitable for high-speed operation and high-temperature operating conditions [3]. Moreover, the no excitation winding will keep away from the problems of friction noise and electric spark. So, FRPMMs are more reliable and require less maintenance [4, 5]. In addition, the rotor of FRPMMs is light in weight and has a small rotational inertia [6]; hence, the acceleration and deceleration response is faster.

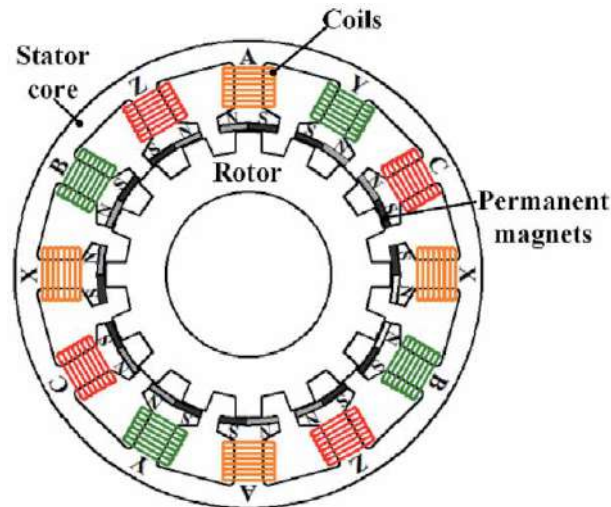


Figure 1.
Cross section of a FRPMM.

3. The stator windings of FRPMMs are mostly concentrated windings, which are easy to manufacture. Moreover, the electromagnetic isolation of the concentrated windings is better than regular distributed windings, which means that if one winding has faults, the fault is not likely to spread to other windings, and thus the fault tolerance is good [7, 8]. In addition, the concentrated winding has a smaller winding factor, inductance, and a shorter electrical time constant than the distributed windings [9], and thus the dynamic response of concentrated winding is faster.
4. Compared to other stator-PM machines, that is, flux switching PM machines and doubly salient PM machines, FRPMMs have a simpler structure. The PMs of the flux switching PM machines and doubly salient PM machines are inserted into the stator core, which is not convenient for installation. In the flux switching PM machine, putting permanent magnets in the middle of the teeth will reduce the slot area and affect the output torque. In the doubly salient PM machine, placing PMs in the yoke will increase the volume of the motor and reduce the torque density. In the FRPMMs, the PMs are pasted on the inner surface of the stator teeth, thus eliminating the above problems [10].

Finally, the structural characteristics and performance advantages of the flux-reverse motor can be summarized in **Table 1**.

It can be seen that the FRPMMs have many performance advantages, and these advantages can be utilized in different applications. First of all, the high efficiency, the large torque density, the rapid acceleration, and deceleration response make FRPMMs suitable for various high-speed rotation areas, such as electric vehicles [11–13], electric spindle [14], fans [15, 16], etc. Secondly, the number of rotor pole pairs is usually high, which is also suitable for low-speed areas, meanwhile its torque density is high at the low speeds, making FRPMMs suitable for various low-speed direct-drive occasions [17], for example wind power [18–20], direct drive servo system [21], wave power generation [22], etc. In addition, linear FRPMM has no PMs and copper windings in the secondary, which saves cost and is also very suitable for long rail transit linear motion applications [23, 24].

No.	Structural characteristic	Advantages
1	Use rare-earth PMs	1.No excitation loss, high motor efficiency; 2.Rare-earth with high-magnetic energy product increases torque density
2	No windings or PMs in the rotor	1.Simple rotor structure, suitable for high-speed operation and high temperature conditions; 2.Avoids mechanical friction and electric sparks caused by commutators and brushes, thus improving the reliability; 3.Small rotational inertia, thus fast acceleration and deceleration response
3	Often use concentrated windings	1.Good fault tolerance and high reliability; 2.Easy processing and manufacturing; 3.Small inductance and electrical time constant
4	PMs attached to the stator teeth surface	1.Easy to install 2.No reduction in the slot area or increase in the motor volume

Table 1.
Structural characteristics and corresponding advantages of FRPMM.

In most existing literatures, the design of FRPMMs is mainly based on the classical design method [25] with low accuracy or time-consuming finite element algorithm (FEA) [26]. Therefore, in this chapter, the specialized sizing equations for FRPMMs will be deduced and the analytical design method will be introduced, which can be directly employed in the initial design of FRPMMs and allows for fast calculations of machine dimensions.

This chapter is organized as follows. First, the structure and operation principles are introduced in Section 2. Then in Section 3, the magnetic circuit model is built and the sizing equations are analytically derived. After that, in Section 4, the influences of several key parameters (slot-pole combination, airgap radius, electric loading, and equivalent magnetic loading) in the sizing equation on the torque density are analyzed. Also, the effects of the airgap structural parameters on the pulsating torque, power factor, and PM demagnetization performances are investigated. Moreover, in Section 5, the geometric design of stator and rotor are introduced. And in Section 6, the design procedure is illustrated. Besides, to make the analytical design method more readable, a case study is presented and a FRPMM prototype is tested. Finally, conclusions are drawn in Section 7.

2. Operation principle of FRPMM

To clearly exhibit the operating principle, a three-phase FRPMM with two pole windings, six stator slots, and eight rotor teeth is cited as an example. The flux distributions at different rotor positions are illustrated in **Figure 2**. The magnetic flux field is excited only by the PMs, and the difference of each rotor movement is 11.25 mech. degrees (i.e., 1/4 rotor slot pitch). Taking flux linkage of phase A winding as an example, when the rotor position is 0 degree, the flux linkage is 0; when the rotor position is 11.25 mech. degree (90 elec. degree), the flux linkage reaches the positive maximum value; when the rotor position is 22.5 mech. degree (180 elec. degree), the flux linkage is 0; when the rotor position is 33.75 mech. degree (270 elec. degree), the flux linkage reaches the negative maximum value. Therefore, in the duration of one rotor slot pitch (360 elec. degrees), the winding flux linkage reverses the polarity, thus it is called “flux reversal machine.” Then,

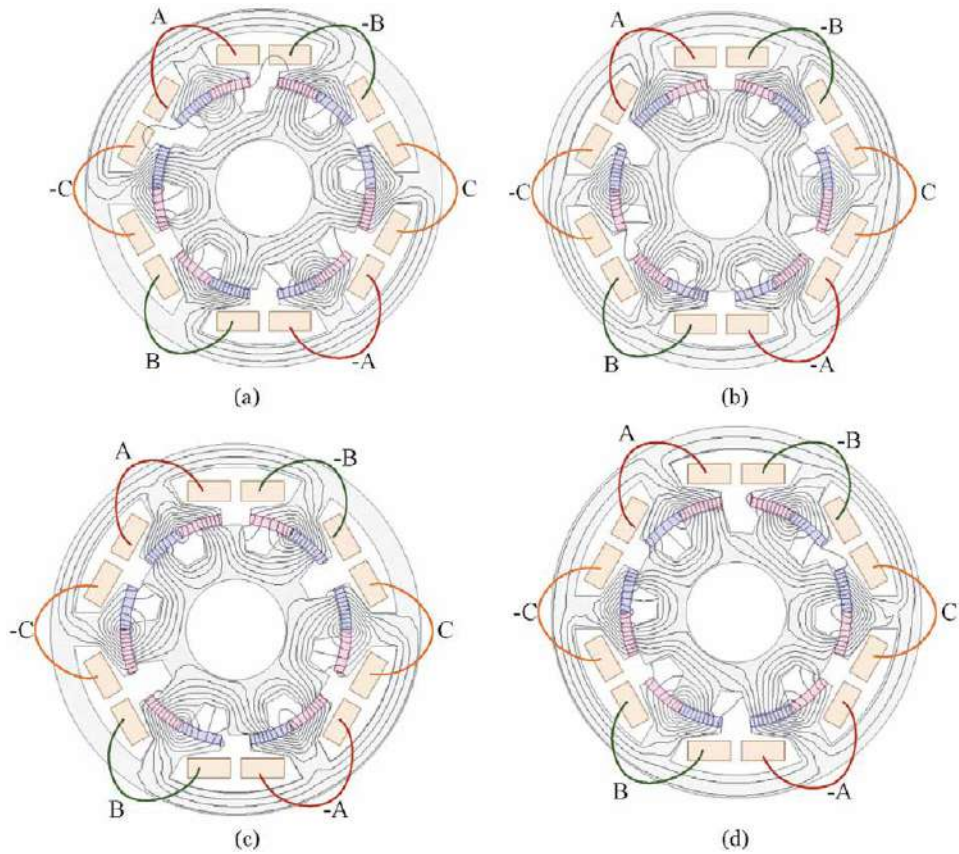


Figure 2. No-load flux lines of the FRPMM excited by the PMs: (a) rotor position = 0 elec. degree; (b) rotor position = 90 elec. degree; (c) rotor position = 180 elec. degree; (d) rotor position = 270 elec. degree.

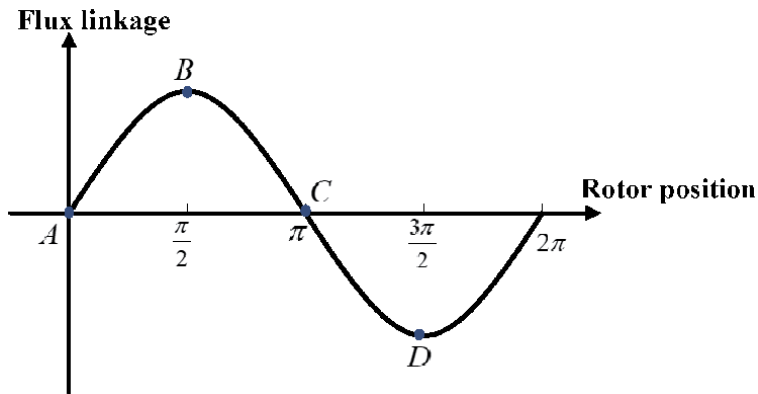


Figure 3. Variation of flux linkage of phase a winding at different rotor positions.

after obtaining the bipolar flux linkage, as shown in **Figure 3**, the winding can produce a bipolar back-electromagnetic motive force (EMF). If the armature windings are injected with currents having the same frequency and phase with the back-EMF, a steady torque can be yielded.

3. Sizing equation of FRPMM

3.1 Magnetic circuit model

In order to derive the sizing equation of FRPMMs, the magnetic circuit model should be built at first; then, based on the model, the analytical equations of airgap flux density, back-EMF, and torque will be deduced.

The equivalent magnetic circuit model can be plotted as **Figure 4**. At No.1 stator tooth, its magnetic field distribution corresponds to the position shown in **Figure 2(b)**, that is, the rotor tooth is closer to the S-pole magnet. The S-pole magnetic generates two paths of magnetic flux, one is pole leakage flux Φ_{pl} , which goes through the adjacent N-pole magnet, the other is main flux Φ_m , which goes through the stator tooth, stator yoke, rotor tooth, and rotor yoke, thus can provide winding flux linkage and back-EMF. At No. 2 stator tooth, its magnetic field distribution corresponds to the position shown in **Figure 2(c)**, that is, the rotor axis is at the same distance from the S-pole and N-pole magnets. Thus, at this time, the two magnets can only generate one magnetic flux path, that is, the pole leakage flux Φ_{pl} . At No. 3 stator tooth, its magnetic field distribution corresponds to the position shown in **Figure 2(d)**, that is, the rotor tooth is closer to the N-pole magnet. The N-pole magnetic generates two paths of magnetic flux, one is pole leakage flux Φ_{pl} , which goes through the adjacent S-pole magnet, the other is main flux Φ_m , which goes through the stator tooth, stator yoke, rotor tooth, and rotor yoke, thus can provide winding flux linkage and back-EMF. It should be noted that the magnetic flux path of No. 1 stator tooth is just opposite to that of No. 3 stator tooth, so winding flux polarity in these two cases is just opposite to each other.

As mentioned above, **Figure 4** provides the magnetic circuit of FRPMMs, which can help analyze the flux distribution of FRPMMs at different rotor positions. However, the magnetic circuit requires the establishment of the whole FRPMM

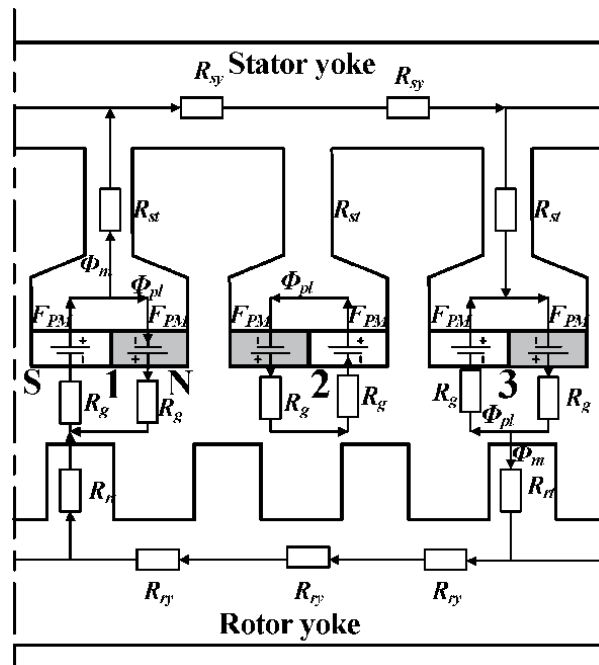


Figure 4.
 Equivalent magnetic model of FRPMMs.

magnetic path, which is rather complex. Besides, the pole leakage flux, main flux, and the reluctance at each rotor positions should be calculated, which needs high workload. Therefore, a simplified magnetic circuit should be built. Observing **Figure 2**, it can be seen that a small rotor displacement brings a large rotation in stator flux field. This phenomenon is called as flux modulation effect, i.e. a high-pole slow-speed magnetic field becomes a low-pole high-speed magnetic field through the modulation effect of iron teeth. Therefore, the physical nature of FRPMM is indeed the flux modulation effect. The research of some flux modulation machines are usually based on the PM magnetic motive force (MMF)-airgap permeance model, such as the Vernier machine in [27]. So, this chapter will use this model to analyze FRPMMs.

In PM MMF-airgap permeance model, the no-load airgap flux density $B(\theta_s, \theta)$ can be written as the product of PM MMF $F_{PM}(\theta_s)$ and specific airgap permeance $\Lambda(\theta_s, \theta)$:

$$B(\theta_s, \theta) = F_{PM}(\theta_s)\Lambda(\theta_s, \theta) \quad (1)$$

where the definitions of angles θ_s and θ are shown in **Figure 5**. Then, the simplified magnetic circuit model can be given in **Figure 6**. Once knowing the PM

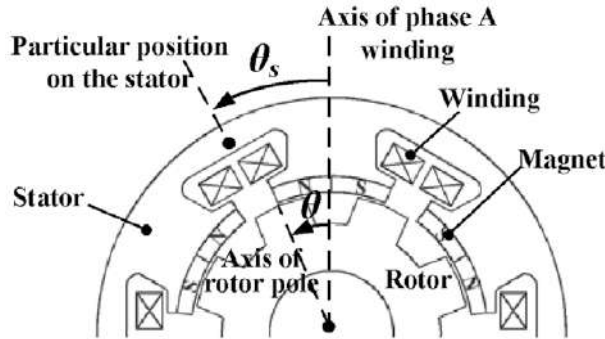


Figure 5.
Definitions of different angles in FRPMM.

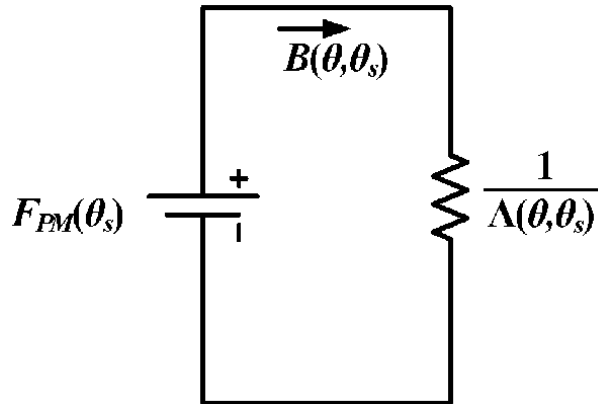


Figure 6.
Simplified equivalent magnetic model of FRPMMs.

MMF and airgap permeance, the no-load airgap flux density can be obtained. Then, the stator flux linkage $\lambda_{ph}(\theta)$ can be deduced using winding function theory:

$$\lambda_{ph}(\theta) = r_g I_{stk} \int_0^{2\pi} B(\theta_s, \theta) N(\theta_s) d\theta_s \quad (2)$$

where $N(\theta_s)$ is the phase winding function. After that, the phase back-EMF $E_{ph}(t)$ and average torque T_e can be calculated as:

$$E_{ph}(t) = \frac{d\lambda_{ph}(\theta)}{dt} \quad (3)$$

$$T_e = \frac{3}{2} E_{ph} I_{ph} \quad (4)$$

where I_{ph} is the peak value of phase current. Therefore, from Eqs. (1–4), it can be found that if the torque equation need to be calculated, the key is to obtain the equation of airgap flux density $B(\theta_s, \theta)$, which is further determined by the PM MMF $F_{PM}(\theta_s)$ and specific airgap permeance $\Lambda(\theta_s, \theta)$. Therefore, in the next parts, the equations of the PM MMF $F_{PM}(\theta_s)$ and specific airgap permeance $\Lambda(\theta_s, \theta)$ will be deduced in detail.

3.2 Airgap flux density equation

As aforementioned, to derive the torque equation, the no-load airgap flux density $B(\theta_s, \theta)$ should firstly be known, whose equation can be given as Eq. (1). Then, the next step is to derive the expressions of $F_{PM}(\theta_s)$ and $\Lambda(\theta_s, \theta)$. The PM MMF waveform excited by the magnets is shown in **Figure 7**, which can be given as:

$$F_{PM}(\theta_s) = \begin{cases} F_C; & 0 \leq \theta_s < (1 - SO)\pi/Z_s \\ 0; & (1 - SO)\pi/Z_s \leq \theta_s < (1 + SO)\pi/Z_s \\ F_C; & (1 + SO)\pi/Z_s \leq \theta_s < 2\pi/Z_s \\ -F_C; & 2\pi/Z_s \leq \theta_s < (3 - SO)\pi/Z_s \\ 0; & (3 - SO)\pi/Z_s \leq \theta_s < (3 + SO)\pi/Z_s \\ -F_C; & (3 + SO)\pi/Z_s \leq \theta_s < 4\pi/Z_s \end{cases} \quad (5)$$

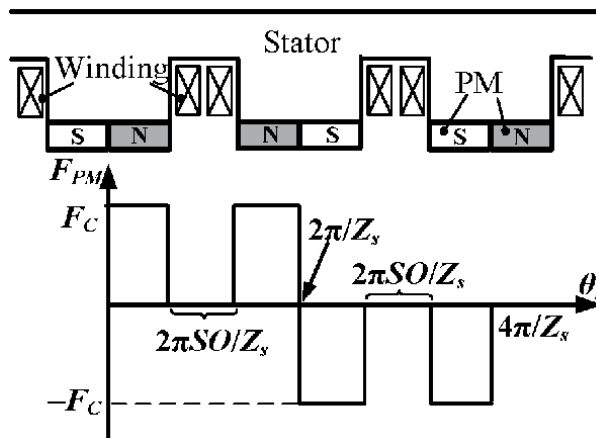


Figure 7.
Magnet MMF waveform.

where F_C is:

$$F_C = \frac{B_r h_m}{\mu_r \mu_0} \quad (6)$$

Then, it can be written in Fourier series as follows:

$$F_{PM}(\theta_s) = \sum_{i=1,3,5}^{\infty} F_i \sin\left(\frac{iZ_s}{2}\theta_s\right) \quad (7)$$

where the magnitude F_i is

$$F_i = \frac{4}{\pi} \frac{1}{i} \frac{B_r h_m}{\mu_0 \mu_r} \left[1 + (-1)^{\frac{i+1}{2}} \sin\left(\frac{i\pi}{2} SO\right) \right] \quad (8)$$

Then, the next step is to derive the specific airgap permeance $\Lambda(\theta_s, \theta)$ in Eq. (1). Since the stator slotting effect has already been considered in Eqs. (5–8), the specific airgap permeance $\Lambda(\theta_s, \theta)$ can be replaced by the airgap permeance with smoothed stator and slotted rotor $\Lambda_r(\theta_s, \theta)$. The model of smoothed stator and slotted rotor is shown in **Figure 8**. Then, the $\Lambda_r(\theta_s, \theta)$ can be expressed by:

$$\Lambda_r(\theta_s, \theta) \approx \Lambda_{0r} + \Lambda_{1r} \cos[Z_r(\theta_s - \theta)] \quad (9)$$

The coefficients of the airgap permeance function Λ_{0r} and Λ_{1r} in Eq. (9) can be obtained using the conformal mapping method [28, 29]:

$$\Lambda_{0r} = \frac{\mu_0}{g'} \left(1 - 1.6\beta \frac{b_o}{t} \right) \quad (10)$$

$$g' = g + h_m / \mu_r \quad (11)$$

$$\Lambda_{1r} = \frac{\mu_0}{g'} \frac{4}{\pi} \beta \left[0.5 + \frac{(b_o/t)^2}{0.78125 - 2(b_o/t)^2} \right] \sin\left(1.6\pi \frac{b_o}{t}\right) \quad (12)$$

$$\beta = 0.5 - \frac{1}{2\sqrt{1 + \left(\frac{b_o t}{2g'}\right)^2}} \quad (13)$$

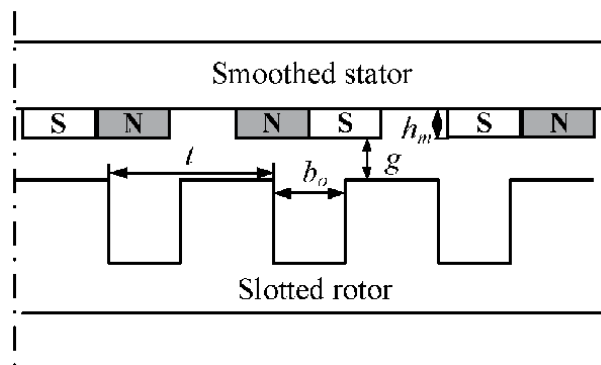


Figure 8. Schematic of single-side salient structure on rotor.

where b_o is the rotor slot opening width and t is the rotor slot pitch, as shown in **Figure 8**. Combining Eq. (1), Eqs. (5–13), the no-load airgap flux density $B(\theta_s, \theta)$ can be finally calculated as:

$$B(\theta_s, \theta) = \sum_{i=1,3}^{\infty} B_i \sin \left[\left(\frac{iZ_s}{2} \pm Z_r \right) \theta_s - Z_r \theta \right] \quad (14)$$

where the magnitude B_i is

$$B_i = \frac{1}{2} F_i \Lambda_{1r}, \quad i = 1, 3, 5 \dots \quad (15)$$

3.3 Slot-pole combinations

As can be seen in Eq. (14), the number of pole pairs in the air gap flux density is $iZ_s/2 \pm Z_r$, $i = 1, 3, 5 \dots$. Then, in order to make the flux density induce EMF in the armature windings, the pole pair number of the armature windings P should be equal to $iZ_s/2 \pm Z_r$, $i = 1, 3, 5 \dots$. Besides, for three phase symmetry, the winding pole pair number must also meet the following requirement:

$$\frac{Z_s}{\text{GCD}(Z_s, P)} = 3k, \quad k = 1, 2, 3 \dots \quad (16)$$

All in all, the slot-pole combination of three-phase FRPMMs is ruled by the following equation:

$$P = \min \left\{ P = \frac{iZ_s}{2} \pm Z_r; \quad \frac{Z_s}{\text{GCD}(Z_s, P)} = 3k \right\} \quad (17)$$

$$i = 1, 3, 5 \dots \quad k = 1, 2, 3 \dots$$

where min means to select the minimum number of these qualified harmonic orders so as to obtain a maximal pole ratio of FRPMMs. Therefore, the feasible slot-pole combinations can be summarized as **Table 2**. Non-overlapping windings (i.e., concentrated windings) are usually used in FRPMMs because of the higher fault tolerance and easier manufacture than regular overlapping windings. However, some FRPMMs are suggested to employ overlapping windings in order to have a larger winding factor and thus a higher torque density. Therefore, both winding factors, that is, k_{wn} (using non-overlapping winding) and k_{wr} (using overlapping winding) are calculated for each FRPMM so as to see the difference of using different winding types.

3.4 Torque equation

Once the stator winding pole pair is selected, the stator flux linkage can be deduced using winding function theory, just as mentioned in Eq. (2). The winding function $N(\theta_s)$ in Eq. (2) can be written as:

$$N(\theta_s) = \sum_{i=1,3,5}^{\infty} N_i \cos(iP\theta_s) \quad (18)$$

$$N_i = \frac{2}{i\pi} \frac{N_s}{P} k_{wi} \quad (19)$$

Z_s	Z_r	2	3	4	5	6	7	8	10	11	12	13	14	15	16
6	P	1	1	1	2	2	2	1	1	2	2	2	1	1	1
	SPP	1	1	0.5	0.5	0.5	0.5	1	1	0.5	0.5	0.5	1	1	1
	PR	2	4	2.5	3.5	8	8	10	10	5.5	6.5	6.5	14	16	16
	k_{wm}	0.5	0.5	0.866	0.866	0.866	0.866	0.5	0.5	0.866	0.866	0.866	0.5	0.5	0.5
	k_{wr}	1	1	0.866	0.866	0.866	0.866	1	1	0.866	0.866	0.866	1	1	1
12	P	4	2	1	1	1	1	2	4	5	5	4	4	2	2
	SPP	0.5	1	2	2	2	2	1	0.5	0.4	0.4	0.4	0.5	1	1
	PR	0.5	2	5	7	7	7	4	2.5	2.2	2.6	2.6	3.5	8	8
	k_{wm}	0.866	0.5	0.25	0.25	0.25	0.25	0.5	0.866	0.933	0.933	0.933	0.866	0.866	0.5
	k_{wr}	0.866	1	0.966	0.966	0.966	0.966	1	0.866	0.933	0.933	0.933	0.866	0.866	1
18	P	7	6	5	4	3	2	1	1	2	3	4	5	6	7
	SPP	3/7	0.5	0.6	0.75	1	1.5	3	3	1.5	1	0.75	0.6	0.5	3/7
	PR	2/7	0.5	0.8	1.25	2	3.5	8	10	5.5	4	3.25	2.8	2.5	16/7
	k_{wm}	0.902	0.866	0.735	0.617	0.5	0.492	0.167	0.167	0.492	0.5	0.617	0.735	0.866	0.902
	k_{wr}	0.902	0.866	0.945	0.945	1	0.945	0.96	0.96	0.945	1	0.945	0.945	0.866	0.902
PS:	Non-overlapping winding is recommended.														
	Other: Overlapping winding is recommended.														
k_{wm} and k_{wr} are fundamental winding factors calculated based on non-overlapping winding type and recommended winding types, respectively.															

Table 2. Slot-pole combinations of three-phase FRPMM.

where N_i is the i th harmonics of the winding function and k_{wi} is the winding factor of the i th harmonics. As can be seen in Eq. (17), the pole pair number is $iZ_s/2 \pm Z_r$ ($i = 1, 3, 5 \dots$). So, the sum or difference of any two pole pair harmonics P_{i1} and P_{i2} is a multiple of stator slot number, that is,

$$\begin{cases} P_{i1} = i_1 Z_s / 2 \pm Z_r \\ P_{i2} = i_2 Z_s / 2 \pm Z_r \\ |P_{i1} \pm P_{i2}| = k Z_s, \quad k = 1, 2, 3 \dots \end{cases} \quad (20)$$

Therefore, all the flux density harmonics are tooth harmonics of each other, that is, they have the same absolute values of winding factors, and their absolute winding factor equals the fundamental winding factor k_{w1} :

$$|k_{wP_{i1}}| = |k_{wP_{i2}}| = k_{w1} \quad (21)$$

Then, combining Eq. (2), Eq. (3), Eqs. (18–21), the back-EMF can be finally obtained as:

$$E_{ph} = 2\omega_m r_g l_{stk} N_s Z_r k_{w1} \sum_{i=1}^{\infty} \text{sgn} * \frac{B_i}{\left(\frac{iZ_s}{2} \pm Z_r\right)/P} \quad (22)$$

where

$$\text{sgn} = \begin{cases} 1, \text{winding factor of } (iZ_s/2 \pm Z_r)^{\text{th}} \text{ harmonic equals } k_{w1} \\ -1, \text{winding factor of } (iZ_s/2 \pm Z_r)^{\text{th}} \text{ harmonic equals } -k_{w1} \end{cases} \quad (23)$$

Since the reluctance torque of FRPMM is negligible, the electromagnetic torque under $i_d = 0$ control can be expressed as Eq. (4). Then, combining Eq. (4) and Eq. (22), the average torque T_e is able to be calculated as:

$$T_e = 3I_{ph} r_g l_{stk} N_s Z_r k_{w1} \sum_{i=1}^{\infty} \text{sgn} * \frac{B_i}{\left(\frac{iZ_s}{2} \pm Z_r\right)/P} \quad (24)$$

So far, the general torque equation has been obtained as Eq. (24), but in this equation, some parameters such as B_i , I_{ph} cannot be determined in the initial design stage of FRPMMs, so it is desirable that Eq. (24) can be transformed to a combination of several basic parameters, such as electric loading, magnetic loading, which can be easily determined in the initial design stage.

As known for electrical machines, the electric loading A_e can be written as:

$$A_e = \frac{6N_s I_{ph}}{2\sqrt{2}\pi r_g} \quad (25)$$

Then, the equivalent magnetic loading of three-phase FRPMM B_m is defined as:

$$B_m = \sum_{i=1}^{\infty} \text{sgn} * \frac{B_i}{\left(\frac{iZ_s}{2} \pm Z_r\right)/P} \quad (26)$$

So, the torque expression in Eq. (24) can be rewritten as:

$$T_e = \sqrt{2}\pi r_g^2 l_{stk} k_w Z_r A_e B_m \quad (27)$$

Thus, the rotor volume V_r , which equals $\pi l_{stk} r_g^2 g$, can be obtained:

$$V_r = \frac{T_e}{\sqrt{2} k_w Z_r A_e B_m} \quad (28)$$

and then the airgap radius r_g and the stack length l_{stk} can be derived as:

$$r_g = \sqrt[3]{V_r / (\pi k_{lr})} \quad (29)$$

$$l_{stk} = \sqrt[3]{V_r k_{lr}^2 / \pi} \quad (30)$$

where k_{lr} is the aspect ratio, equals to the ratio of r_g to l_{stk} . It can be found in Eq. (27) that the key parameters affecting the torque density are the airgap radius r_g , stack length l_{stk} , winding factor k_w , rotor slot number Z_r , electric loading A_e , and equivalent magnetic loading B_m , among which the stack length l_{stk} can be determined by the volume requirement, and winding factor k_w is approximate to 1. So, the remaining parameters r_g , Z_r , A_e , B_m should be determined at the initial stage of the design process. Thus, the influences of the above key parameters on important performances, such as average torque, pulsating torque, power factor, PM demagnetization performance, will be investigated in the following parts.

4. Influence of design parameters on key performances

4.1 Average torque performances

4.1.1 Influence of slot-pole combinations on average torque

As aforementioned, the rotor slot number Z_r is one of key parameters that should be determined in the first design stage. How to determine the rotor slot number is a question. In this part, the influence of Z_r on the torque performance will be investigated, giving instruction on how to select Z_r . The parameters of the FRPMM models are listed in **Table 3**. These parameters are kept the same for the FRPMMs in order to have a reasonable comparison of their torque performance. That is to say, the airgap radius r_g , stack length l_{stk} , and electric loading A_e are the same.

Figure 9 shows the influence of rotor slot number on the output torque when non-overlapping windings and recommended windings are used respectively. For **Figure 9(a)**, when non-overlapping windings are adopted, the average torque is mainly related to the product of winding factor and rotor slot number, that is,

Parameter	Value	Parameter	Value
Stator outer diameter	170 mm	Stator inner diameter	105 mm
Stator slot opening ratio	0.25	Remanent permeability	1.065
Stack length	100 mm	PM thickness	2.5 mm
Series turns per phase	80	Airgap length	0.5 mm
Rotor slot opening ratio	0.65	Rated current	5.3A
Rated speed	600 rpm	Magnet remanence	1.21 T

Table 3.
Parameters of the three-phase FRPMM models.

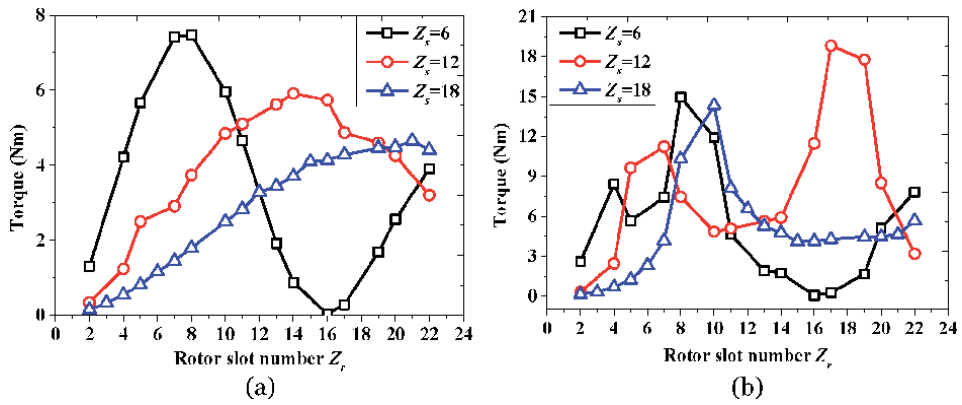


Figure 9. Effect of combinations of stator slots and rotor slots on torque: (a) non-overlapping windings; (b) recommended windings.

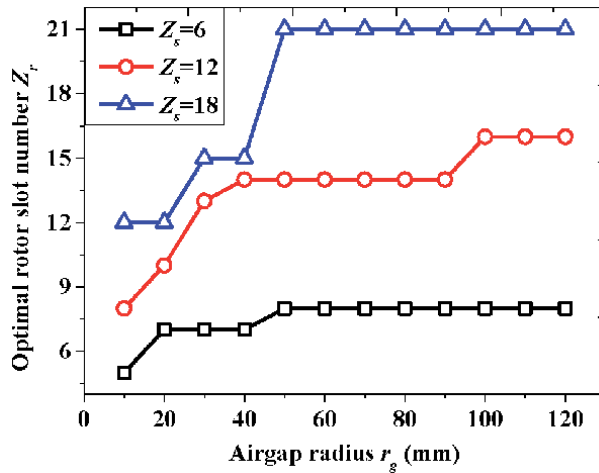


Figure 10. Effect of x_g on optimal Z_r when split ratio is 0.6.

$k_w * Z_r * B_m$. Since the machine volume and PM usage are kept the same, the equivalent magnet loading B_m is mainly determined by the pole ratio (PR). So, the variation trend of torque is similar to that of $k_w * Z_r * PR$. It can be seen that the torque achieves the maximum value when the rotor slot number is 8, 14, and 21 for 6 stator slots, 12 stator slots, and 18 stator slots, respectively. When the recommended windings are used, which means that the winding factor are maximized, the main factor that affects the torque is the $Z_r * PR$. As shown in **Table 2**, the variation of PR is irregular, hence the variation of torque with rotor slot number is irregular. As can be seen, for recommended winding types, the torque achieves the maximal value when the rotor slot number is 8, 10 and 17 for 6 stator slots, 12 stator slots, and 18 stator slots, respectively.

4.1.2 Influence of airgap radius on average torque

As shown in Eq. (27), the airgap radius r_g is also very important for the output torque. **Figure 10** investigates the effect of optimal rotor slot number Z_r at different r_g . For 6, 12, 18 stator slots, their rotor slot numbers are selected as 8, 14, and 21,

respectively. Moreover, non-overlapping windings are used in these models because non-overlapping winding is simple and has the same end winding length. It can be seen that when the airgap radius is small, the optimal rotor slot number is small. This is because when the airgap radius is small, the leakage flux between adjacent rotor teeth occupies a large percent, so the optimal rotor slot number should be small to reduce the leakage flux as much as possible. When the airgap radius gets larger and larger, the leakage flux decreases gradually. Hence, the optimal rotor slot number increases.

Then, keeping the stator outer diameter as a constant, that is, 170 mm, the effects of airgap radius of average torque are analyzed in **Figure 11**. It indicates that when the airgap radius increases, the output torque goes up. This is because the torque is proportional to the square of airgap radius. The larger the airgap radius, the higher the torque. However, the torque is not only influenced by the airgap radius, but also the electric loading A_e . With the increase of airgap radius, the inner diameter of the stator increases, and thus the slot area decreases, leading to the decrease of winding turns per slot and the electric loading. Therefore, as the airgap radius keeps increasing, the output torque decreases afterwards.

4.1.3 Influence of magnetic loading and equivalent electric loading on average torque

In addition to the rotor slot number Z_r , airgap radius r_g , the rest of key parameters affecting the torque in Eq. (27) are the electric loading A_e and the equivalent magnetic loading B_m . **Figure 12** analyzes the influence of A_e and B_m on the average torque at different stator slot number. For these models, the airgap radius is fixed as 55 mm and their rotor slot number is chosen as their corresponding optimal value. Also, non-overlapping windings are adopted. As can be seen, the output torque increases with the electric loading. This reason is very simple, that is, a larger current, a higher torque. But for the equivalent magnetic loading, the variation trend of torque does not monotonically increase with the equivalent magnetic loading. This is due to the saturation effect of the iron core. Moreover, it can be seen that the knee point of the equivalent magnet loading increases with the stator slot number. Since the winding pole pair of the 18-stator-slot FRPMM is 6, which is larger than 1-winding-pole-pair of the 6-stator-slot and 4-winding-pole-pair of the

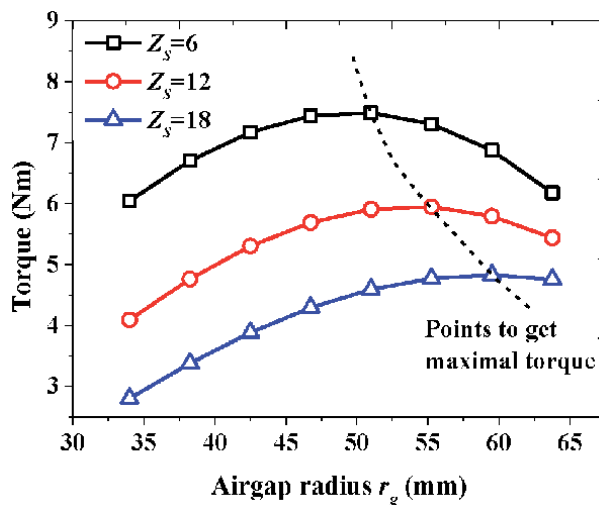


Figure 11.
Effect of r_g on torque when stator outer diameter is 170 mm.

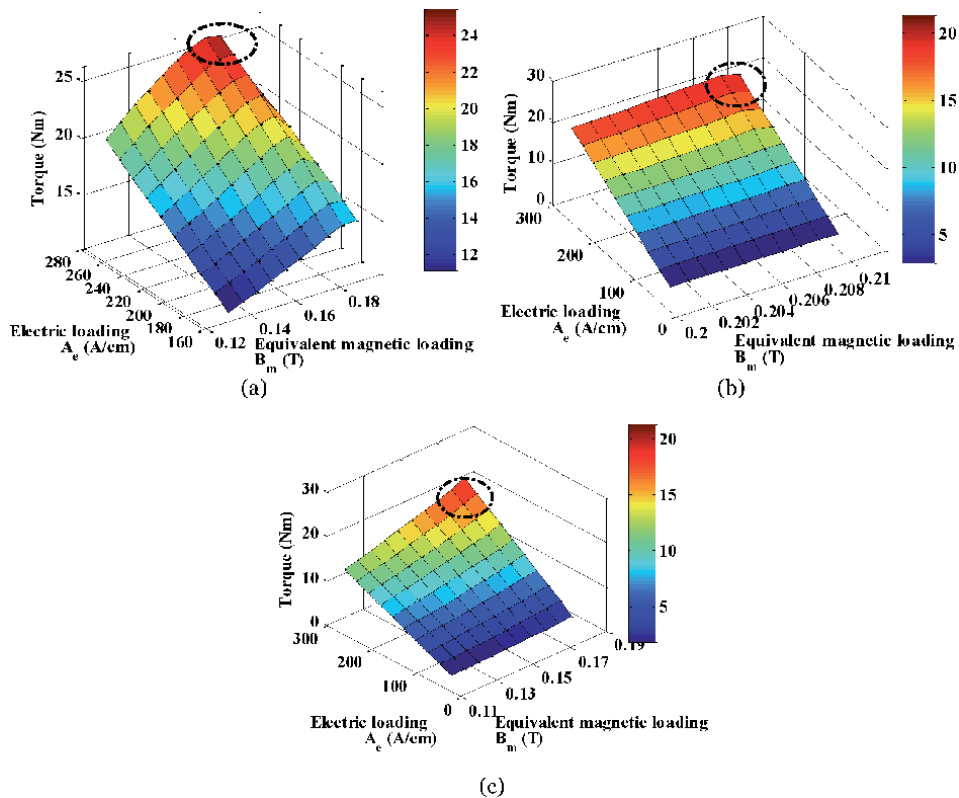


Figure 12. Effect of equivalent magnetic loading and electric loading on torque: (a) $Z_s = 6$; (b) $Z_s = 12$; (c) $Z_s = 18$.

12-stator-slot FRPMM, the stator iron of the 18-stator-slot FRPMM is less likely to saturate than the others.

4.2 Pulsating torque performances

4.2.1 Influence of slot-pole combinations on pulsating torque

Apart from the torque density, pulsating torque is also very important because a large pulsating torque will increase the vibration and noise of machines. **Figure 13** shows the cogging torque and ripple torque waveforms of 13-, 14-, 16-, 17-, and 19-rotor-slot FRPMMs. The stator slot number of these models is all chosen as 12. For the rated torque, we can see in **Figure 13(b)** that the 14-rotor-slot FRPMM yields the largest among the five models. As for the pulsating torque, we can see that the cogging torque and ripple torque of 16-rotor-slot FRPMM are the largest, and that of 19-rotor-slot FRPMM is the least. This phenomenon is related to the least common multiple of stator slot number and rotor slot number. The larger least common multiple, the lower pulsating torque. The least common multiples of the 13-, 14-, 16-, 17-, and 19-rotor-slot FRPMMs are 156, 84, 48, 204, and 228, respectively. Therefore, the 19-rotor-slot FRPMM exhibit the lowest cogging torque and ripple torque. However, attentions should be paid to use odd rotor number because it will cause other problems such as eccentricity stress. **Figure 14** compares the radial stress of the five FRPMM models. It can be seen that for the even rotor slot number FRPMMs, that is, 14 and 16 rotor slots, the stress harmonics only have even orders, which will not lead to eccentricity. However, for the odd rotor slot number

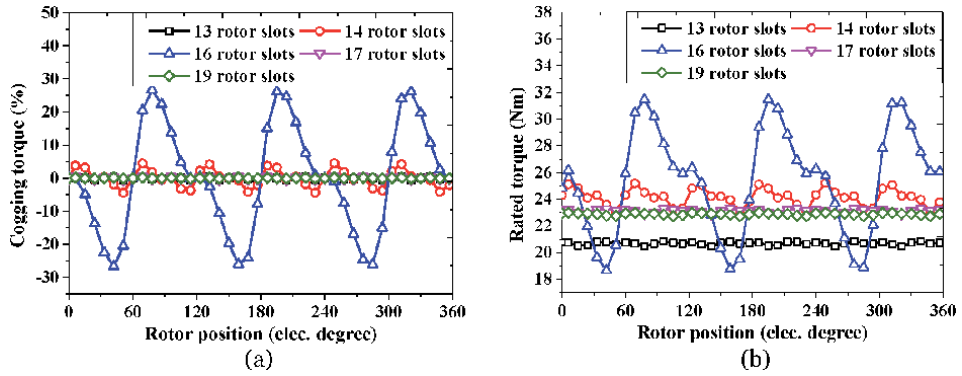


Figure 13. Effect of slot-pole combination on pulsating torque performances: (a) cogging torque waveforms (%); (b) rated torque waveforms.

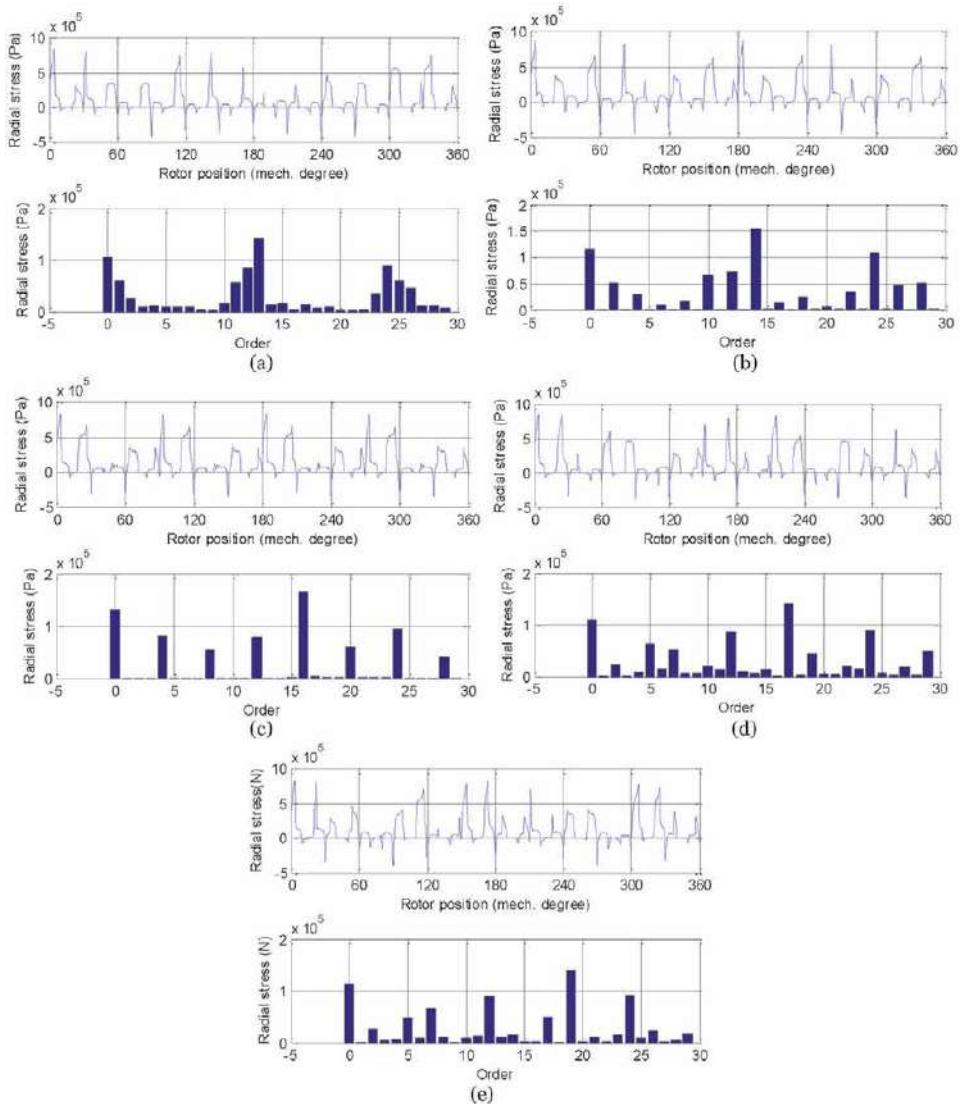


Figure 14. Radial stress analysis of the FRPMMs: (a) 13-rotor-slot; (b) 14-rotor-slot; (c) 16-rotor-slot; (d) 17-rotor-slot; (e) 19-rotor-slot.

FRPMMs, that is, 13, 17, and 19 rotor slots, there are many odd stress harmonics. Since the first-order harmonic is dominant for the eccentricity, the 13-rotor-slot FRPMM has a large eccentricity stress. Therefore, 13-rotor-slot is not recommended. The first-order stress harmonic for 17 and 19 rotor slots are very small, so their eccentricity can be neglected.

4.2.2 Influence of PM thickness and split ratio on pulsating torque

The influences of split ratio and PM thickness on cogging torque and ripple torque of FRPMMs are also analyzed in **Figure 15**. This figure is plotted based on the 14-rotor-slot, which is chosen because it has the largest torque density and a relatively low pulsating torque, as shown in **Figure 13**. It can be found in **Figure 15(a)** that the cogging torque increases with the PM thickness and the split ratio. When the PM thickness increases, the airgap flux density increases, and thus the interaction between the PMs and slot-teeth becomes greater, which leads to a higher cogging torque. As the split ratio increases, the airgap radius increases, hence the cogging torque increases with the split ratio [30]. As for the ripple torque, the ripple torque has the maximum value when the split ratio is around 0.66. This is because the ripple torque is not only related to the slot structure but also influenced by the electric loading. As aforementioned, the pulsating torque resulting from the slot structure is increased with the split ratio. However, as the split ratio increases, the slot area is reduced and the electric loading gets smaller and smaller, so the ripple torque resulting from the electric loading becomes lower. Considering these two impacts, the ripple torque has a maximal value when the split ratio changes.

4.2.3 Influence of slot opening ratios on pulsating torque

As we know, the airgap structure is significant for the pulsating torque because the pulsating torque results from the interaction between the two sides of the airgap, that is, stator and rotor. Therefore, this chapter also analyzes the influences of stator slot opening ratio and rotor slot opening ratio on cogging torque and ripple torque. Here, the stator/rotor slot opening ratio is defined as the ratio of stator/rotor slot opening width to the stator/rotor slot pitch. **Figure 16** shows the variation of cogging torque and ripple torque with the two slot opening ratios. It can be seen that the cogging torque increases with the stator slot opening ratio. The reason is that a larger stator slot opening ratio reduces the PM width and the smoothness of PM MMF, thus the changing of the PM MMF along the tangential direction increases

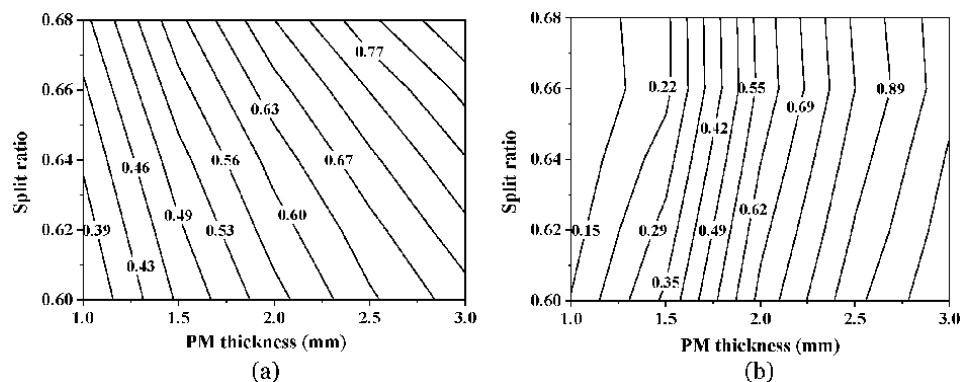


Figure 15. Effect of split ratio and PM thickness on pulsating torque performances: (a) cogging torque (%); (b) ripple torque (%).

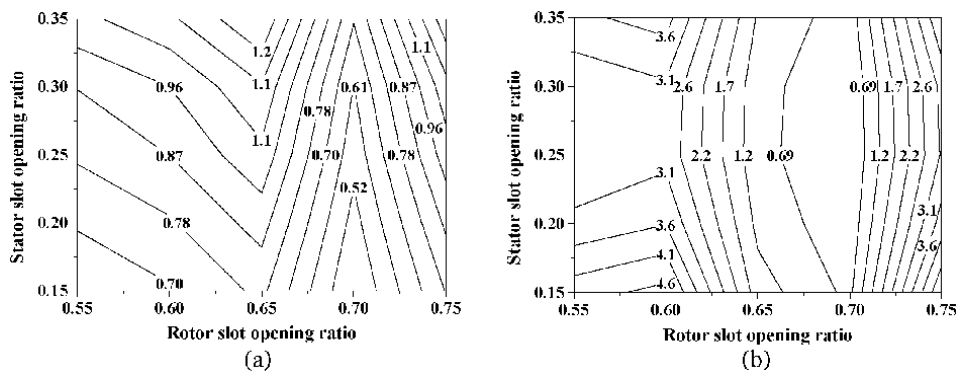


Figure 16.

Effect of stator slot opening ratio and rotor slot opening ratio on pulsating torque: (a) cogging torque (%); (b) ripple torque (%).

the cogging torque. As for the rotor slot opening ratio, which simultaneously influences all the harmonic contents of the airgap permeance, it has great and nonlinear impact on the pulsating torque. Since the pulsating torque results from the interaction of multi permeance harmonics, the variation of pulsating torque changes nonlinearly with the rotor slot opening ratio. It can be seen in **Figure 16** that the optimal cogging torque and ripple torque can be achieved when the stator slot opening ratio and rotor slot opening ratio are around 0.25 and 0.7, respectively.

4.3 Power factor performances

4.3.1 Influence of stator inner diameter and PM thickness on power factor

Since the power factor of FRPMMs is usually low, which is around 0.4–0.7, meanwhile a low power factor will increase the converter capacity and cost, the influences of key parameters on the power factor should be also analyzed to achieve a relatively high power factor. The power factor can be given as:

$$PF = 1/\sqrt{1 + \left(\frac{L_s I_s}{\psi_m}\right)^2} \quad (31)$$

where I_s is the winding current, L_s is the synchronous inductance (because the saliency ratio is approximate to 1, $L_d \approx L_q$), and ψ_m is the PM flux linkage. Then, the effect of stator inner diameter on power factor is shown in **Figure 17**. Here, the stator outer diameter is kept as 124 mm, and the airgap length is fixed as 0.5 mm. It can be found that with the increase of stator inner diameter, the power factor increases continuously. The reason is that with the increase of stator inner diameter, the slot area decreases, so the winding turns per phase decreases, thus leading to the reduction of the synchronous inductance L_s . The lower L_s , the higher power factor, as shown in Eq. (31). Apart from the stator inner diameter, another important parameter affecting the power factor is the PM thickness h_m . **Figure 18** investigates the variation of power factor with respect to the PM thickness. It indicates that the power factor initially increases with the PM thickness but then decreases. The reason is explained as follows. As the PM thickness increases, the PM flux linkage ψ_m becomes larger, so the power factor increases. However, the synchronous inductance L_s also increases with the PM thickness, which leads to the reduction of power factor afterwards. Therefore, there is an optimal PM thickness for a maximum achievable power factor.

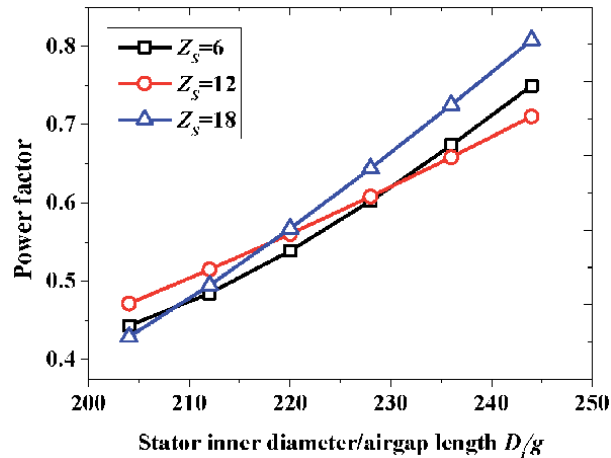


Figure 17.
 Effect of stator inner diameter/airgap length on power factor.

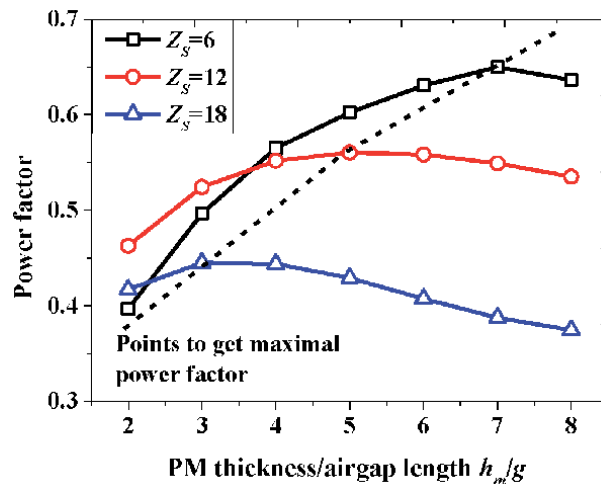


Figure 18.
 Effect of PM thickness/airgap length on power factor.

4.3.2 Influence of slot opening ratio on power factor

Another important parameter that influences the airgap structure is the slot opening ratio. Hence, **Figures 19** and **20** analyzes the effect of stator slot opening ratio and rotor slot opening ratio on pulsating torque performances, respectively. It can be seen in **Figure 19** that the maximum power factor can be obtained when the stator slot opening ratio is approximately to 0.3. The explanation is as follows. When the stator slot opening ratio is too small, the slot leakage flux between the stator tips is large, thus the main flux is reduced, and the back-EMF is lowered, resulting in smaller back-EMF. And when the stator slot opening ratio is too large, the PM width will be narrower. Although the slot leakage flux is reduced, the main flux is not high due to the narrower PMs, thus the back-EMF is lowered. Therefore, the stator slot opening ratio cannot be too small or too large, that is, there is an optimal value for the stator slot opening ratio.

Then, the influences of rotor slot opening ratio on power factor can be seen in **Figure 20**. It indicates that when the rotor slot opening ratio is around 0.7, the

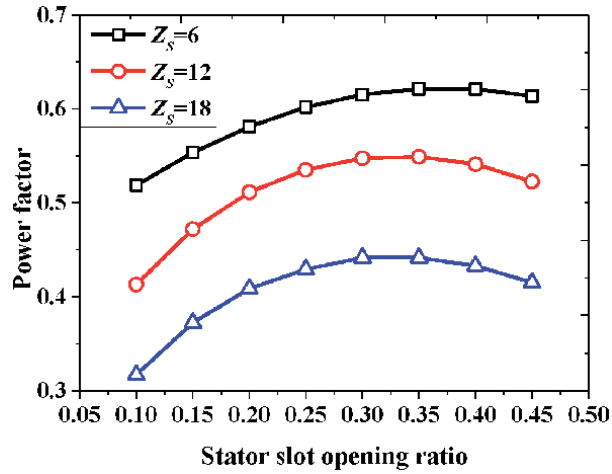


Figure 19.
Effect of stator slot opening ratio on power factor.

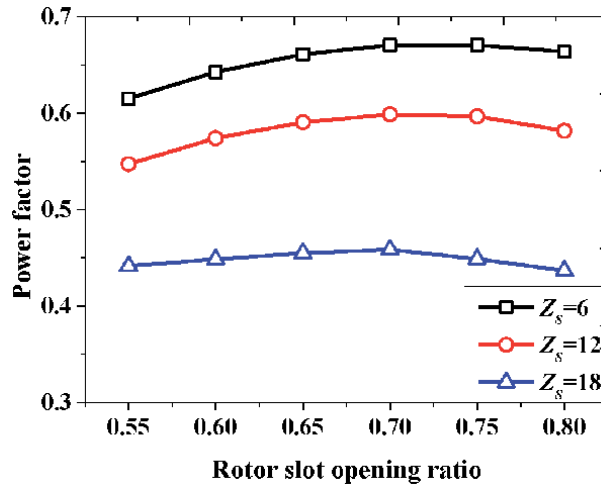


Figure 20.
Effect of rotor slot opening ratio on power factor.

power factor reaches the maximal value. This is because the power factor is mainly influenced by the back-EMF. When the rotor slot opening ratio increases, the effective airgap length becomes smaller, thus the main flux is increased and the back-EMF is improved. As a result, the power factor is increased. When the rotor slot opening ratio keeps increasing, the flux modulation effect of the rotor teeth becomes weaker and weaker, thus the smaller modulated flux, and the lower back-EMF. Therefore, there is also an optimal value for rotor slot opening ratio when a high power factor is demanded.

4.4 PM demagnetization performances

For PM machines, PM demagnetization performances are very important because it is highly related to the safe operation and machine reliability. Therefore, the PM demagnetization performances of FRPMMs should be analyzed in this

chapter. Since the magnetic properties of PM materials are sensitive to temperature, and the temperature coefficient of NdFeB magnet is as high as $-0.126\%K^{-1}$. When the current of FRPMMs is large, the winding heating can easily affect the PMs attached to the stator teeth surface, causing the decrease of PM magnetic performances. On the other hand, when the winding current is large, the demagnetizing effect of the armature field is enhanced, and thus the PMs have the possibility to be demagnetized. Therefore, it is of great importance to investigate the PM demagnetization performances of FRPMMs at different conditions.

Figure 21 shows the demagnetization curve of the magnets. The upper half is a straight line, and lower half under the knee point B_{knee} is a curved line. When the FRPMM works on the straight line (such as point P_1), the return line coincides with the demagnetization curve, and the magnetic performance of the magnets will not be lost. However, when the armature equivalent MMF H_a' is too large at load condition, or the knee point is too high, the working point B_{knee} is moved to P_2 . At this time, the recovery line does not coincide with the original demagnetization line, thus the intersection of the B -axis changes from B_r to B_{r1} , causing the irreversible demagnetization. Then, the PM properties and machine performances will no longer return to the original. So, the PM flux density should be examined in order to check the risk of irreversible demagnetization. As we know, the PM flux density is determined by the design parameters such as electric loading A_e , PM thickness h_m , rotor slot opening ratio, etc. So, in this chapter, the effects of electric loading A_e , PM thickness h_m , rotor slot opening ratio b_o/t on PM demagnetization performances of FRPMMs will be studied. For instance, the PM material is selected as N38SH, and knee point of the PM flux density at $100^\circ C$ is 0.35 T.

Figure 22 shows the PM flux density of a 12-stator-slot/14-rotor-slot FRPMM when the electric loading A_e is 1600A/cm, the PM thickness h_m is 3 mm, rotor slot opening ratio b_o/t is 0.65. It can be seen that the PM flux density distribution varies with the rotor position. When the rotor position is 140° , the PM does not demagnetize, while at 0° and 340° , the PM will demagnetize. Hence, in the following analysis, the PM flux density at the most severe moment of demagnetization is selected.

Figure 23 studies the magnetic flux density distribution in the PMs under different electric loadings. It can be found that the larger electric loading A_e , the smaller minimum flux density. This is because the larger electric loading, the higher armature MMF H_a' , and the more left operating point P_2 , so the lower flux density

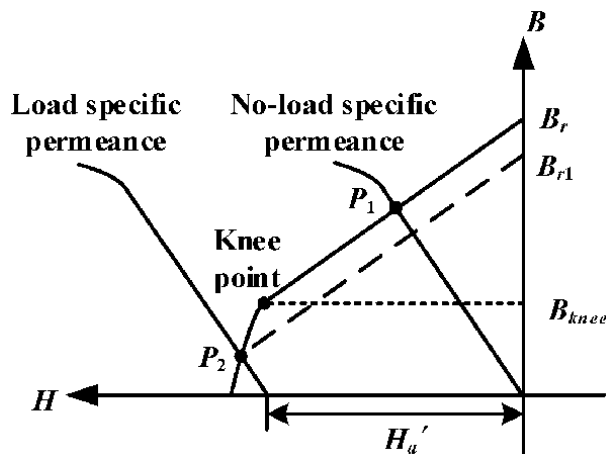


Figure 21.
 PM demagnetization curve.

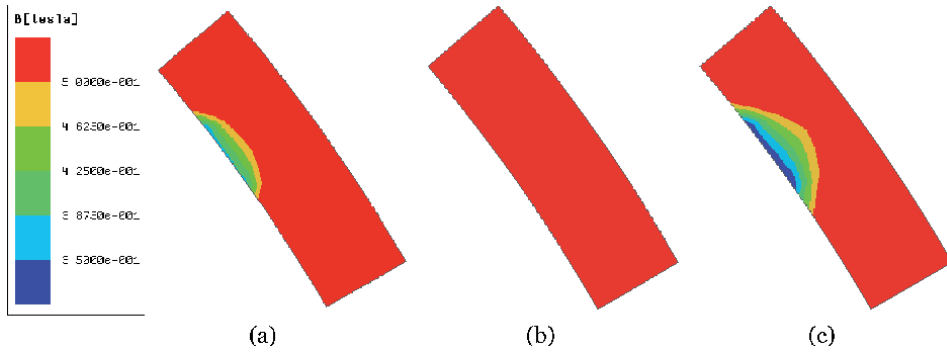


Figure 22. PM demagnetization at different rotor positions: (a) rotor position = 0° ; (b) rotor position = 140° ; (c) rotor position = 340° .

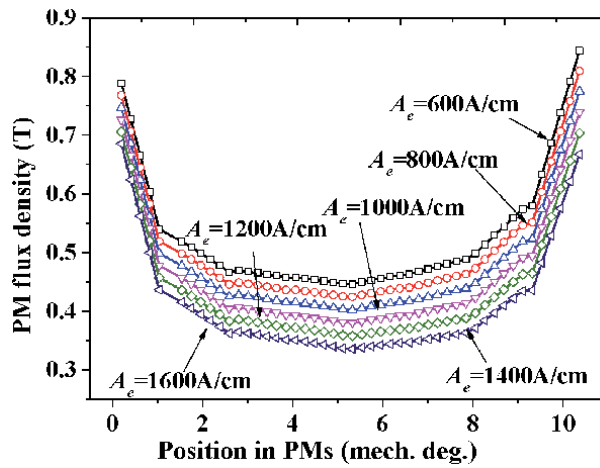


Figure 23. Influence of A_e on PM demagnetization.

in the magnets. When the electric loading A_e is 1400 A/cm , the PM irreversible demagnetization just occurs. In addition, it can be seen that the entire magnetic flux density map is skewed to the right. This is because the N-pole magnet is intercepted in this analysis, and there is an S-pole magnet next to the N-pole magnet. There is PM pole leakage flux between the S-pole magnet (negative axis) and the N-pole magnet (positive axis), so the magnetic flux density around the 0 position is lower, and away from the 0 position, the magnetic flux density gradually rises.

Figure 24 analyzes the effect of PM thickness h_m on the PM demagnetization performances. At this time, the electric loading is chosen as 800 A/cm , and the rotor slot opening ratio is selected as 0.65. It can be seen in **Figure 24** that when the PM thickness h_m is less than 2.5 mm, the irreversible demagnetization will happen, while when the PM thickness h_m is larger than 2.5 mm, the irreversible demagnetization will not. In this model, the airgap length is 0.5 mm. Therefore, in the design stage, the PM thickness should be better to set as five times or more the airgap length. Considering the back-EMF, it is claimed in [3] that when the PM thickness is about three times the airgap length, the back-EMF will reach the maximum. But considering both back-EMF and PM demagnetization risk, it is safer to set the PM thickness as about five times airgap length.

Figure 25 shows the influences of rotor slot opening ratio b_o/t on the flux density distribution inside the PMs. At this time, the electric loading is chosen as 800 A/cm ,

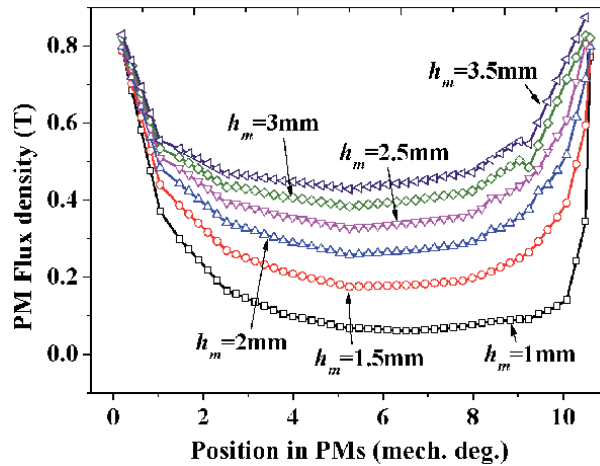


Figure 24.
 Influence of h_m on PM demagnetization.

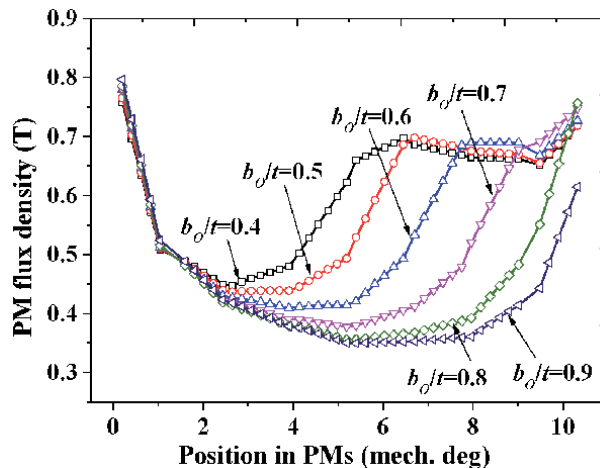


Figure 25.
 Influence of b_o/t on PM demagnetization.

and the PM thickness is selected as five times the airgap length, that is, 3 mm. The larger rotor slot opening ratio, the narrower rotor teeth, thus the more saturated rotor teeth, and the smaller magnetic reluctance. As shown in **Figure 20**, when the magnetic gets smaller, the more left operating point P_2 , and thus the lower PM flux density. It can be seen in **Figure 25** that when the rotor slot opening ratio b_o/t is 0.9, the irreversible PM demagnetization just occurs. In Ref. [28], it is claimed that the maximum back-EMF can be achieved when the rotor slot opening ratio b_o/t is around 0.6. So, during the design process, the optimal rotor slot opening ratio can be directly applied without consideration of the PM demagnetization risk.

5. Geometric design of stator and rotor

5.1 Stator design

The geometrical parameters of stator and rotor are shown in **Figure 26**. The no-load flux of each winding pole could be calculated as:

